Development of numerical models within the liquid film and Lagrangian spray framework

Baleta, Jakov

Doctoral thesis / Disertacija

2016

Degree Grantor / Ustanova koja je dodijelila akademski / stručni stupanj: **University of Zagreb, Faculty of Mechanical Engineering and Naval Architecture / Sveučilište u Zagrebu, Fakultet strojarstva i brodogradnje**

Permanent link / Trajna poveznica: https://urn.nsk.hr/urn:nbn:hr:235:326725

Rights / Prava: In copyright / Zaštićeno autorskim pravom.

Download date / Datum preuzimanja: **2024-03-29**

Repository / Repozitorij:

Repository of Faculty of Mechanical Engineering and Naval Architecture University of Zagreb







University of Zagreb

Faculty of Mechanical Engineering and Naval Architecture

Jakov Baleta

DEVELOPMENT OF NUMERICAL MODELS WITHIN THE LIQUID FILM AND LAGRANGIAN SPRAY FRAMEWORK

DOCTORAL THESIS

Zagreb, 2016



Sveučilište u Zagrebu

Fakultet strojarstva i brodogradnje

Jakov Baleta

RAZVOJ NUMERIČKIH MODELA U PODRUČJU FILMA KAPLJEVINE NA STJENCI I LAGRANGEOVOG SPREJA

DOKTORSKI RAD

Zagreb, 2016.



University of Zagreb

Faculty of Mechanical Engineering and Naval Architecture

Jakov Baleta

DEVELOPMENT OF NUMERICAL MODELS WITHIN THE LIQUID FILM AND LAGRANGIAN SPRAY FRAMEWORK

DOCTORAL THESIS

Supervisor:
prof. dr. sc. Neven Duić

Zagreb, 2016



Sveučilište u Zagrebu

Fakultet strojarstva i brodogradnje

Jakov Baleta

RAZVOJ NUMERIČKIH MODELA U PODRUČJU FILMA KAPLJEVINE NA STJENCI I LAGRANGEOVOG SPREJA

DOKTORSKI RAD

Mentor:
prof. dr. sc. Neven Duić

Zagreb, 2016.

BIBLIOGRAPHY DATA

UDC: 532.51

Keywords: analytical force balance; catalyst; computational fluid dynamics; Eulerian approach; film roughness; film rupturing; gas aftertreatment; Lagrangian spray; multicomponent evaporation; NOx reduction; reaction kinetics; selective catalytic reduction; selective non-catalytic reduction; turbulent boundary layer; UNIFAC method; urea deposits; urea thermal decomposition; urea water solution; wall function; wall film

Scientific area: TECHNICAL SCIENCES

Scientific field: Mechanical engineering

Institution: Faculty of Mechanical Engineering and Naval Architecture

Thesis supervisor: Prof.dr.sc. Neven Duić

Number of pages: 77

Number of figures: 32

Number of tables: 4

Number of references: 91

Date of examination:

Thesis defence commission:

Doc.dr.sc. Milan Vujanović – Chairman of defence commission

Prof.dr.sc. Ladislav Lazić – member

Dr.sc. Klaus Pachler – member

Archive: Faculty of Mechanical Engineering and Naval Architecture

ACKNOWLEDGMENTS

I hereby declare that this thesis is entirely the result of my own work and knowledge obtained during my studies, except where otherwise indicated. I have fully cited all used sources and I have only used the ones given in the list of references.

I would like to begin by expressing my gratitude to my supervisor, Professor Neven Duić for giving me this great opportunity to participate in international collaboration with AVL List GmbH. Financial support for this work is gratefully acknowledged from AVL Croatia and its manager mr. sc. Goran Mirković. I am also grateful to Dr. Klaus Pachler for valuable advices, discussions and guidance throughout this work. Special thanks goes to Dr. Milan Vujanović for his advices, guidance, patience and constant support. His inexhaustible positive energy and bright personality kept me motivated during the hardest periods of making this work when the shadow of self-doubt was over me. I would also extend my appreciation to guys from PowerLab for their technical support and valuable discussions. Thank you Zvonimir for showing be programming hacks and tips. Technical support from Dr. Marko Ban was of crucial importance, especially during first months of work, when I was starting my work on PhD. Valuable discussions and ideas that came from Dr. Mikulčić have contributed to the final quality of the work. Finally and most important, I am truly thankful to my family for their unconditional love, understanding, patience, support and for keeping me focused on the thesis. I dedicate this work to my recently deceased grandmother, who was really looking forward to see the end of this thesis. Unfortunately, things went differently.

Jakov Baleta, June 1st, 2016

"Felix, qui potuit rerum cognoscere causas."

Publius Vergilius Maro

CONTENT

BIBLIOGRAPHY DATA I
ACKNOWLEDGMENTS II
CONTENT IV
LIST OF FIGURES VI
LIST OF TABLES VII
NOMENCLATURE VIII
ABSTRACT XV
SAŽETAK XVI
PROŠIRENI SAŽETAK XVII
KEY WORDS XXIV
KLJUČNE RIJEČI XXV
1. INTRODUCTION 1
2. FUNDAMENTAL EQUATIONS OF FLUID FLOW 9
2.1. Conservation equations 10
2.2. General transport equation 11
2.3. Turbulent flows 12
2.3.1. Averaging of conservation equations 12
2.3.2. Turbulence modelling 13
2.4. Numerical procedure 17
2.4.1. Integral form of the transport equation 17
2.4.2. Time discretization 17
2.4.3. Control volume discretisation 18
2.4.4. Numerical schemes 18
2.4.5. Solution procedure 19
3. SELECTIVE NON-CATALYTIC REDUCTION 21
3.1. Description of spray droplets motion inside the domain 21
3.2. Evaporation of urea-water droplets 22
3.3. Chemical reactions taking place in the gas phase 25
4. LIQUID WALL FILM MODELLING 26
4.1. Governing equations 26
4.2. Phase interaction 28
4.3. Submodels 30
4.3.1. Film rupturing 30
4.3.2. Evaporation 31
4.3.2.1. Single component evaporation 32
4.3.2.2. Multicomponent evaporation 34
4.3.3. Urea thermal decomposition 36
4.3.4. Spray/wall interaction 38

5. NUMERICAL SIMULATIONS, RESULTS AND DISCUSSION 40
5.1. Film rupturing 40
5.1.1. Experimental configuration 40
5.1.2. Numerical simulation 41
5.1.3. Results 42
5.2. Multicomponent evaporation 44
5.2.1. Experimental configuration 44
5.2.2. Numerical simulation 44
5.2.3. Results 45
5.3. Urea thermal decomposition 48
5.3.1. Experimental configuration 48
5.3.2. Numerical simulation 48
5.3.3. Results 50
5.4. SNCR cases 53
5.4.1. Pipe reactor 53
5.4.1.1. Experimental configuration 53
5.4.1.2. Numerical simulation 54
5.4.1.3. Results 55
5.4.2. Industrial incinerator 60
5.4.2.1. Experimental configuration 60
5.4.2.2. Numerical simulation 61
5.4.2.3. Results 63
6. CONCLUSION 67
7. LITERATURE 70
8. CURICULUM VITAE 76

LIST OF FIGURES

Figure 1. Turbulent fluctuation of general physical quantity [41] 13
Figure 2. Schematic representation of computational node 18
Figure 3. Force balance on film ligament [12] 30
Figure 4. Reaction scheme of urea [82] 36
Figure 5. Schematic representation of droplet wall interaction and interaction regimes [84] 39
Figure 6. Computational domain with boundary conditions for case of film rupturing 41
Figure 7. Qualitative representation of film separation criterion 42
Figure 8. Film rupturing at the sharp corner 43
Figure 9. Shematic representation of test section [35] 44
Figure 10. Mesh representation of computational domain 45
Figure 11. Comparison of gas phase concentrations in measurement plane 4 (O'Rourke model) 46
Figure 12. Comparison of gas phase concentrations in measurement plane 4 (Wittig model) 47
Figure 13. Comparison of gas phase concentrations in measurement plane 4 – lower pressure 47
Figure 14. Computational domain with plate detail 49
Figure 15. Biuret decomposition – comparison with experimental results 50
Figure 16. Spray/wall interaction and temperature field on the experimental plate 51
Figure 17. Development of urea deposits on the Birkhold experimental case 52
Figure 18. Schematic representation of experimental pipe reactor [29] 53
Figure 19. Computational domain with symmetric boundary condition 54
Figure 20. Detail of spray injection 56
Figure 21. Velocity field 56
Figure 22. Temperature field 57
Figure 23. Water vapour mass fraction 58
Figure 24. Ammonia mass fraction distribution 58
Figure 25. Isocyanic acid mass fraction distribution 59
Figure 26. NO mass fraction distribution 59
Figure 27. Comparison of experimental and numerical results 60
Figure 28. Computational domain of the incinerator 62
Figure 29. Urea-water solution spray at the the developed state 63
Figure 30. Flow temperature, NO reduction rate and NO mass concentration for two time points 64
Figure 31. Flow velocity, H_2O and NH_3 mass fraction for two time points 65
Figure 32. The NO mass fraction reduction from the inlet to the point of experimental measurement 66

LIST OF TABLES

Table 1. The values of the constants in the k-ε model 15
Table 2. The values of the constants in the k-ζ-f turbulence model 16
Table 3. Seven step reaction mechanism 25
Table 4. Kinetic reaction scheme of urea decomposition [22] 37

NOMENCLATURE

Latin	Unit	Description
Kn	-	Knudsen number
$\bar{l}$	m	Average free path length of the molecule
L	m	Characteristic linear dimension of observed domain
f_i	m/s^2	Body force
$\bar{k}$	m^2/s^2	Turbulent kinetic energy
a_P	-	Control volume discretisation central matrix coefficient
x_{id}	m	Droplet position vector
$\bar{k}_g$	W/(m K)	Thermal conductivity of the gas mixture
B_T	-	Heat transfer number
$\hat{n}_i$	-	Unit normal to the face cell facing outwards
$\dot{H}_{sor,wf}$	W	Heat flux from wall side
$\dot{H}_{sor,fg}$	W	Heat flux from the gas phase boundary layer above the film
$\dot{m}_{ev}$	kg/s	Liquid film evaporation rate
h_{ev}	J/kg	Enthalpy of evaporation
$\dot{H}_{sor,im}$	W	Energy flux from impacting spray droplets
$\dot{H}_{sor,ent}$	W	Energy flux leaving the film due to film entrainment
Re_{ks}	-	Reynolds number for roughness
$\dot{V}_f$	m^3/s	Film volumetric flow
$\dot{m}$	kg/s	Evaporated mass flux
c_I	-	Vapour concentration at the film/gas interface
D_{12}	m^2/s	Binary diffusion coefficient
D_t	m^2/s	Turbulent diffusion coefficient
St_m	-	Stanton number for mass transfer
$u_{//}$	m/s	Film parallel velocity
H_Y	-	Wall function for evaporation
M^*	-	Dimensionless vaporization rate
$T_{g\infty}$	K	Gas phase temperature
c_{pg}	J/(kg K)	Gas phase heat capacity
T_s	K	Film surface temperature
T^*	-	Dimensionless temperature
K	-	Dimensionless droplet velocity
$\bar{c}_{pF}$	J/(kg K)	The specific heat capacity of the vapour

$\bar{c}_{pG}$	J/(kg K)	The specific heat capacity of gas mixture
$\dot{m}_{vap}$	kg/s	Vaporization rate
A	s^{-1}	Frequency rate in Arrhenius expression
A	m^2	Surface area of film patch
A_R	m^2	Surface area of HNCO in evaporation model
B	-	Spalding number
B_Y	-	Mass transfer number
C	m^{-1}	Surface curvature
C	-	Constant in wall film shear expression
c	-	Concentration of the liquid film
c_f	-	Local friction factor
C_μ ,$C_{\varepsilon 1}$, $C_{\varepsilon 2}$, C_1,C_2', C_L, C_η, C_τ	-	Model constant of *k*-ζ-*f* model of turbulence
C_μ, C_1, C_2	-	Model constant of *k*-ε model of turbulence
D_d	m	Droplet diameter
E_a	kJ/mol	Activation energy
f	kg/(m^3 s)	Elliptic function
F_{ib}	N	Contribution from other external forces
F_{idr}	N	Drag force
F_{ig}	N	Force including the effects of gravity and buoyancy
F_{ip}	N	Pressure force
F_M, F_T	-	Diffusional film correction factors
G	kg /(m s^3)	Generation of turbulent kinetic energy
g_i	m/s^2	Gravity vector
h	J/kg	Film specific enthalpy
h	-	Ratio of liquid and vapour HNCO density
h_f	m	Film thickness
i	J/kg	Specific internal energy of fluid
j	mol/s	Source term for the evaporation rate
K	m^2/s^2	Turbulent kinetic energy
K	-	Dimensionless droplet velocity
k_s		Correction function
L	m	Length of the face cell boundary/turbulent length scale
L	J/kg	Latent heat of evaporation
Le	-	Lewis number
L_b	m	Ligament length
l_t	m	Characteristic turbulent length
m_d	kg	Droplet mass
M	kg/mol	Molar mass
M_i	kg (m/s)	Film momentum
Nu^*	-	Modified Nusselt number

Nu_0	-	Nusselt number of the non-evaporating droplet
Δn	m	normal distance from the wall
$\frac{dp}{dx}$	Pa/m	streamwise pressure gradient
p	Pa	Thermodynamic pressure
p_{drop}	Pa	Pressure resulting from spray droplets impingement
$p_{f,vel}$	Pa	Dynamic film pressure
p_{fluid}	Pa	The pressure from liquid film in neighbouring cells
p_{hyd}	Pa	Hydrostatic pressure
p_i(y)	Pa	Partial pressure of *i*–th liquid component in the gas phase
$p_{i,s}$	Pa	Partial pressure of the *i*–th liquid component on the film/gas interface
P_m	-	Correction factor
Pr	-	Prandtl number
p_{refer}	Pa	Static gas pressure (reference pressure),
p_σ	Pa	Capillary pressure
$\dot{Q}$	W	Heat flux
q_i	W/m^2	Heat flux density vector
r	s^{-1}	Reaction rate
R	J/(mol K)	Universal gas constant
Re	-	Reynolds number
S	s^{-1}	additional term for definition of turbulent length and time scales
Sc	-	Schmidt number
Sh^*	-	Modified Sherwood number
Sh_0	-	Sherwood number of the non-evaporating droplet
S_i	W/m^3	Heat source/sink
S_m	N/ m^3	Source/sink term of momentum equation
S_M	N	Source and sink terms of film momentum equation
S_{mD}	kg/s	Film mass source
S_{mV}	kg/s	Film mass sink term
$S_{\gamma i,D}$	kg/s	Source of *i*-th liquid film component in species conservation equation for wall film
$S_{\gamma i,V}$	kg/s	Sink of *i*-th liquid film component in species conservation equation for wall film
St_m	-	Stanton number for mass transfer
t	s	Time
Δt	s	Time interval
T	K	Thermodynamic temperature
$\overline{T}$	K	Reference temperature
T_S	K	Droplet saturation temperature

u^+	-	Nondimensional velocity
u_1, u_2	m/s	Film velocity components
$u_{d,\perp}$	m/s	Wall normal component of the droplet velocity
u_f	m/s	Mean film velocity
U_g	m/s	Gas phase velocity
u_{id}	m/s	Droplet velocity
u_j	m/s	Velocity vector components
$\overline{v}$	m/s	Average molecular velocity
V	m^3	Volume
V_j	m/s	Wall velocity
v_t	m/s	Characteristic velocity of turbulent fluctuations
We_{rel}	-	Weber number
w_f	m	Film width
x_j	m	Cartesian coordinates
y	m	Wall normal distance
y^+	-	Dimensionless normal coordinate
y_C^+	-	Threshold value of y^+
Y_i	-	Vapour mass fraction of i-th liquid component
Y_V	-	Vapour mass fraction
Y_u	-	Urea concentration in droplet
$\overline{Y}$	-	Reference vapour concentration

Greek	**Unit**	**Description**
β_{stefan}	-	Stefan flux correction
ρ	kg/m^3	Fluid density
σ_{ij}	N/m^2	Stress tensor
δ_{ij}	-	Kronecker delta
τ_{ij}	N/m^2	Viscous stresses
μ	Pa s	Fluid viscosity
λ	W/(m K)	Thermal conductivity
ϕ	-	Exponent of heat transfer number
φ	-	General transport scalar variable
$\overline{\varphi}$	-	Averaged general transport scalar variable
μ_t	Pa s	Turbulent viscosity
$\overline{\varepsilon}$	m^2/s^3	Turbulent energy dissipation rate
ν	m/s^2	Kinematic viscosity
σ^k	-	Model constant of *k-ε* and *k-ζ-f* model of turbulence
σ^ε	-	Model constant of *k-ε and k-ζ-f* model of turbulence

ζ	-	Velocity scales ratio
τ	s	Turbulent time
σ^{ζ}	-	Model constant of *k*-ζ-*f* model of turbulence
L	m	Turbulent length scale
$\overline{\rho}_g$	kg/m^3	Density of the gas mixture
$\overline{\beta}_g$	m^2/s	Binary diffusion coefficient of the gas mixture
δ	m	Film thickness
δ_T	m	Fictional gas film thickness for modelling heat transfer resistance
δ_m	m	Fictional gas film thickness for modelling mass transfer resistance
Γ_i	N	Term that takes into account all shear stresses
σ	N/m	Surface tension
γ_i	-	Concentration of *i*-th liquid component in the film
κ	-	Von Kármán constant
τ_w	N/m^2	Wallfilm shear
θ	°	Inclination of the surface from the horizontal
ρ_g	kg/m^3	Gas phase density
ρ_{vap}	kg/m^3	Vapour density
μ_f	Pas	Liquid film dynamic viscosity
μ_L	Pa s	Laminar viscosity
$\dot{Q}$	W	Heat flux from/to gas phase
ρ_{gs}	kg/m^3	Gas phase density
$\beta_{stefan,i}$	-	Stefan flux correction
μ_{d}	Pa s	Dynamic viscosity of the droplet

Subscripts	**Description**
∞	Related to undisturbed ambient conditions
d	Droplet
e	Numerical schemes, control volume discretisation
E	Numerical schemes, control volume discretisation
f	Film
g	Gas
i	Cartesian component index
j	Cartesian component index
k	Cartesian component index
L	Laminar
l	Liquid
m	Matrix

n	Related to the new time level
o	Related to the old time level
P	Numerical schemes, control volume discretisation
S	Condition at droplet surface
s	Solid
t	Turbulent
v	Vapour
W	Numerical schemes, control volume discretisation
w	Numerical schemes, control volume discretisation
w	Wall
φ	General variable

Superscripts	**Description**
φ	related to general transport variable
’	fluctuating component
n	Related to the new time level
o	Related to the old time level

Abbreviations	**Description**
CDS	Central Differencing Scheme
CFD	Computational Fluid Dynamics
CPU	Central Processing Unit
CV	Control volume
DDM	Discrete Droplet Method
deNOx	Nitrogen oxides removal
DTG	Differential Thermal Gravimetric
FTIR	Fourier transform infrared spectroscopy
HPLC	High Performance Liquid Chromatography
IC engines	Internal Combustion engines
NSR	Normalised Stoichiometric Ratio
PISO	Pressure Implicit with Splitting of Operator
RANS	Reynolds-Averaged Navier-Stokes
RDF	Računalna dinamika fluida
SCR	Selective Catalytic Reduction
SIMPLE	Semi-Implicit Method for Pressure-Linked Equations
SNCR	Selective Non-Catalytic Reduction
TGA	Thermogravimetric analysis
UDS	Upwind Differencing Scheme
UNIFAC	UNIQUAC Functional-group Activity Coefficients
UWS	Urea-Water Solution

Chemical species	**Name**
$(NH_2)_2CO$	Urea
$(NH_2)_2CONHCO$	Biuret
CO	Carbon monoxide
CO_2	Carbon dioxide
cya	Cyanuric acid
H	Hydrogen ion
H_2O	Water
HNCO	Isocyanic acid
N_2	Nitrogen
N_2O	Nitrous oxide
NCO	Cyanate
NH_3	Ammonia
NO	Nitric oxide
NOx	Nitrogen oxides
O	Oxygen ion
O_2	DioOxygen
OH	Hydroxide

ABSTRACT

Liquid film flow sheared by an external air flow field is a physical phenomenon encountered in many engineering applications such as: burners, rain on vehicle windows and aircraft wings, rocket nozzles, mist eliminators, heat exchangers, steam turbine blades and especially internal combustion (IC) engines. Specifically, liquid wall films affect chemical composition of the gas phase and wall thermal behaviour of these systems. The goal of this research is additional improvement of the Eulerian liquid wall film model through further development and implementation of numerical models with the ultimate aim of achieving more accurate and computationally efficient calculations. The research hypothesis is that improved, adopted and newly developed numerical models are going to enable numerical simulations of multicomponent liquid wall films, and that they could be then used in industrial applications. The first objective was adaptation and implementation of semi-empirical wall film rupturing model to the numerical computational fluid dynamics (CFD) framework, as well as the seven step reaction mechanism for SNCR process modelling. Furthermore, two multicomponent liquid film evaporation models were developed, the first one on the basis of analogy between momentum and mass transfer, and the second one employing modified wall functions which take into account influence of the evaporation on boundary layer above liquid film. Particular scientific contribution is in implementation of the UNIFAC method for activity coefficients calculation, which is employed for the first time in the area of liquid wall films. Finally, the suitable kinetical model of urea thermal decomposition was adjusted and incorporated into existing numerical framework as a step in the process of description of urea deposits influence on overall domain of the real flue gas aftertreatment system. Developed mathematical models were implemented by employing FORTRAN-based user functions that are connected to the main solver of the commercial CFD code Fire. Coupling between the liquid wall film and the gas phase is achieved through the source terms in the mass, energy, species and momentum conservation equations. The ultimate goal was to obtain results of all relevant chemical and physical phenomena that are satisfactory on both qualitative and quantitative basis. The accuracy of numerical modelling, where possible, was determined by comparison with available and relevant experimental data. Results show satisfactory agreement with experiments and encourage future applications of implemented models in industrial CFD applications.

SAŽETAK

Strujanje filmova kapljevine na stjenci uzrokovano smičnim naprezanjem, kojega vrši vanjska struja zraka, je fizikalni fenomen koji se susreće u velikom broju inženjerskih aplikacija poput: gorionika, kiše na prozorima vozila i krilima zrakoplova, raketnih mlaznica, eliminatora kapljica, prijenosnika topline, lopatica plinskih turbina i, pogotovo motora s unutarnjim izgaranjem. Naime, filmovi kapljevine utječu na kemijski sastav plinske faze i termičko ponašanje stijenki tih sustava. Cilj ovog istraživanja je daljnje poboljšanje Eulerovog modela filma kapljevine na stjenci kroz razvoj i implementaciju numeričkih modela s konačnom svrhom postizanja točnijih i računalno efikasnijih kalkulacija. Hipoteza istraživanja je da će poboljšani, prilagođeni i novo razvijeni numerički modeli omogućiti numeričke simulacije višekomponentnih filmova na stjenci te da se isti mogu koristiti u industrijskim primjenama. Prva zadaća je bila prilagodba i implementacija poluempirijskog modela otkidanja filma u numeričko okruženje računalne dinamike fluida (RDF), kao i sedmostepenog reakcijskog mehanizma za modeliranje procesa selektivne nekatalitičke redukcije. Nadalje, razvijena su dva modela višekomponentnog isparavanja filmova kapljevine na bazi analogije između prijenosa mase i količine gibanja te modificiranih zidnih funkcija koje uzimaju u obzir utjecaj isparavanja filma na granični sloj iznad filma. Specifičan znanstveni doprinos predstavlja implementacija UNIFAC metode za izračun aktivacijskih koeficijenata, koja je po prvi puta primijenjena u području filmova kapljevine na stjenci. Konačno, pogodni kinetički model termalne dekompozicije uree je prilagođen i implementiran u postojeći numerički okvir, kao korak u procesu opisivanja utjecaja depozita uree na domenu čitavog sustava obrade ispušnih plinova. Razvijeni matematički modeli su implementirani upotrebom korisničkih funkcija u programskom jeziku FORTRAN koje su povezane s glavnim rješavačem komercijalnog računalnog RDF paketa Fire. Povezivanje između filma kapljevine i plinovite faze ostvaruje se kroz izvorske članove u jednadžbama održanja mase, energije, kemijskih vrsta i količine gibanja. Konačni cilj bio je dobiti rezultate svih relevantnih kemijskih i fizikalnih fenomena koji će biti zadovoljavajući, kako na kvalitativnoj, tako i kvantitativnoj bazi. Točnost numeričkog modeliranja utvrđena je usporedbom s dostupnim i relevantnim eksperimentalnim podacima gdje god je to bilo moguće. Rezultati pokazuju zadovoljavajuće slaganje s eksperimentima i potiču buduću primjenu implementiranih modela u industrijskim primjenama.

PROŠIRENI SAŽETAK

Različiti propisi za zaštitu okoliša nameću sve veća ograničenja u pogledu emisija ispušnih plinova u industriji i transportu kao dio rješenja problema zagađenja zraka, globalnog zatopljenja te njima uzrokovanih klimatskih promjena. Na emisije nastale uslijed izgaranja fosilnih goriva utječe kvaliteta procesa miješanja goriva i zraka za izgaranje te efikasnost sustava za obradu dimnih plinova. Iz navedenog se jasno vidi da se industrija i transport suočavaju s velikim izazovima kojima se može odoljeti isključivo razvojem novih i efikasnijih sustava korištenjem naprednih alata za razvoj proizvoda, jedan od kojih jest i računalna dinamika fluida (RDF).

Detaljno razumijevanje složenih fizikalnih i kemijskih procesa koji se odvijaju u inženjerskim sustavima iz područja industrije i transporta ključno je za njihovo unapređenje kroz konstrukcijski razvoj i optimizaciju. Sveobuhvatno razumijevanje tih procesa i dalje je veliki izazov za istraživače i znanstvenike uslijed njihove kompleksnosti, ali i otežene mogućnosti eksperimentalnog ispitivanja. Naime, intenzivna eksperimentalna ispitivanja u ovakvim sustavima rezultiraju visokim troškovima i dugotrajnim istraživanjima.

U zadnja dva desetljeća, eksponencijalnim porastom računalne snage, nameće se kao alternativa skupim eksperimentalnim ispitivanjima matematičko modeliranje opisanih procesa uz pomoć RDF-a. Pristup se sastoji u tome da se adekvatnim matematičkim modelom opisuje promatrani fizikalni fenomen, nakon čega se pristupa diskretizaciji interesne domene metodom kontrolnih volumena. Konačno, u posljednjem koraku se jednadžbe modela rješavaju pogodnim numeričkim metodama, nakon čega se dobiveni rezultati prikazuju u grafičkoj formi koja omogućuje njihovu validaciju. Ipak, unatoč navedenim prednostima, u modelima računalne dinamike fluida postoje mnogobrojni izvori pogrešaka, koji unatoč velikim naporima uloženima od strane istraživača i inženjera, još uvijek ne dopuštaju točna kvantitativna predviđanja promatranih fenomena. Računalna dinamika fluida omogućuje skraćivanje vremena i smanjenje troškova razvoja u ranoj, prototipnoj fazi konstruiranja proizvoda. Njome se uz relativno niske troškove već na početku može izvršiti velik broj simulacija kojima se dolazi do kvalitativnog uvida u fiziku promatranog problema, čime se omogućuje odabir svega nekoliko pogodnih prototipova. Oni se zatim izrađuju i detaljno eksperimentalno ispituju kako bi se donio zaključak o optimalnoj konstrukciji proizvoda. Na taj način primjena RDF-a u ranoj fazi razvoja proizvoda značajno skraćuje proizvodni

postupak i pridonosi smanjenju troškova razvoja. Međutim, eksperimentalno ispitivanje, ma koliko skupo, još uvijek je neizbježno sredstvo finalizacije razvoja.

Ovo istraživanje se dotiče četiri različita područja koja se sva mogu pronaći u raznim industrijskim aplikacijama (npr. sustavi obrade dimnih plinova, motori s unutarnjim izgaranjem, kemijski reaktori, itd.): otkidanje filma kapljevine i njegovo isparavanje u slučaju višekomponentnih smjesa, kemijska kinetika ureinih depozita i deNOx kemijska kinetika u slučaju selektivne nekatelitičke redukcije.

Općenito se pristup višekomponentnom isparavanju može podijeliti na dvije različite porodice modela: diskretni višekomponentni modeli i kontinuirani višekomponentni modeli. Diskretni višekomponentni modeli prate individualne komponente goriva i omogućuju direktno povezivanje s reakcijskom kinetikom pojedinih komponenti goriva, dok se kontinuirani višekomponentni modeli temelje na kontinuiranoj termodinamičkoj metodi i opisuju sastav goriva kao kontinuirano distribuiranu funkciju s obzirom na neki parametar, poput molekularne mase. Ovaj pristup smanjuje računalne zahtjeve u usporedbi s prethodnim, ali se pokazuje netočnim u slučaju ako se zahtijevaju detaljni kemijski izračuni, ili kod smjesa sastavljenih od velikog broja komponenata. Kako su trenutni zahtjevi za točnošću računalnih simulacija relativno visoki, ovaj rad će se usredotočiti isključivo na diskretne modele višekomponentnog isparavanja. Unutar njega, temperatura filma i koncentracija kemijskih vrsta se smatraju konstantnima unutar filma. Implementiran je model isparavanja po analogiji izmjene mase i količine gibanja, ali i višekomponentni model koji se temelji na generaliziranim zidnim funkcijama O'Rourkea i Amsdena, a koje su prilagodili Torres i sur. Kao doprinos ovog rada, parcijalni tlak pojedine komponente u filmu na granici između filma i plinske faze izračunat je korištenjem UNIFAC metode koja uzima u obzir međuutjecaj molekularne strukture pojedinih komponenata u smjesi. To omogućuje točniji izračun koncentracija koje imaju presudan utjecaj na brzinu isparavanja. Pregledom dostupne literature ustanovljeno je da je sličan pristup napravljen jedino kod opisivanja kapljica spreja.

Iako je ponašanje tankih filmova kapljevine na čvrstoj stjenci pokriveno brojnim numeričkim, teoretskim i eksperimentalnim istraživanjima, isto ne vrijedi za fiziku filmova kapljevine koji prelaze preko oštroga ruba. S obzirom na uvid dobiven pregledom literature, do sada je objavljeno samo nekoliko istraživanja koja su se bavili konstrukcijom teoretskog modela. Nedavni rad Fiedricha i sur. usredotočio se na nedostatke prethodnih pristupa kako bi ih nadišao. Kriterij odvajanja je izveden iz uvjeta ravnoteže sila na kontrolni volumen koji obuhvaća ligament filma koji se počinje odvajati od ruba. U obzir su uzete površinska napetost, inercija filma i gravitacija. Iako ovaj pristup ima tendenciju preranog predviđanja

otkidanja, smatra se prilično pouzdanim. U sklopu ovoga rada izvršena je prilagodba i implementacija spomenutog modela otkidanja filma unutar postojećeg numeričkog okvira komercijalnog računalnog RDF paketa. Verifikacija modela izvršena je na bazi fizikalnog razmatranja, pošto u literaturi nije pronađen model koji opisuje svojstva otkinutog filma, kao što su razdioba veličine čestica i njihova brzina te funkcija postotka otkinute mase ovisno o uvjetima u strujanju.

Selektivna katalitička redukcija, kao jedna od najperspektivnijih metoda za redukciju dušikovih oksida, nameće nove izazove konstruktorima u području predviđanja ponašanja filma kapljevine na stjenci. Trenutno stanje razvoja numeričkih modela omogućuje pouzdanu simulaciju pripreme spreja, posebice jednolikosti raspodjele reducirajućeg sredstva i polja strujanja prije katalizatora te kemijskih reakcija koje se odvijaju unutar katalizatora za selektivnu katalitičku redukciju (eng. *Selective Catalytic Reduction*- SCR). Međutim, pouzdano predviđanje stvaranja i ponašanja depozita uree uz pomoć numeričkih simulacija još uvijek je tema najnovijih istraživanja. Unatoč činjenici da se eksperimentalno ispitivanje dekompozicije uree odvija već dugi niz godina, samo modeliranje kemijske kinetike ureinih depozita počelo je tek nedavno. Ebrahimian i sur. bili su prvi koji su predstavili reducirani model kinetike ureinih depozita koji je moguće povezati s RDF kodom. Model se sastoji od 12 reakcija koje opisuju termolizu uree te stvaranje i razgradnju cijanurne kiseline i biureta. Sam model je u stanju opisati utjecaj promjenjive brzine zagrijavanja, ali se temelji na poznatoj početnoj masi uzorka, čime je ograničena njegova primjenjivost. Naime, u realnim ispušnim sustavima masa depozita uree varira ovisno o trenutnoj temperaturi, koncentraciji produkata u plinskoj fazi iznad depozita, temperaturi stjenke i ubrizganoj masi spreja te nije unaprijed poznata. Dekompozicija i ponašanje biureta, cijanurne kiseline i amelida nisu dobro predviđeni. Također, model ne uzima u obzir utjecaj geometrije substrata na proces razlaganja depozita. Utvrđene nedostatke ispravili su Brack i sur. razvivši reducirani model temeljen na 15 reakcija koje opisuju termolizu uree te stvaranje i razgradnju biureta i cijanurne kiseline. Sam postupak razgradnje podijelili su u tri područja u kojima različiti depoziti imaju dominantnu ulogu. Shodno tome, pojedinačno su eksperimentalno analizirali razlaganje svakog dominantnog depozita, odredili glavne reakcijske puteve te, nakon optimizacije pojedinih stadija, uklopili sve istražene mehanizme u cjelokupan proces razlaganja uree. Međutim, pretragom dostupne literature nije pronađen nijedan točan model kemijske kinetike implementiran unutar RDF koda. Stoga je jedan od ciljeva rada razvoj, implementacija i prilagodba kinetičkog modela razlaganja uree Brack-a i suradnika na model filma kapljevine

kao korak u procesu objašnjavanja utjecaja depozita uree na cjelokupnu domenu realnog ispušnog sustava.

Posljednji dio ovog rada dotiče se selektivne nekatalitičke redukcije (eng. *Selective Non-Catalytic Reduction* - SNCR) kao efikasne i jeftine metode uklanjanja NOx-a iz dimnih plinova emitiranih iz sektora industrije. Sve stroži emisijski standardi na dopušteni nivo NOx-a u dimnim plinovima iz raznih industrijskih ložišta ne mogu se više ispoštovati korištenjem primarnih mjera za redukciju NOx-a. Potrebno je korištenje neke metode obrade dimnih plinova, jedna od kojih je SNCR, koja je dokazana efektivna i jeftina metoda za kontrolu NOx-a iz velikih stacionarnih postrojenja, poput elektrana, spalionica, kotlova i cementnih kalcinera. Sam proces se odvija ubrizgavanjem reducensa, poput amonijaka ili vodene otopine uree u struju vrućih dimnih plinova. Na SNCR proces najviše utjecaja imaju boravak reducensa u reakcijskoj zoni, temperaturni profil reakcijske zone, kvaliteta miješanja reducensa s dimnim plinovima, koncentracija NOx-a u dimnim plinovima, pobjeg amonijaka u okoliš, te normalizirani stehiometrijski omjer. Duljina boravka reducensa u reakcijskoj zoni je faktor čije povećanje omogućuje dulji kontakt između reducensa i NOx-a. Ona ovisi ponajviše o geometriji strujanja i profilu brzina u reakcijskoj zoni. Većina istraživača se slaže da se optimalna temperatura SNCR procesa nalazi unutar relativno uskog raspona između 800 i 1100 °C. Iznad tog raspona amonijak ima tendenciju vezivanja s kisikom, a ispod je brzina reakcije s NOx-om preniska. Kvaliteta miješanja između reducensa i dimnih plinova ovisi o brzinama i vrtloženju u reakcijskoj zoni te uvjetima ubrizgavanja reducensa, dok se na koncentraciju NOx-a u dimnim plinovima može utjecati putem primarnih mjera za redukciju.
Svi radni uvjeti su međuzavisni i pokazuju da, iako je princip SNCR-a vrlo jednostavan, proces izvedbe optimalnog procesa ili retrofit na postojećem postrojenju su daleko od trivijalnog. RDF nam omogućuje izvođenje tzv. virtualnih eksperimenata kako bismo dobili detaljan uvid u radne karakteristike procesa što je inače vrlo teško ostvariti mjerenjem zbog otežane dostupnosti mjerenja te velikog prostora i turbulencija koje izazivaju snažnu varijaciju parametara i mogu prikriti esencijalne karakteristike. Uključivanjem sedmostepenog reduciranog kemijskog deNOx mehanizma razvijenog od strane Brouwera u računalno okruženje RDF-a u ovome radu omogućena je simulacija svih relevantnih fizikalno-kemijskih procesa koji dolaze do izražaja tijekom selektivne nekatalitičke redukcije, a što je potvrđeno izvođenjem simulacija na geometriji eksperimentalnog cijevnog reaktora i realnog spaljivača komunalnog otpada.

Cilj i hipoteza

Cilj ove teze je poboljšanje Eulerovog modela filma kapljevine na stjenci daljnjim razvojem i implementacijom numeričkih modela, s krajnjim ciljem točnijih i efikasnijih izračuna kompleksnih fizikalnih i kemijskih fenomena koji se javljaju u čitavom nizu inženjerskih sustava za izgaranje u području industrije i transporta. Specifični istraživački ciljevi su prilagodba i implementacija modela otkidanja filma kapljevine razvijenog od strane Friedricha i sur., razvoj modela višekomponentnog isparavanja te modeliranje kemijske kinetike ureinih depozita i selektivne nekatalitičke redukcije.

Hipoteza istraživanja je da će poboljšani, prilagođeni i novo razvijeni numerički modeli omogućiti numeričke simulacije višekomponentnih filmova na stjenci te da se isti mogu koristiti u industrijskim primjenama.

Metode i pregled disertacije

Ovaj rad numerički opisuje fenomene filma kapljevine na stjenci koji se događaju unutar čitavog niza industrijskih aplikacija kroz daljnju matematičku nadogradnju postojećeg numeričkog okvira temeljenog na zakonima održanja fizikalnih veličina. Unutar komercijalnog programskog paketa za računalnu dinamiku fluida AVL Fire, baziranom na metodi kontrolnih volumena, koji će biti korišten za istraživanje, kapljice spreja opisuju se korištenjem Lagrangeove formulacije, dok se plinovita faza rješava Eulerovom formulacijom. U svrhu reduciranja računalnih zahtjeva kapljice spreja podjednakih veličina i fizikalnih svojstava se grupiraju u skupine kapljica, tzv. parcele. Kretanje parcela se opisuje jednadžbama baziranim na drugom Newtonovom zakonu koje uzimaju u obzir sve relevantne sile na kapljice. Povezivanje između parcela i plinovite faze ostvaruje se kroz izvorske članove u jednadžbama održanja mase, energije i količine gibanja. Isto vrijedi i za povezivanje modela filma kapljevine na stjenci s plinovitom fazom.

Razvijeni matematički modeli implementirani su upotrebom korisničkih funkcija u programskom jeziku FORTRAN koje su povezane s glavnim rješavačem. Nakon kodiranja i implementacije svih korisničkih funkcija mogu se definirati validacijske simulacije. One uključuju generiranje računalne mreže, postavljanje početnih i rubnih uvjeta, odabir primjerenih shema diferencije te ostalih relevantnih parametara samog rješavača. Nakon pokretanja testnih kalkulacija očekuje se da će biti moguće simulirati realne industrijske geometrije.

Konačni cilj je dobiti rezultate svih relevantnih kemijskih i fizikalnih fenomena u područjima definiranim samim istraživanjem, a koji će biti zadovoljavajući kako na

kvalitativnoj, tako i na kvantitativnoj bazi. Zbog bolje preglednosti i unutarnje koherentnosti rad će biti podijeljen na nekoliko dijelova kako slijedi.

U prvom dijelu dan je pregled trenutnog stanja odabranog područja istraživanja kroz uvid dobiven u dostupnu i relevantnu literaturu. Također je definirana hipoteza doktorata i ciljevi istraživanja.

Drugi dio donosi pregled najvažnijih matematičkih modela koji čine numerički okvir računalne dinamike fluida u odabranom području istraživanja, kao i opće modele sadržane u računalnoj dinamici fluida kao istraživačkoj metodologiji.

Treći dio započinje sa samim doprinosom provedenog istraživanja kroz prilagodbu i implementaciju redukcijskog sedmostepenog modela NOx-a od Brouwera za primjenu u SNCR procesima. Također su dane osnovne jednadžbe Lagrangeovog spreja.

Četvrti dio teze donosi analizu i modeliranje filmova kapljevine na stjenci. Dan je model otkidanja filma kapljevine na stjenci prilikom nailaska na oštar rub iz literature koji je prošao višestruku eksperimentalnu provjeru te je prilagođen za primjenu u RDF-u. Nadalje, dana je analiza i modeliranje isparavanja višekomponentnih filmova kapljevine na stjenci. Napravljena je svojevrsna fuzija dostupnih modela uzimajući u obzir prednosti i nedostatke svakoga od njih, pri tome imajući na umu kompromis između točnosti rezultata i vremena računanja. Kraj četvrtog dijela predstavlja adpataciju i implementacija modela ureinih depozita i njihovog termičkog razlaganja te povezivanje s kemijskim reakcijama i vrstama danim u plinskoj fazi iznad depozita. Pregled dosadašnje literature ne ukazuje na postojanje sličnih modela unutar dostupnih kodova za računalnu dinamiku fluida, stoga će ovaj dio rada predstavljati izvorni znanstveni doprinos.

Peti dio je posvećen verifikaciji i validaciji implementiranih modela. Gdje god je bilo moguće rezultati razvijenih modela su uspoređeni s dostupnim eksperimentalnim podacima. Kriterij odvajanja filma je verificiran samo na fizikalnog promišljanja jer nisu pronađene korelacije koje bi dale uvid u svojstva odvojene kapljevine. Razvijeni model višekomponentnog isparavanja uspoređen je s eksperimentalnim mjerenjima provedenim od strane Wittiga i sur., koji su istraživali isparavanje filma kapljevine sastavljenog od jednakih masenih udjela vode i etanola unutar uskog raspora visine 3.9 mm. Model termičke dekompozicije ureinih depozita validiran je na eksperimentalnim rezultatima Bracka i suradnika koji daju rezultate termičke razgradnje uree i viših nusproizvoda, poput biureta i cijanurne kiseline. Model redukcije NOx-a je validiran na relativno jednostavnoj geometriji cijevi eksperimentalnog reaktora, ali njegova primjenjivost je također provjerena na realnom industrijskom spaljivaču komunalnog otpada.

Posljednji dio teze sadrži zaključak na temelju dobivenih rezultata provedenog istraživanja te smjernice i preporuke za daljnji rad.

Znanstveni doprinos rada

Glavni znanstveni doprinos ovog doktorskog rada je daljnji razvoj numeričkog okvira filma kapljevine na stjenci kroz razvoj, adaptaciju i implementaciju numeričkih modela s krajnjim ciljem povećanja točnosti i primjenjivosti alata računalne dinamike fluida u području razvoja inženjerskih sustava izgaranja u industriji i transportu. Matematički model kriterija otkidanja filma kapljevine prilikom nailaska na oštri rub adaptiran je i implementiran u numeričko okruženje komercijalnog koda za RDF, kao i sedmostepeni mehanizam za redukciju NOx-a u SNCR procesu. Nadalje, osobiti znanstveni doprinos rada je razvoj dva modela višekomponentnog isparavanja filma kapljevine na stjenci te implementacija i adaptacija modela termalne dekompozicije ureinih depozita Bracka i suradnika unutar komercijalnog koda za računalnu dinamiku fluida, pošto pregled postojeće literature nije otkrio nijedan takav model zadovoljavajuće točnosti. Parcijalni tlak pojedine komponente u filmu na granici između filma i plinske faze izračunat je korištenjem UNIFAC metode koja uzima u obzir međuutjecaj molekularne strukture pojedinih komponenata u smjesi. To omogućuje točniji izračun koncentracija koje imaju presudan utjecaj na brzinu isparavanja. Pregledom dostupne literature ustanovljeno je da je sličan pristup napravljen jedino kod opisivanja kapljica spreja.

Svi nabrojani modeli omogućuju proširenje numeričkog okvira filma kapljevine na stjenci i Lagrangeovog spreja te se s dovoljnom pouzdanošću, a koja je dokazana validacijom s dostupnim eksperimentalnim ispitivanjima, mogu koristiti za razvoj modernih inženjerskih sustava.

KEY WORDS

analytical force balance;

catalyst;

computational fluid dynamics;

Eulerian approach;

film roughness;

film rupturing;

gas aftertreatment;

Lagrangian spray;

multicomponent evaporation;

NOx reduction;

reaction kinetics;

selective catalytic reduction;

selective non-catalytic reduction;

turbulent boundary layer;

UNIFAC method;

urea deposits;

urea thermal decomposition;

urea water solution;

wall function;

wall film

KLJUČNE RIJEČI

analitička ravnoteža sila;

katalizator;

računalna dinamika fluida;

Eulerov pristup;

hrapavost filma

otkidanje filma;

obrada ispušnih plinova;

Lagrangeov sprej;

višekomponentno isparavanje;

NOx redukcija;

reakcijska kinetika;

selektivna katalitička redukcija;

selektivna nekatalitička redukcija;

turbulentni granični sloj;

UNIFAC metoda;

depoziti uree;

termalna dekompozicija uree;

vodena otopina uree;

zidna funckija;

film na stjenci

1. INTRODUCTION

Rising concerns about global climate changes, together with increase in world population and energy demand, that are met mostly using fossil fuels, call for change in society development, urging it to be more sustainable. Main goals toward achieving sustainable development are clear: using more renewable energy resources, increase in energy efficiency and reduction in harmful emissions. The ways to achieve them and areas of human activities that need to be modified are extremely diverse. Automotive sector and industry are, on the global scale, one of the main pollutants and are forced by environmental regulations to minimize their impact. Clearly, the industry and transport are facing major challenges that can be met only by development of new and more efficient systems using advanced tools for product development, one of which is computational fluid dynamics (CFD).

The liquid film flow sheared by an external air flow field is a physical phenomenon encountered in many engineering applications such as: burners, rain on vehicle windows and aircraft wings, rocket nozzles, mist eliminators, heat exchangers, steam turbine blades and especially internal combustion (IC) engines, where its proper description is important condition in order to comply with stringent environmental regulations. In IC engines, it has been observed that the unburned fuel that goes directly into the manifold causes an increase in emissions of unburned hydrocarbons in the petrol engines, and larger production of soot in the compression-ignited engines, especially under cold start conditions. The quality of mixing between the gas phase and the liquid film vapour is crucial for efficient operation of chemical reactors utilizing favourable mass and heat transfer characteristics of the liquid film. Also, injection of precursor substance into exhaust gases before the catalyst leads to the formation of liquid wall film due to unsteady engine working conditions. Above mentioned examples demonstrate the importance of an accurate prediction of the wall film behaviour. From a CFD standpoint, the challenge is to model an already complex set of processes and phenomena, together with the additional complication of handling various cell types in the dynamically changing geometry and mesh topology of an engine simulation. This research will deal with further improvement of Eulerian wall film and Lagrangian spray framework by further improvement, development, implementation and validation of numerical models, with the final aim of enabling more accurate and computationally efficient CFD calculations of complex physical and chemical phenomena of spray and liquid wall film taking part in

various engineering devices from industry and transport. In order to improve existing framework, drawbacks of current models are identified by literature review described in the following section. Four different areas are going to be addressed, all of which could be found within different industrial applications (e.g. internal combustion engines, exhaust gas aftertreatment systems, chemical reactors, etc.) – liquid film rupturing, multicomponent liquid film evaporation, urea deposits chemical kinetics and deNOx from exhaust gases with selective non-catalytic reduction.

Multicomponent evaporation modelling approach can be generally divided into two model groups: discrete multicomponent models and continuous multicomponent models [1]. Discrete multicomponent evaporation models track individual fuel components and enable direct coupling of reaction kinetics to the individual fuel components, whilst continuous multicomponent models are based on the continuous thermodynamic method and describe fuel composition as continuous distributed function with respect to some parameter, such as the molecular weight [2]. The latter approach decreases computational demands compared to the former one, but tends to be inaccurate if detailed chemical calculations are needed, or in the case of mixtures composed of large number of components. As current demands for computational simulation accuracy are relatively high, this section will only deal with discrete multicomponent evaporation models. O'Rourke and Amsden [3] showed that the evaporation affects structure of the turbulent boundary layer near the wall due to perpendicular velocity component of evaporated chemical species. In order to properly describe this effect, they have derived provisional wall functions that inhibit transport and reduce to standard ones in the case of walls without the wall film. Zeng and Lee [4] have suggested the model for multicomponent liquid wall film evaporation that is basically generalization of the model of O'Rourke and Amsden to more components. In their work they modelled film concentrations and temperature non-uniformity by employing third order polynomial. Torres and al. [5] took this approach one step further by discretizing liquid film. That way, a higher calculation accuracy is achieved, but at the expense of calculation time. Ebrahimian [6] has developed the most accurate model of liquid film evaporation which, like the approach in [4], employs third order polynomial for film temperature distribution. However, it also takes into account the chemical species enthalpy diffusion, Stefan flow and generalizes wall functions, developed on the basis of the direct numerical simulation [7], on the multicomponent evaporation case. In spite of all the advantages of this model, its validation is still missing.

Although the behaviour of thin liquid wall films has been covered by numerous numerical, theoretical and experimental studies, the same cannot be stated for the phenomena

of liquid wall film encountering sharp edge. With respect to the insight given by the literature review, thus far only five published studies are dealing with construction of the theoretical model. Owen and Ryley were first to consider the flow of thin liquid films around the edge [8]. Separation criterion has been derived from the balance of forces on the infinitesimal volume of film that is rotated about the edge. Second approach was given by O'Rourke and Amsden [3] and it is the simplest one, because only pressure difference on the both sides of the film is taken into account. This approach has not been thoroughly validated experimentally, and comparison with available measurements is not satisfactory. Maroteaux et al. [9] introduced an alternative way of describing the film rupturing by analysis of surface instabilities that occur as a result of film inertial forces. However, this method met serious criticism [10] and showed discrepancies from experimental measurements [11]. The recent work of Friedrich et al. [12] focused on the drawbacks of the previous approaches in order to overcome them. The separation criterion has been derived from the force balance on the control volume, which includes ligament of film that is beginning to detach from the edge. Surface tension, gravity and inertia of the film were taken into account. Although this approach has a tendency toward premature rupturing prediction [13], it is considered to be fairly reliable [14]. Finally, the latest approach is the one developed by Bacharoudisa et al. [15], which combines the force balance that has been further extended to include the wave characteristics of the film. This model enables reliable prediction of the rupturing only for an angle of 90°, which limits its practical application.

Selective Catalytic Reduction (SCR), as one of the most promising methods for reducing nitrogen oxides from diesel engines, raises new challenges for designers in the field of the liquid wall film behaviour. The current state of development of numerical models provides reliable simulation of the spray preparation, especially regarding the uniformity of distribution of the reducing agent and the flow field before the catalysts [16] and the chemical reactions that take place within the SCR catalyst [17]. However, a reliable prediction of creation and behaviour of deposits of urea by means of numerical simulation still remains the topic of the latest research efforts. Despite the fact that experimental investigation of urea decomposition has taken place for many years, modelling of the chemical kinetics of urea deposits began only recently. Ebrahimian et al. [18] were the first to introduce a reduced model of the kinetics of urea deposits that can be coupled with CFD code. Their research is based on experimental findings of Schaber et al. [19] and Lundstrom et al. [20]. The model is composed of 12 reactions describing the thermolysis of urea and the creation and decomposition of cyanuric acid and biuret. It is able to describe the effect of changing heating

rate, but is based on the known initial weight of the sample, which limits its applicability. In fact, in the real exhaust systems, the mass of urea deposits varies depending on the current temperature, concentration of products in the gas phase above the deposit, wall temperature and injected mass of the spray, and is not known in advance. Although their model showed good agreement with the measured results of Schaber et al. [19], decomposition and behaviour of biuret, cyanuric acid and ammelide was not predicted well. Also, the model does not take into account the effect of geometry of the substrate on the process of decomposition, shown in [21]. Identified deficiencies were corrected by Brack et al. [22] by developing the new reduced model based on fifteen reactions describing thermolysis of urea and the creation and degradation of biuret and cyanuric acid. By using results given in [19], they divided the process of urea thermolysis into three areas in which different deposits have the dominant role. Each dominant deposit substance was individually experimentally analysed, the dominant reaction pathways were determined and, after optimization of individual stages, all the explored mechanisms were fit into the complete process of urea decomposition. It should be noted here that Brack et al. [22] have solved the problem of influence of deposit's geometry [21] by taking into account the area of free surface of the substrate that has great impact on the further course of isocyanic acid evaporation.

However, the available literature review didn't reveal any reliable chemical kinetic model implemented within available CFD code. Thus, one of the thesis goals is going to be implementation and adjustment of the kinetical model of urea deposition from Brack et al. on the wall film model as a step in the process of description of urea deposits' influence on the overall domain of the real flue gas aftertreatment system.

Methods of NOx control may be categorised into primary methods, which prevent formation of NOx and secondary NOx control methods, which are focused on the reduction of already formed NOx [23]. Selection of an individual method or combination of methods is always dependent on economic balances and legislation.

First option of primary NOx control methods consists of regulation of the excess air, keeping at the same time in mind the fact that it directly affects unburned carbon emissions. The combustion air staging creates fuel-rich primary zone and fuel-lean secondary zone, suppressing that way creation of fuel and thermal NOx. Similar to combustion air, fuel can also be staggered through creating a fuel-rich secondary combustion zone, where NOx formed in the primary combustion zone is decomposed. Exhaust gas recirculation, a technique frequently employed in modern internal combustion engines [24], represents also one of the primary NOx reduction measures that can significantly reduce thermal NOx generation by

lowering combustion temperatures and excess air. Tightened NOx emission standards [25,26] on industrial emissions from combustion plants cannot be met using the described primary NOx reduction techniques anymore. Also, it is difficult to implement those techniques into existing facilities. Considering the stated, it is clear that the answer to those challenges should be in utilising exhaust gas aftertreatment. Some new technologies emerged during the last few years, such as pulsed corona discharge and electron beam flue gas treatment [27]. However, selective non-catalytic reduction (SNCR), as well as selective catalytic reduction (SCR), are proven to be optimal from both the cost and the NOx reduction efficiency standpoint.

SCR offers higher denitrification efficiencies with respect to SNCR, although the investment cost is much higher [28] and it is not suitable for retrofitting due to clogging problems and loss of catalytic efficiency in such cases. On the other side, SNCR is a proven cost-effective secondary method of NOx control from big stationary sources such as power plants, incinerators, boilers and cement calciners. The process is operated by the controlled injection of reducing agents such as ammonia or urea [29]. The performance of SNCR process has been shown to be influenced by reducing agent residence time, temperature profile in reaction zone, quality of mixing of reagent with flue gases, concentration of NOx in flue gases, ammonia slip and normalised stoichiometric ratio [30]. Residence time is a factor whose increase enables longer contact between reducing agent and NOx. Its value is highly dependent on flow geometry and velocities inside the region where SNCR is taking place. Most researchers agree that optimum SNCR process is taking place within relatively narrow temperature range between 800 and 1100 °C [28]. Above 1100 °C ammonia tends to oxidise, while below 800 °C the reduction rate is too slow. Mixing quality of reagent and exhaust gases depends upon velocities and swirl in the reaction zone, and also upon the injecting conditions, whilst the concentration of NOx in flue gases could be affected using primary NOx reduction measurements, and also differs between various applications such as power plants, utility boilers, and incinerators. Normalised stoichiometric ratio (NSR) refers to the ratio between reducing agent and NOx. It is preferable to have it high. However, one must take into account also toxic ammonia slip, whose levels are limited by various legislations and norms. Previous research showed that optimum NSR value in terms of NO reduction efficiency is between 1.5 and 2 [31].

All operating conditions are interdependent and show that, although SNCR process is principally very simple, design of an optimum process or retrofitting an existing facility can be quite complex. There are several arguments for using computational fluid dynamics in SNCR applications. Firstly, in view of shortening the development cycles and reducing

development costs, an early stage assessment of the performance of different setups and various design parameters becomes very important [32]. Also, in reality, it is very difficult to study SNCR processes in large utility boilers directly through measurements because of the limited experimental access. Large space and strong turbulence in such facilities cause a very poor accuracy and hinder the essential operational characteristics. Finally, improved computational design tools are needed for design and optimisation of SNCR performance required by tightened emission regulations and demand for decrease in cost of a NOx emission controlling system [33]. By incorporating suitable mathematical representation of relevant physical phenomena that are taking place in SNCR system, CFD can give detailed insight into all flow variables and replace expensive and intrusive experimental tests [34].

Taking into account all stated, the purpose of this thesis is additional improvement of the Eulerian liquid wall film model through further development and implementation of numerical models, with the ultimate goal of achieving more accurate and computationally efficient calculations of complex chemical and physical phenomena associated with various applications in industry and transport. Specific research goals are adaptation and implementation of liquid film rupturing model of Friedrich et al. [12], development and implementation of two multicomponent liquid film evaporation models on the basis of momentum and mass transfer analogy and modified wall functions derived by O'Rourke and Amsden [3], modelling of urea deposits chemical kinetics on the basis of work carried out by Brack [22] and adaptation and implementation of reduced deNOx chemical kinetics model for SNCR applications into the numerical CFD framework.

Thesis Hypothesis

Research hypothesis is that improved, adopted and newly developed numerical models are going to enable numerical simulations of multicomponent liquid wall films and that they could be then used in various industrial applications.

Research Methods

The developed mathematical models are going to be implemented by employing FORTRAN-based user functions that are connected to the main solver. After coding and implementation of all user functions, the validation simulations can be defined. They include generation of computational mesh, setting of initial and boundary conditions and selection of appropriate differencing schemes and other relevant parameters of the solver. After successful test calculations, real industrial geometries are expected to be simulated.

The ultimate goal is to obtain results of all relevant physical and chemical phenomena defined within research that will be satisfactory, both qualitatively and quantitatively. In order to achieve better clarity and internal coherence, the work will be divided into several sections, as follows.

The second chapter brings an overview of the most important mathematical models which form the numerical framework of the computational fluid dynamics in the chosen research area, as well as general models of computational fluid dynamics as a research method. The following part starts with the actual contribution of performed research through adjustment and implementation of the seven step kinetic model for Brouwer for SNCR applications. Also, the basic spray governing equations are presented.

The fourth part brings the analysis and modelling of liquid wall film. Existing numerical framework is described together with implemented models of multicomponent evaporation, urea deposits thermal decomposition and criterion for onset of film rupturing. For the purpose of assessing the multicomponent liquid film evaporation, two approaches are utilized: the one based on the wall functions from O'Rourke and Amsden, and the other based on the analogy between momentum and mass transfer. The end of fourth part focuses on adaptation and implementation of chemical kinetics of urea thermal decomposition developed by Brack et al. [22], and its coupling with the liquid wall film model.

The fifth part of the thesis brings verification and validation of implemented models. Where possible, the developed models were subjected to comparison with available experimental data. The separation criterion from Friedrich has been verified only on the basis of physical reasoning, since there are no correlations describing properties of ruptured film. Multicomponent evaporation has been compared with the experiment carried out by Wittig et al. [35], where evaporation of the liquid film composed of equal mass fractions of water and ethanol has been investigated in small gap with height of 3.9 mm. Urea deposits decomposition model was validated following experiments from Brack et al. [22], where urea and its by-products were analysed in quiescent conditions. The implemented and adjusted seven step reaction mechanism from Brouwer is validated on a simple experimental pipe reactor, but its applicability is also tested on actual industrial case of a municipal incinerator.

The final part of the thesis contains conclusion statements that are based on the obtained results, as well as guidelines and recommendations for further research.

Scientific Contribution

The scientific contributions of this thesis are:

- Adaptation and implementation of the wall film rupturing model from Friedrich et al. to the numerical CFD framework, as well as the seven step reaction mechanism for SNCR process modelling;
- Development and implementation of two multicomponent liquid film evaporation models on the basis of momentum and mass transfer analogy and modified wall functions derived by O'Rourke and Amsden. Particular scientific contribution presents implementation of the UNIFAC method for activity coefficients calculation which is employed in the area of liquid wall films for the first time;
- Numerical modelling of urea deposits formation and thermal decomposition on the basis of the work performed by Brack et al.

2. FUNDAMENTAL EQUATIONS OF FLUID FLOW

Computational fluid dynamics today encompasses immensely wide area, but in a nutshell it can be said that it deals with solving problems of fluid mechanics by employing numerical method. Fluid mechanics is one of the branches of continuum mechanics which is based on one fundamental assumption – that of the continuum. Although it has been shown during the 20th century that matter has a discrete structure on the microscopic level, the continuum concept has proven to be useful because it allows point definition of relevant physical quantities and the usage of calculus as the main tool of continuum mechanics. The continuum approach is valid up until even the smallest volume of interest contains a sufficient number of molecules so that statistic average has meaning [36]. Talking more precisely in the area of fluid mechanics, if we observe Knudsen number defined as:

$$Kn = \bar{l} / L \tag{1}$$

where L represents characteristic linear dimension of observed domain and $\bar{l}$ is average free path length of the molecule, it can give us quantitative criterion for validity of continuum approach. Namely, numerous observations showed that its value should be below ≈0.1. Above that threshold other scientific disciplines are employed.

The foundation of continuum mechanics represents four fundamental conservation laws: mass conservation law, momentum conservation law, angular momentum conservation law and energy conservation law. Branches of continuum mechanics are separated according to constitutive equations inherent to each of them. In order to derive constitutive equations, there are two possible pathways – inductive and deductive approach. The inductive approach starts from experimental results by idealizing and simplifying them. It has historically preceded the deductive approach and is especially relevant to technical applications. On the other side, the deductive approach is more systematic and is based on the constitutive equations axioms [37]:

- coordinate invariance;
- causality principle;
- principle of determinism;
- principle of local action;
- equipresence principle;

- principle of fading memory;
- principle of physical consistency;
- principle of material frame-indifference.

After the basic assumptions are adopted, it can be proceeded to the definition of conservation equations of fluid mechanics. In this thesis, only Newtonian fluids are observed, so all relations are defined accordingly.

2.1. Conservation equations

Mass conservation law (continuity equation) for differential element of fluid in Cartesian coordinate system can be expressed as follows:

$$\frac{\partial \rho}{\partial t} + \frac{\partial}{\partial x_j}(\rho u_j) = 0 \qquad \textbf{(2)}$$

where ρ is fluid density, t represents time, x_j Cartesian coordinates and u_j velocity vector components. For incompressible fluid, equation (2) states that the divergence of velocity is equal to zero.

Momentum conservation law for infinitesimal Newtonian fluid element could be defined only after constitutive relations for Newtonian fluid are given. In general, fluid stress tensor can be written as:

$$\sigma_{ij} = -p\delta_{ij} + \tau_{ij} \qquad \textbf{(3)}$$

where σ_{ij} is stress tensor, p is thermodynamic pressure, δ_{ij} is Kronecker delta and τ_{ij} represents viscous stresses. Newtonian fluid is by definition a fluid in which the viscous stresses are linearly proportional to the rate of deformation:

$$\tau_{ij} = \mu\left(\frac{\partial u_i}{\partial x_j} + \frac{\partial u_j}{\partial x_i}\right) - \frac{2}{3}\mu\delta_{ij}\frac{\partial u_k}{\partial x_k} \qquad \textbf{(4)}$$

In the above expression μ represents fluid viscosity and it should be noted that was derived with assumption of isotropic fluid and negligible volume viscosity [38]. Taking into account equation (4) momentum conservation law for infinitesimal, incompressible Newtonian fluid element can be stated as:

$$\frac{\partial}{\partial t}(\rho u_i) + \frac{\partial}{\partial x_j}(\rho u_i u_j) = -\frac{\partial p}{\partial x_i} + \mu\frac{\partial^2 u_i}{\partial x_j \partial x_j} + \rho f_i \qquad \textbf{(5)}$$

Momentum conservation law equations for Newtonian fluid together with continuity equation (2) are also called Navier-Stokes equations according to the researchers who were first to derive them.

Angular momentum conservation law reduces itself down to the fact that the stress tensor is symmetric tensor in the case of non-polar continuum:

$$\sigma_{ij} = \sigma_{ji} \tag{6}$$

The final basic conservation law that yet has to be defined is the energy conservation law. However, one more constitutional expression is missing – the one that defines heat diffusivity, the so called Fourier's law:

$$q_i = -\lambda \frac{\partial T}{\partial x_i} \tag{7}$$

where q_i is heat flux density vector, λ is fluid's thermal conductivity and T is thermodynamic temperature. Again, above express is valid only for isotropic fluid. With defined heat diffusivity, energy conservation law can be written as:

$$\frac{\partial}{\partial t}(\rho i) + \frac{\partial}{\partial x_j}(\rho i u_j) = -p\frac{\partial u_j}{\partial x_j} + \frac{\partial}{\partial x_j}(\lambda \frac{\partial T}{\partial x_j}) + \rho f_i v_i + \frac{\partial(\tau_{ji} v_i)}{\partial x_j} \tag{8}$$

where i is specific internal energy of fluid.

Now that the basic conservation laws are defined, they can be rearranged in order to emphasize some similarity between them. Modification of equations (5) and (8) yields:

$$\frac{\partial}{\partial t}(\rho u_i) + \frac{\partial}{\partial x_j}(\rho u_i u_j) = -\frac{\partial p}{\partial x_i} + \frac{\partial}{\partial x_j}\left(\mu \frac{\partial u_i}{\partial x_j}\right) + S_m \tag{9}$$

$$\frac{\partial}{\partial t}(\rho i) + \frac{\partial}{\partial x_j}(\rho i u_j) = -p\frac{\partial u_j}{\partial x_j} + \frac{\partial}{\partial x_j}(\lambda \frac{\partial T}{\partial x_j}) + \Phi + S_i \tag{10}$$

Significant commonalities between presented governing equations justify introduction of a general variable φ, which enables us to write general conservative form of all fluid flow equations, presented in the forthcoming section.

2.2. General transport equation

General transport equation of scalar quantity could be decomposed on characteristic members, each having distinguished physical meaning and inherent properties.

$$\frac{\partial}{\partial t}(\rho\varphi) + \frac{\partial}{\partial x_j}(\rho\varphi u_j) = \frac{\partial}{\partial x_j}(\Gamma_\varphi \frac{\partial \varphi}{\partial x_j}) + S_\varphi \tag{11}$$

First term on the left hand side of the equation (11) represents time rate of change of general variable φ, second term on the same side is convective transport of the same variable, first term on the right hand side describes diffusional transport of φ, whilst the last term of the equation represents source/sink of the variable φ due to various mechanisms, not being

covered by the three previous ones. General transport equation (11) represents basic equation upon which the numerical theory of CFD is being built.

2.3. Turbulent flows

Turbulence represents highly irregular and apparently random regime of fluid flow. The great majority of fluid flows occurring in the nature and engineering applications are turbulent, so it is obvious right from beginning why engineers have a necessity for mathematical apparatus that is going to enable them prediction of turbulent flow.

Turbulence has also some distinct characteristics which, depending on the application of interest, could be viewed as beneficiary or harmful. As far as technical applications are concerned, diffusivity is the most important turbulent feature [39]. Turbulent vortices of a wide range of frequencies and wavelengths cause improved mixing among fluid particles enabling thus higher possibility that spatially separated particles meet and exchange physical property (momentum, heat, etc.). Turbulent diffusivity has tendency to make physical properties more homogenous in flow domain. Increased energy dissipation is a turbulence property which follows directly as a consequence of turbulent diffusivity. Namely, the same turbulent eddies which are important for turbulent diffusivity, are also responsible for draining more kinetic energy from the main flow. If there is no continuous supply of energy, turbulence decays promptly [39]. Finally, in order to better grasp turbulent energy dissipation we will employ concept of turbulent energy cascade. Turbulence consists of spectrum of eddies ranging continuously from the biggest ones that have characteristic size comparable to the width of the flow to smallest ones fixed by viscous dissipation of energy [40]. The largest eddies interact with the energy of the main flow and pass the energy to smaller eddies through process called vortex stretching. Vortex stretching continuous over the whole range of wavelengths until finally, kinetic energy is dissipated by the means of viscous forces.

The stochastic nature of turbulent flows makes it impossible to solve them analytically. For engineering purposes, usually some average integral quantities are sufficient, and therefore, next section shows one of statistical approaches for describing turbulence.

2.3.1. Averaging of conservation equations

As can be seen in Figure 1, instantaneous quantity of some general transport scalar variable φ could be represented as a sum of time averaged and fluctuating component:

$$\varphi = \overline{\varphi} + \varphi' \qquad \textbf{(12)}$$

Time averaged component is by definition:

$$\overline{\varphi} = \frac{1}{\Delta t}\int_{t}^{t+\Delta t} \varphi(x_i, t)dt \qquad \textbf{(13)}$$

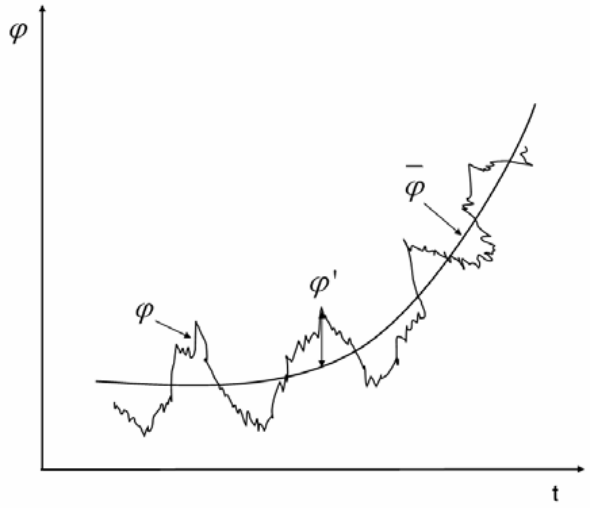


Figure 1. Turbulent fluctuation of general physical quantity [41]

After the application of the above described averaging procedure, also known as Reynolds averaging, which consists of algebraic manipulation and simplifications, the averaged continuity and momentum equations could be written as:

$$\frac{\partial \overline{u}_j}{\partial x_j} = 0 \qquad \textbf{(14)}$$

$$\rho\frac{\partial \overline{u}_i}{\partial t} + \frac{\partial}{\partial x_j}(\rho \overline{u}_i \overline{u}_j) = -\frac{\partial \overline{p}}{\partial x_i} + \frac{\partial}{\partial x_i}\left[\mu\left(\frac{\partial \overline{u}_i}{\partial x_j} + \frac{\partial \overline{u}_j}{\partial x_i}\right) - \overline{\rho u_i' u_j'}\right] \qquad \textbf{(15)}$$

A set of time-averaged equations (14) and (15) is called Reynolds-averaged Navier-Stokes equations. By observing this system, it can be clearly seen that there is more unknowns than equations due to additional term $\overline{\rho u_i' u_j'}$. This tensor is called Reynolds stress tensor. By averaging Navier-Stokes equations, piece of information from Navier-Stokes equations was lost. In order to restore this information, it is necessary to introduce infinitely many correlations for pressure and velocity field. This is also known in literature as the closure problem [42]. In order to solve this problem, turbulence models are employed.

2.3.2. Turbulence modelling

The approach for turbulence modelling presented in this section is based upon RANS (Reynolds-Averaged Navier-Stokes) equations. Turbulence models can be divided based on the correlation for velocity for which the transport equation is solved on first, second and third

order models. In the first orders models Reynolds stress term, defined in the previous section is modelled, most commonly according to the Boussinesq hypothesis. It states the analogy with Newton viscosity law:

$$-\overline{\rho u_i' u_j'} = \mu_t \left(\frac{\partial \bar{u}_i}{\partial x_j} + \frac{\partial \bar{u}_j}{\partial x_i} \right) - \frac{2}{3} \rho \bar{k} \delta_{ij} \quad \textbf{(16)}$$

where μ_t is turbulent viscosity and $\bar{k}$ is turbulent kinetic energy. With the Boussinesq hypothesis six components of Reynolds stresses are replaced with the one field of turbulent viscosity. Boussinesq hypothesis leads directly to the Prandtl turbulent viscosity model, which is based on the analogy with the molecular viscosity, defined by the kinetic theory of gases:

$$\mu_t = \rho l_t v_t \quad \textbf{(17)}$$

where l_t is characteristic turbulent length and v_t is characteristic velocity of turbulent fluctuations. Expression (17) represents the base for a number of turbulence models which differ according to the definition of l_t and v_t. This section will present two models that were employed in this thesis, namely *k-ε* and *k-ζ-f* models.

<u>*k-ε* model</u>

In the *k-ε* model turbulent viscosity is defined with the following expression:

$$\mu_t = C_\mu \rho \frac{\bar{k}^2}{\bar{\varepsilon}} \quad \textbf{(18)}$$

where C_μ is model constant, $\bar{k}$ is turbulent kinetic energy and $\bar{\varepsilon}$ is turbulent energy dissipation rate. $\bar{k}$ is defined as:

$$\bar{k} = \frac{1}{2} \overline{u_i' u_i'} \quad \textbf{(19)}$$

whilst $\bar{\varepsilon}$ can be described as:

$$\bar{\varepsilon} = \nu \overline{\frac{\partial u_i'}{\partial x_j} \frac{\partial u_i'}{\partial x_j}} \quad \textbf{(20)}$$

where ν is kinematic viscosity of the fluid.

In order to compute those additional two quantities necessary for calculation of turbulent viscosity in equation (18), the model employs additional transport equations for those quantities. The final form of the modelling equation for turbulent kinetic energy is [43]:

$$\frac{\partial}{\partial t}(\rho \bar{k}) + \frac{\partial}{\partial x_j}(\rho \bar{u}_j \bar{k}) = \frac{\partial}{\partial x_j} \left[\left(\mu + \frac{\mu_t}{\sigma^k} \right) \frac{\partial \bar{k}}{\partial x_j} \right] + G - \rho \bar{\varepsilon} \quad \textbf{(21)}$$

In the above expression σ^k represents model constant and G is generation of turbulent kinetic energy:

$$G = \mu_t \left(\frac{\partial \bar{u}_i}{\partial x_j} + \frac{\partial \bar{u}_j}{\partial x_i} \right) \frac{\partial \bar{u}_i}{\partial x_j} \tag{22}$$

The final form of the modelling equation for the turbulent energy dissipation rate is:

$$\frac{\partial}{\partial t}(\rho \bar{\varepsilon}) + \frac{\partial}{\partial x_j}(\rho \bar{u}_j \bar{\varepsilon}) = \frac{\partial}{\partial x_j}\left[\left(\mu + \frac{\mu_t}{\sigma^\varepsilon} \right) \frac{\partial \bar{\varepsilon}}{\partial x_j} \right] + C_1 G \frac{\bar{\varepsilon}}{\bar{k}} - C_2 \rho \frac{\bar{\varepsilon}^2}{\bar{k}} \tag{23}$$

The five model constants are not universal and must be adjusted to a specific problem. However, the default values covering wide range of practical turbulence problems are presented in the Table 1 [44].

Table 1. The values of the constants in the *k-ε* model

C_μ	C_1	C_2	σ^k	σ^ε
0.09	1.44	1.92	1.0	1.3

<u>*k-ζ-f* model</u>

k-ζ-f turbulence model is also based on the turbulent viscosity but Durbin's elliptic relaxation concept [45] is employed. This model solves a transport equation for the velocity scales ratio $\zeta = \frac{\overline{v^2}}{\bar{k}}$ instead of $\overline{v^2}$, thus making it more robust and less sensitive to grid nonuniformities [46].

In the *k-ζ-f* turbulence model turbulent viscosity is represented as:

$$\mu_t = C_\mu \rho \zeta \bar{k} \tau \tag{24}$$

where ζ is velocity scales ratio and τ is turbulent time. The equation for turbulent kinetic energy could be written as follows:

$$\frac{\partial}{\partial t}(\rho \bar{k}) + \frac{\partial}{\partial x_j}(\rho \bar{u}_j \bar{k}) = \frac{\partial}{\partial x_j}\left[\left(\mu + \frac{\mu_t}{\sigma^k} \right) \frac{\partial \bar{k}}{\partial x_j} \right] + G - \rho \bar{\varepsilon} \tag{25}$$

Turbulent energy dissipation rate is described by the following expression:

$$\frac{\partial}{\partial t}(\rho \bar{\varepsilon}) + \frac{\partial}{\partial x_j}(\rho \bar{u}_j \bar{\varepsilon}) = \frac{\partial}{\partial x_j}\left[\left(\mu + \frac{\mu_t}{\sigma^\varepsilon} \right) \frac{\partial \bar{\varepsilon}}{\partial x_j} \right] + \rho \frac{(C_{\varepsilon 1} G - C_{\varepsilon 2} \varepsilon)}{\tau} \tag{26}$$

Transport equation for velocity scales ratio is:

$$\frac{\partial}{\partial t}(\rho\zeta)+\frac{\partial}{\partial x_j}(\rho\bar{u}_j\zeta)=\frac{\partial}{\partial x_j}\left[\left(\mu+\frac{\mu_t}{\sigma^{\zeta}}\right)\frac{\partial\zeta}{\partial x_j}\right]+\rho f-\rho\frac{\zeta}{\bar{k}}G \quad \textbf{(27)}$$

where σ^{ζ} is model constant and f is elliptic function calculated by the following equation:

$$L^2\frac{\partial^2 f}{\partial x_j\partial x_j}-f=\frac{1}{\tau}\left(C_1+C_2^{'}\frac{G}{\bar{\varepsilon}}\right)\left(\zeta-\frac{2}{3}\right) \quad \textbf{(28)}$$

In the above equation L represents turbulent length scale, where Kolmogorov length scale [47] is imposed as a lower bound and combined with Durbin's realizability constraint [48]:

$$L=C_L\max\left[\min\left(\frac{\bar{k}^{\frac{3}{2}}}{\bar{\varepsilon}},\frac{\bar{k}^{\frac{1}{2}}}{\sqrt{6}C_\mu|S|\zeta}\right),C_\eta\left(\frac{\nu^3}{\bar{\varepsilon}}\right)^{\frac{1}{4}}\right] \quad \textbf{(29)}$$

Similarly, turbulent time is defined by imposing Kolmogorov time scale [47] as a lower bound and combined with Durbin's realizability constraint [48]:

$$\tau=\max\left[\min\left(\frac{\bar{k}}{\bar{\varepsilon}},\frac{0.6}{\sqrt{6}C_\mu|S|\zeta}\right),C_\tau\left(\frac{\nu}{\bar{\varepsilon}}\right)^{\frac{1}{2}}\right] \quad \textbf{(30)}$$

In the above expressions (29) and (30) S is defined as follows:

$$S=\sqrt{\frac{1}{2}\left(\frac{\partial\bar{u}_i}{\partial x_j}+\frac{\partial\bar{u}_j}{\partial x_i}\right)\left(\frac{\partial\bar{u}_i}{\partial x_j}+\frac{\partial\bar{u}_j}{\partial x_i}\right)} \quad \textbf{(31)}$$

The default model constants appearing in equations (24) - (30), covering wide range of practical turbulence problems, are presented in the following Table 2.

Table 2. The values of the constants in the *k*-ζ-*f* turbulence model

C_μ	$C_{\varepsilon 1}$	$C_{\varepsilon 2}$	C_1	C_2'	σ^k	σ^ε	σ^ζ	C_L	C_η	C_τ
0.22	1.4(1+0.012/ζ)	1.9	0.4	0.65	1	1.3	1.2	0.36	85	6.0

Compared to previously described *k*-ε model, the *k*-ζ-*f* turbulence model dispenses with the conventional practice of introducing empirical damping functions. It is more suitable for strong swirling flows such as those that can be found in internal combustion engines. However, additional transport equation for calculation of ζ as well as additional differential equation for elliptic function *f* make this model more computationally demandable. It is up to the user to assess whether will employment of the *k*-ζ-*f* turbulence model bring much better accuracy compared to additional resources which should be employed for its solution.

2.4. Numerical procedure

Previous sections presented selected analytical equations of fluid mechanics and turbulence models. Those equations could be solved analytically only for limited number of very simplified cases, that barely have any technical importance. It is obvious that we should use increasingly available computing power for numerical approach, basis for which is general transport equation (11). The upcoming sections will present only the basic overview of numerical method employed in CFD.

2.4.1. Integral form of the transport equation

General transport equation (11) given in differential form has to be stated in the integral form in order to be applicable for the control volume discretization method [49]. By integrating the equation (11) over the control volume, integral form of this equation is obtained:

$$\frac{\partial}{\partial t}\int_{CV}(\rho\varphi)dV+\int_{CV}\frac{\partial}{\partial x_j}(\rho\varphi u_j)dV=\int_{CV}\frac{\partial}{\partial x_j}(\Gamma_\varphi\frac{\partial\varphi}{\partial x_j})dV+\int_{CV}S_\varphi dV \qquad \textbf{(32)}$$

2.4.2. Time discretization

In the case of transient simulations the time interval is also split into a finite number of time steps. Thus, the general transport equation could be written as:

$$\int_t^{t+\Delta t}\left[\frac{\partial}{\partial t}\int_{CV}(\rho\varphi)dV+\int_{CV}\frac{\partial}{\partial x_j}(\rho\varphi u_j)dV\right]dt=\int_t^{t+\Delta t}\left[\int_{CV}\frac{\partial}{\partial x_j}(\Gamma_\varphi\frac{\partial\varphi}{\partial x_j})dV+\int_{CV}S_\varphi dV\right]dt \qquad \textbf{(33)}$$

or in more compact notation:

$$\int_t^{t+\Delta t}\left[\frac{\partial}{\partial t}\int_{CV}(\rho\varphi)dV\right]dt=\int_t^{t+\Delta t}f(t,\varphi(t))dt \qquad \textbf{(34)}$$

where all the terms except transient one were cast on the right hand side.

By using explicit or forward Euler method of time discretization equation (34) can be expressed as:

$$\varphi^n=\varphi^o+f(t_o,\varphi^o)\Delta t \qquad \textbf{(35)}$$

This method is conditionally stable, i.e. if Courant number criterion is fulfilled and is the first order accurate.

In the case of implicit of backward Euler method, equation (34) is transformed into:

$$\varphi^n = \varphi^o + f(t_n, \varphi^n)\Delta t \quad \textbf{(36)}$$

This scheme is unconditionally stable and first-order accurate. However, it requires φ values at the new time level [50].

Finally, the Crank-Nicholson method uses linear interpolation between φ values at the old and new time level:

$$\varphi^n = \varphi^o + \frac{1}{2}\left[f(t_o, \varphi^o) + f(t_n, \varphi^n)\right]\Delta t \quad \textbf{(37)}$$

Crank-Nicolson method is second order accurate and unconditionally stable, but doesn't guarantee bounded solution [51].

2.4.3. Control volume discretisation

The main task of discretization method is transformation of initial system of partial differential equations into system of algebraic equations which can be easily tackled with appropriate numerical framework. The control volume discretization employed in this work divides the space of physical domain of interest into finite number of volumes that don't overlap. The computational nodes are located in the centres of these control volumes. It is assumed that any dependent variable is homogeneous within the control volume. The integration of the conservation equations is applied to every control volume. Consequently, the control volume discretization method will ensure the global conservation as one of its principal advantages.

2.4.4. Numerical schemes

The task of numerical schemes is calculating the value of the considered physical quantity on the sides of the control volumes. This is realized by taking into account the values at the centre of adjacent control volumes which have the observed side in common. Figure 2 gives schematic representation of computational node which will be used for definition of differencing schemes.

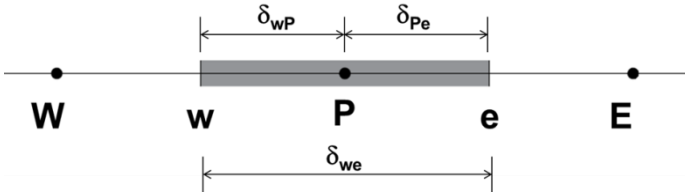


Figure 2. Schematic representation of computational node

Upwind differencing scheme (UDS), as its name implies, takes the physical value from the node of upstream control volume to represent the physical quantity at the border of two control volumes. Mathematical equivalent of this statement is:

$$\varphi_w = \begin{cases} \varphi_W \ for & F > 0 \\ \varphi_P \ for & F < 0 \end{cases} \quad \textbf{(38)}$$

The fact that this scheme is the first order of accuracy is the basic drawback of this scheme, and introduces false diffusion in numerical solution. In contrast, very simple calculation coefficient is an advantage of this scheme. If we consider that the coefficient are always positive, this scheme will never give unphysical oscillatory solutions, nor will diverge [52]. Due to mentioned advantages, this scheme is built into most commercial CFD software.

In the central differencing scheme (CDS) the value at the side is calculated using values at neighbouring nodes and multiplying those values with weighting factor that takes relative distance to each neighbouring node. In the case of uniform 1D mesh this can be written as (refer to Figure 2):

$$\varphi_e = \frac{\varphi_E + \varphi_P}{2} \quad \textbf{(39)}$$

This scheme is second order accuracy, it hasn't property of transportiveness and introduces ellipticity even in situations where equations are parabolic or hyperbolic [50]. This results in the need of setting the boundary conditions even on boundaries where, physically speaking, it is not necessary. As is the case with all higher order approximations, this scheme may produce oscillatory solutions [52].

Finally, the blended scheme will be presented here, which presents linear combination of UDS and CDS. Thus, it is possible to combine benefits of both schemes. Blended scheme can be written as follows:

$$\varphi_e = \gamma \varphi_e^{CDS} + (1-\gamma)\varphi_e^{UDS} \quad \textbf{(40)}$$

where γ is so called blending factor. Its value is in the range between 0 (UDS) and 1 (CDS).

2.4.5. Solution procedure

For every control volume, one equation in the following form is assembled:

$$a_P \varphi_P = \sum_{i=1}^{N} a_i \varphi_i + S_\varphi \quad \textbf{(41)}$$

Since every computational node is dependent on the values in neighbouring nodes, the ultimate result of general transport equation discretization on a given computational grid is a

system of non-linear algebraic equations which must be solved by an appropriate iterative technique [52]:

$$[A]\{\varphi\} = \{S\} \tag{42}$$

In the above expression $[A]$ represents matrix containing a_i and a_p terms from equation (41) for each control volume of computational domain, the vector $\{\varphi\}$ contains the dependent variables and finally, vector $\{S\}$ is vector of right hand side of equation (41), so called source term.

3. SELECTIVE NON-CATALYTIC REDUCTION

In order to accurately represent all relevant physical phenomena occurring during the injection of urea-water solution (UWS) into hot flue gases, mathematical description of following processes is needed:

- solution of gas phase;
- description of spray droplets motion inside the domain;
- evaporation of urea-water solution droplets;
- thermal decomposition of urea;
- chemical reactions taking place in the gas phase.

3.1. Description of spray droplets motion inside the domain

Experimental observations as well as the knowledge obtained from the instability analyses form the basis for numerical modelling of liquid spray. The most commonly used method for spray calculation today is Discrete Droplet Method (DDM) [53] although in some special cases, such as dense spray regions near the nozzle, Euler–Eulerian multiphase approach is gaining increasing popularity [54]. Taking into account current state of CFD techniques, it would be practically impossible to solve differential equations for the trajectory, momentum, heat and mass transfer of every single spray droplet. DDM simplifies spray modelling by introducing parcels which are groups of identical non-interacting droplets. Thus, one member of the group, i.e. droplet of certain size, represents the behaviour of the complete parcel. That way, only differential equations of parcels are numerically solved which significantly reduces computation time and required computing power [55].

Droplet parcels are introduced in the flow domain with initial conditions of position, size, velocity, temperature and number of particles inside the parcel. Lagrangian description of motion is then used for tracking the parcels through the computational grid. A drawback of the standard DDM is the treatment of Lagrangian parcels as point sources for physical quantities for the Eulerian gas flow field. From the Newton's second law of motion which states that the net force on an object is equal to the rate of change of its linear momentum in an inertial reference frame follows droplet momentum equation:

$$m_d \frac{du_{id}}{dt} = F_{idr} + F_{ig} + F_{ip} + F_{ib} \qquad \textbf{(43)}$$

where m_d and u_{id} are droplet mass and droplet velocity respectively, F_{idr} is the drag force, F_{ig} is a force including the effects of gravity and buoyancy, F_{ip} is the pressure force and F_{ib} summarises other external forces. Comparing the magnitude of all forces, the drag force is only relevant force for fuel spray injection application. Therefore follows:

$$m_d \frac{du_{id}}{dt} = F_{idr} \quad \textbf{(44)}$$

After integrating above equation, u_{id} could be obtained and from this we can solve differential equation for the trajectory:

$$\frac{dx_{id}}{dt} = u_{id} \quad \textbf{(45)}$$

More details about the numerical procedure could be found in [56].

3.2. Evaporation of urea-water droplets

Droplet evaporation can be described by different methods in the rising level of complexity, such as: constant droplet temperature model, infinite diffusion model, effective diffusion model, vortex model and Navier–Stokes solutions [57]. For the purpose of this research Abramzon/Sirignano evaporation model was used to perform calculations [58]. This model represents the extension of classical droplet vaporisation model [55] and includes important effects such as variable physical properties, non-unitary Lewis number in the gas phase and influence of Stefan flow on the heat and mass transfer. It requires a relatively small amount of computational time per droplet and therefore is convenient for spray calculations.

This approach relies on the classic film theory where the resistance to heat and mass transfer are modelled by fictional gas films of constant thickness: δ_T and δ_m. However, in the case of an evaporating droplet these values have to be corrected by the factors F_T and F_M representing the relative change of film thicknesses due to Stefan law. Droplet evaporation is described by the empirical Nusselt and Sherwood numbers derived from experiments using single droplets:

$$\dot{m} = \pi \bar{\rho}_g \bar{\beta}_g D_d Sh^* \ln(1+B_Y) \quad \textbf{(46)}$$

$$\dot{m} = \pi \frac{\bar{k}_g}{\bar{c}_{pF}} D_d Nu^* \ln(1+B_T) \quad \textbf{(47)}$$

where D_d is the droplet diameter, and ρ_g, β_g, $\bar{k}_g$ are the density, binary diffusion coefficient and thermal conductivity of the gas mixture at reference conditions, $\bar{c}_{pF}$ is the specific heat capacity of the vapour, and B_Y and B_T are mass and heat transfer numbers, also called Spalding numbers. The mass transfer number is given as:

$$B_Y = \frac{Y_{VS} - Y_{V\infty}}{1 - Y_{VS}} \quad \textbf{(48)}$$

where Y_V is the vapour mass fraction and index S denotes the conditions at droplet surface, while index ∞ denotes the ambient conditions. Physical properties in (46) and (47) are evaluated at reference temperature and reference vapour concentrations using the 1/3 rule recommended by [53]:

$$\bar{T} = T_S + \frac{1}{3}(T_\infty - T_S) \quad \textbf{(49)}$$

$$\bar{Y}_S = Y_{V,S} + \frac{1}{3}(Y_{V,\infty} - Y_{V,S}) \quad \textbf{(50)}$$

The non-dimensional heat and mass transfer coefficients *Nu** and *Sh** are modified Nusselt and Sherwood numbers, which are given as follows:

$$Nu^* = 2 + \frac{(Nu_0 - 2)}{F_T} \quad \textbf{(51)}$$

$$Sh^* = 2 + \frac{(Sh_0 - 2)}{F_M} \quad \textbf{(52)}$$

where Nu_0 and Sh_0 are Nusselt and Sherwood number of the non-evaporating droplet:

$$Nu_0 = 2 + 0.552 Re^{1/2} Pr^{1/3} \quad \textbf{(53)}$$

$$Sh_0 = 2 + 0.552 Re^{1/2} Sc^{1/3} \quad \textbf{(54)}$$

The diffusional film correction factors F_M and F_T represent the relative change of film thicknesses due to Stefan flow. *F(B)* is the universal function for both factors:

$$F(B) = (1+B)^{0.7} \frac{\ln(1+B)}{B} \quad \textbf{(55)}$$

Finally, the algorithm for calculation of heat and mass transfer is [59]:

1. Evaluate Y_{VS} at the droplet surface.
2. Calculate average physical properties in the gas film using the reference temperature and fuel concentration.
3. Calculate Nusselt and Sherwood number for a non-evaporating droplet, Nu_0 and Sh_0.
4. Get B_Y, F_M, Sh^*.
5. Calculate the mass evaporation rate according to (46).
6. Assume the value of B_T using a value from the previous time step or iteration.

7. Calculate the modified Nusselt number Nu^* and correct the heat transfer number B_T by comparing (46) and (47).

$$B_T = (1+B_Y)^{\phi} - 1 \quad \textbf{(56)}$$

where ϕ is:

$$\phi = \frac{\bar{c}_{pF}}{\bar{c}_{pG}} \frac{Sh^*}{Nu^*} \frac{1}{Le} \quad \textbf{(57)}$$

8. If the difference between assumed and the corrected value of B_T is too large, go back to step 6.

9. Calculate the heat transferred into droplet:

$$Q_s = \dot{m}\left(\frac{\bar{c}_{pF}(T_\infty - T_S)}{B_T} - L(T_S) \right) \quad \textbf{(58)}$$

Despite numerous experimental studies [60] theoretical understanding of evaporation and decomposition of UWS droplets is still far from satisfactory. Theoretical study conducted by Birkhold et al. [16] is implemented in Fire and represents optimum between results accuracy and computational demands. At elevated temperatures the evaporation of liquid starts. Since water has a lower boiling point then urea, the vapour which evaporates first consist mainly of water. Whether is urea vapour also produced is questionable, since urea is known to decompose directly via thermolysis from solid or liquid. This approach assumes two stage process – pure water evaporation until the drop is composed of urea only and subsequent thermolysis. It is assumed that droplets remain spherical throughout the evaporation and decomposition processes, as well as that no crystallization of urea occurs.

The variation of urea concentration of the droplet can be evaluated by:

$$\frac{dY_u}{dt} = -\frac{\dot{m}}{m_d} Y_u \quad \textbf{(59)}$$

Urea melts at 406 K and the thermal decomposition of urea into ammonia and isocyanic acid starts. It is generally accepted that two different ways for the thermal decomposition can be derived:

- evaporation of molten/solid urea to gaseous urea, which decomposes in gas phase into NH_3 and HNCO;
- direct thermolysis from molten/solid urea to gaseous NH_3 and HNCO [16].

This model assumes the latter option and since there is no phase change of urea, an alternative way as used for the evaporation of water must be taken to calculate the urea decomposition rate. For this purpose Arrhenius-type expression is used:

$$\frac{dm_u}{dt} = -\pi D_d A e^{(-E_a/RT_d)} \quad \textbf{(60)}$$

where A is a frequency rate and E_a is activation energy. Experimental data from Yim et al. [61] were used for a default parameter fit.

3.3. Chemical reactions taking place in the gas phase

Coupling all of the above mentioned physical phenomena with the fully detailed chemistry is not advisable from the standpoint of both CPU time and memory. Therefore, CFD modelling with reduced kinetic models is widely adopted. In this study well established seven-step global kinetic mechanism for SNCR chemistry [62] from Brouwer [63] with optimised kinetics parameters [29] was embedded into existing numerical framework. The seven chemical reactions shown in Table 3 are used to predict the concentration of NO, NH_3 and HNCO.

A well-known Arrhenius expression is used to compute reactions in gas phase using parameters given below:

$$r = AT^n e^{-E_a/(RT)} \quad \textbf{(61)}$$

Table 3. Seven step reaction mechanism

Reaction	Pre-exponential factor [cm/(mol s K)]	Exponent [-]	Activation energy [kcal/mol]
$NH_3+NO \rightarrow N_2+H_2O+H$	2.13E+01	5.3	58 039
$NH_3+O_2 \rightarrow NO+H_2O+H$	8.83E+03	7.65	139 964
$HNCO \rightarrow H+NCO$	1.39E+13	0.85	82 457
$NCO+NO \rightarrow N_2O+CO$	2.26E+15	0.0	- 6 214
$NCO+OH \rightarrow NO+CO+H$	3.68E+09	0.0	0.0
$N_2O+OH \rightarrow N_2+O_2+H$	8.6E+04	0.0	20 005
$N_2O \rightarrow N_2+O$	8.5 E+07	0.0	81 023

4. LIQUID WALL FILM MODELLING

Many multi-dimensional numerical models of single-component liquid film have been developed in the past. Models developed by O'Rourke and Amsden [3] and Desoutter [64] adopt a Lagrangian particle tracking method, whereas the models of Stanton and Rutland [65], Bai and Gosman [66], Foucart et al. [67], Wittig [68], Lucchini et al. [69] and Cazzoli and Forte [70] describe the dynamics of the liquid film by an Eulerian approach.

Commercial CFD code AVL Fire, employed during the research conducted in this thesis, is based on the Eulerian approach and this section will present its mathematical structure of, both existing and newly implemented models.

4.1. Governing equations

It is necessary to employ thin film assumption, valid for films with thickness in the range of ≈100 μm, since a 3D two phase flow simulation of liquid wall film is currently too demandable from computational point of view. By integrating across the film thickness, the liquid film can be represented as a two dimensional flow over three dimensional surface, i.e. continuity equation is transformed in the equation for film thickness conservation:

$$\frac{\partial \delta}{\partial t} + \frac{\partial \delta u_1}{\partial x_1} + \frac{\partial \delta u_2}{\partial x_2} = \frac{1}{\rho A}(S_{mD} - S_{mV}) \qquad \textbf{(62)}$$

where δ represents film thickness, u_1 and u_2 are film velocity components, A is surface area of film patch and S_{mD} represents film mass source due to liquid introduction by feeder, spray droplets impingement and condensation, whilst S_{mV} represents sink terms of film mass as a consequence of film rupturing, evaporation and entrainment. We can see that the form of equation (62) allows us to describe liquid film without the need for computational grid adjustment in its vicinity.

Film velocity components could be calculated by imposing assumed velocity profile depending upon film flow regime (either laminar or turbulent), or they can be obtained by solving momentum equation in the form:

$$\frac{dM_i}{dt} = \oint_L \rho \delta u_i (u_i - V_j)\hat{n}_i dL + \oint_L p \delta \hat{n}_i dL + m g_i + \Gamma_i + S_M \qquad \textbf{(63)}$$

where M_i is film momentum, ρ is the film density, u_i is film velocity, V_j is wall velocity, $\hat{n}_i$ is normal to the face cell facing outwards, L is length of the face cell boundary, δ is film thickness, p is film pressure, m is film mass, g_i is gravity vector, Γ_i is the term that takes into account all

shear stresses and S_M presents various source and sink terms, such as film entrainment, spray droplets impingement and film evaporation.

Film pressure p is composed from several contributions as follows [71]:

$$p = p_{refer} + p_{fluid} + p_{hyd} + p_{f,vel} + p_{drop} - p_{\sigma} \quad \textbf{(64)}$$

where p_{refer} is static gas pressure (reference pressure), p_{fluid} is the pressure from liquid film in neighbouring cells, p_{hyd} is hydrostatic pressure defined as:

$$p_{hyd} = \frac{\rho g \delta}{2} \quad \textbf{(65)}$$

, $p_{f,vel}$ is dynamic film pressure that can be written as:

$$p_{f,vel} = \frac{\rho u_f^2}{2} \quad \textbf{(66)}$$

, p_{drop} is pressure resulting from spray droplets impingement and p_{σ} is capillary pressure due to surface curvature:

$$p_{\sigma} = -\sigma C \quad \textbf{(67)}$$

where σ is surface tension of film liquid and C is surface curvature. Momentum equation is solved explicitly by first summing up all the momentum fluxes along boundary faces of selected wall film cell. Thus computed momentum and the already known wall film mass in the cell are used to compute the new velocity value in the actual cell.

In the Fire the default approach for liquid film temperature is to take the same value as the wall underneath. This is valid only for very thin films and to provide a more appropriate treatment the energy balance for the film can be solved. For this purpose a homogeneous mean film temperature in each film cell is calculated using a lumped parameter equation in each film cell. This equation takes into account the following sources [71]:

- conductive heat transfer between film and wall and between film and gas phase flow;
- convective heat transfer within the film;
- enthalpy transfer from spray droplet impingement;
- enthalpy loss from droplet entrainment;
- enthalpy transfer via latent heat during evaporation.

The enthalpy balance equation can be written as:

$$\frac{\partial \rho \delta h}{\partial t} + \frac{\partial h \delta u_1}{\partial x_1} + \frac{\partial h \delta u_2}{\partial x_2} = \frac{1}{A}\left(\dot{H}_{sor,wf} - \dot{H}_{sor,fg} - \dot{m}_{ev} h_{ev} + \dot{H}_{sor,im} + \dot{H}_{sor,ent}\right) \quad \textbf{(68)}$$

where *h* is film specific enthalpy, $\dot{H}_{sor,wf}$ is heat flux from wall side, $\dot{H}_{sor,fg}$ is heat flux from the gas phase boundary layer above the film, $\dot{m}_{ev}$ liquid film evaporation rate, h_{ev} is enthalpy of evaporation, $\dot{H}_{sor,im}$ is energy flux from impacting spray droplets and $\dot{H}_{sor,ent}$ energy flux leaving the film due to film entrainment. The enthalpy transport equation (68) is solved in the semi-implicit way due to numeric stability, using a subcycling procedure with upwinding for the convective fluxes [71].

Finally, species conservation equation could be represented similar to enthalpy transport equation (68):

$$\frac{\partial \rho \delta \gamma_i}{\partial t} + \frac{\partial \gamma_i \delta u_1}{\partial x_1} + \frac{\partial \gamma_i \delta u_2}{\partial x_2} = \frac{1}{A}\left(S_{\gamma i,D} - S_{\gamma i,V}\right) \quad \textbf{(69)}$$

It the expression above γ_i represents concentration of *i*-th liquid component in the film mixture, $S_{\gamma i,D}$ represents source of *i*-th liquid film component due to introduction by feeder, spray droplets impingement and condensation, whilst $S_{\gamma i,V}$ represents sink terms for *i*-th liquid film component as a consequence of evaporation. The species transport equation (69) is also solved in the semi-implicit way due to numeric stability, using a subcycling procedure with upwinding for the convective fluxes [71].

4.2. Phase interaction

Gas and liquid wall film are treated as separated phases within Fire. The coupling is achieved through a modified set of boundary conditions based on semi-empirical relations, which is going to be explained in continuation.

The problem of phase interaction could be reduced to a calculation of gas flow over rough walls because film velocity is typically only few percent of the mean gas velocity above the film. So, the problem of phase coupling comes down to the mathematical description of film roughness effect.

From the logarithmic law of the wall [43]:

$$u^+ = \frac{1}{\kappa}\ln(Ey^+) \quad \textbf{(70)}$$

where κ is von Kármán constant and *E* is defined as follows:

$$E = e^{\kappa C} \quad \textbf{(71)}$$

,the wall film shear is calculated as follows:

$$\tau_w = \rho u^2 \left[\frac{1}{\kappa} \ln\left(\frac{y}{\upsilon} \sqrt{\frac{\tau_w}{\rho}} \right) + C \right]^{-2} \quad \textbf{(72)}$$

Equation (72) has to be solved iteratively which costs most of the CPU time in wall film module. *C* is constant dependent of the level of roughness. Wurz [72] proposed a degree of roughness equal to twice of the mean film thickness. This approach has been shown to be inadequate, so the equivalent sand grain roughness *k* was employed as a parameter for the degree of roughness.

On the basis of the work carried out by Sill [73] and Sattelmayer [74], a correction function dependent on the interfacial shear stress was determined such that:

$$k_s = \psi_\tau(\tau_w) \cdot 2\delta \quad \textbf{(73)}$$

Sattelmayer's measured data of the turbulent boundary layer over liquid films with various properties and thickness was used to propose empirical correlation for roughness factor:

$$\psi_\tau = 0.1\left[\ln(\tau_w + 2) + 0.022\tau_w + 6.57\right] \quad \textbf{(74)}$$

Using the Reynolds number for roughness:

$$\mathrm{Re}_{ks} = \frac{k_s u_\tau}{\nu} \quad \textbf{(75)}$$

three different regions of roughness effect with corresponding constant *C* are distinguished [71]:

1. hydraulically smooth region $Re_{ks} \le 5$:

$$C = 5.2 \quad \textbf{(76)}$$

2. transition region $5 < Re_{ks} \le 70$:

$$C = 5.4494 + (3.0506 - \frac{1}{\kappa}\ln(\mathrm{Re}_{ks})) \cdot \sin\left[0.595 \cdot (\ln(\mathrm{Re}_{ks}) - 1.61)\right] \quad \textbf{(77)}$$

3. completely rough region $Re_{ks} > 70$:

$$C = 8.5 - \frac{1}{\kappa}\ln(\mathrm{Re}_{ks}) \quad \textbf{(78)}$$

The iterative loop starts with initial value of τ_{w0} and sets up first approximation for k_s and Re_{ks}. Then *C* is evaluated and an updated value for τ_w is calculated from equation (72) where the old value for τ_w is used on the right side of equation. The procedure is repeated until τ_w converges sufficiently. Finally, film velocity components are evaluated using converged τ_w value and the film thickness equation is explicitly solved.

4.3. Submodels

This section will provide submodels which, together with conservation equations explained in the previous section, enable description of relevant physical phenomena occurring in spray/wall interaction, wall film formation and wall film development. It should be noted that this part will also present models which present thesis' contribution – multicomponent liquid film evaporation, liquid film rupturing criterion and thermal decomposition of urea deposits.

4.3.1. Film rupturing

Film rupturing model is based on the work of Friedrich et al. [12] as stated in the introductory section. A 2D control volume that embraces liquid film ligament shown in Figure 3 is considered. For this control volume, linear momentum conservation law will be written taking into account inertial forces, surface tension and gravity. As the film approaches the corner, its momentum tends to separate it from the corner, while surface tension and gravity oppose it.

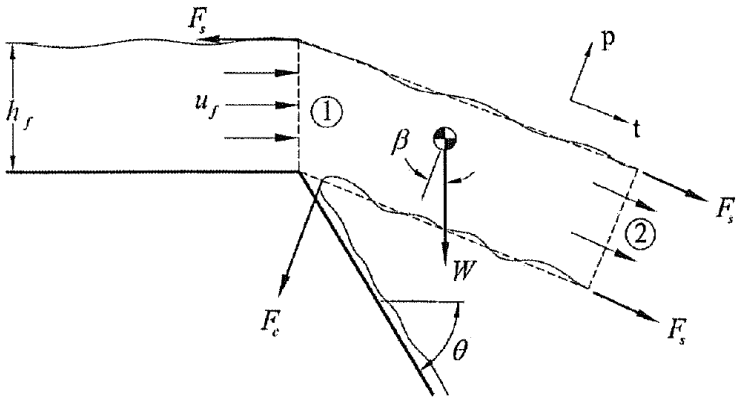


Figure 3. Force balance on film ligament [12]

The momentum flux entering the control volume can be expressed as:

$$-\rho_f \dot{V}_f u_f \sin\theta \qquad \textbf{(79)}$$

where ρ_f is the liquid film density, $\dot{V}_f$ is the film volumetric flow, u_f is the mean film velocity and θ represents inclination of the surface from the horizontal. Surface tension force acts on both sides of the ligament and can be written as:

$$-\sigma w_f \sin\theta \qquad \textbf{(80)}$$

on the upper side and as:

$$-\sigma w_f \tag{81}$$

on the lower side. σ is the surface tension and w_f is the film width. To calculate film ligament length for the evaluation of gravitational forces, experimental correlation of Arai and Hashimoto [75] is used:

$$L_b = 0.0388 h_f^{0.5}\,\mathrm{Re}_f^{0.6}\,We_{rel}^{-0.5} \tag{82}$$

where L_b is the ligament length, h_f is the film thickness and Re_f and We_{rel} are film Reynolds and Weber number defined, respectively, as follows:

$$\mathrm{Re}_f = \frac{\rho_f u_f h_f}{\mu_f} \tag{83}$$

$$We_{rel} = \frac{\rho_g h_f (U_g - u_f)^2}{2\sigma} \tag{84}$$

where ρ_g represents gas phase density, μ_f is the liquid film dynamic viscosity and U_g is the gas phase velocity. Finally, after defining film volumetric flow:

$$\dot{V}_f = u_f w_f h_f \tag{85}$$

linear momentum balance per unit width is given here:

$$\rho_f u_f^2 h_f \sin\theta = \sigma \sin\theta + \sigma + \rho_f g h_f L_b \cos\theta \tag{86}$$

Force ratio, which also represents the separation criterion, is obtained by dividing equation (86) with right-hand side terms:

$$force\ ratio = \frac{\rho_f u_f^2 h_f \sin\theta}{\sigma \sin\theta + \sigma + \rho_f g h_f L_b \cos\theta} \tag{87}$$

This criterion represents a Weber number modified to include effects of gravity and surface tension on the bottom surface of the film. If it exceeds unity, liquid film separation will occur.

4.3.2. Evaporation

This section presents evaporation models that are developed, either on the basis of modified wall functions from O'Rourke and Amsden [3], or using resemblance between momentum and mass transfer.

4.3.2.1. Single component evaporation

First step in evaporation modelling is employing Fick's law of diffusion which takes into account molecular and turbulent diffusion, concentration on the interface and concentration gradient above the film:

$$\dot{m} = -\left[\frac{\rho_v (D_{12} + D_t)}{1 - c_i}\right]\frac{\partial c}{\partial y} \quad \textbf{(88)}$$

where $\dot{m}$ is evaporated mass flux, ρ_v is liquid vapour density, c_i is vapour concentration at the film/gas interface, D_{12} is binary diffusion coefficient of film vapour in gas phase, D_t represents turbulent diffusion coefficient and $\frac{\partial c}{\partial y}$ is concentration gradient above the film.

As mentioned previously, by using resemblance between momentum and mass transfer, the dimensionless Stanton number for mass transfer is introduced:

$$St_m = \frac{\eta c_f}{Sc_t (1 + P_m \sqrt{\eta c_f})} \quad \textbf{(89)}$$

where Sc_t represents turbulent Schmidt number (fixed to 0.9), c_f is local friction factor, P_m is correction factor which takes into account the influence of the laminar sublayer on the mass transfer on rough surfaces and η is correction factor for film waviness.

Local friction factor c_f is implementing the analogy to momentum transfer by directly using logarithmic law of the wall:

$$c_f = \frac{\tau_w}{\rho u_{//}^2} = \left[\frac{1}{\kappa}\ln\left(Ey^+\right)\right]^{-2} \quad \textbf{(90)}$$

In the above expression τ_w is shear stress and $u_{//}$ is film parallel velocity.

The aforementioned correlation η was developed by Burck [76] and extended by Sill [73] for evaporating water films. This correlation was developed originally for heat transfer and it can be written in the following form to describe mass transfer enhancement:

$$\eta = \log\frac{\mathrm{Pr}^{0.33}}{\mathrm{Re}_{ks}^{0.243}} - 0.32 \cdot 10^{-3}\,\mathrm{Re}_{ks}\log(Sc) + 1.225 \quad \textbf{(91)}$$

where *Pr* is non-dimensional Prandtl number:

$$\mathrm{Pr} = \frac{c_p \mu}{\lambda}, \quad \textbf{(92)}$$

and *Sc* is non-dimensional Schmidt number:

$$Sc = \frac{\mu}{\rho D} \quad \textbf{(93)}$$

Finally, P_m was developed by Jayatilleke [77] with the goal to encompass resistance of laminar sub-layer to momentum and heat transfer. Again, this correlation should be modified for mass transfer resistance:

$$P_m = 9.0\left(\frac{Sc}{Sc_t}-1\right)\left(\frac{Sc_t}{Sc}\right)^{0.25} \quad \textbf{(94)}$$

Single component liquid film evaporation rate can be written using the modified Stanton number as:

$$\dot{m} = -\rho_v u_{//} St_m \frac{c-c_I}{1-c_I} \quad \textbf{(95)}$$

where ρ_v represents vapour density and c is concentration of the liquid film component in the gas phase above the film. The heat transfer from the gas boundary layered was not modelled, but rather it was assumed the fixed value of Nusselt number equal to 2. This assumption was proved to be sound for many practical cases by the experimental tests carried out by AVL. Above approach is implemented in the Fire and is used for moderate to high Reynolds number.

As has been previously stated, there is also the other way for mathematical description of liquid film evaporation by employing wall functions. O'Rourke and Amsden were the first proponents of this approach. Liquid vaporization of wall film alters the structure of the turbulent boundary layer above the film due to gas velocity normal to the wall induced by the evaporation [3]. They derived provisional wall functions that inhibit transport of physical quantities above the vaporizing films and that reduce to standard wall functions [43] in case of non-vaporizing walls:

$$H_Y = \begin{cases} \dfrac{\rho C_\mu^{\frac{1}{4}} K^{\frac{1}{2}}}{y_C^+ Sc_L + (Sc_T/\kappa)\ln(y^+/y_C^+)}, & y^+ > y_C^+ \\ \dfrac{\rho C_\mu^{\frac{1}{4}} K^{\frac{1}{2}}}{y_C^+ Sc_L}, & y^+ \le y_C^+ \end{cases} \quad \textbf{(96)}$$

The threshold value of y^+ ($y_C^+ = 11.05$) is used to assess whether laminar or turbulent transport/boundary layer will take its place:

$$y^+ = \rho_L C_\mu^{\frac{1}{4}} K^{\frac{1}{2}} y/\mu_L, \quad \textbf{(97)}$$

y^+ is wall normal distance, C_μ is constant (0.09), K is turbulent kinetic energy and μ_L is laminar viscosity. After wall function calculation evaporation rate is given with the following expression:

$$\dot{m} = H_\gamma \ln\left(\frac{1-c}{1-c_1}\right) \quad \textbf{(98)}$$

Contrary to default evaporation model in Fire, here we can also employ modified wall function for heat transfer, but before, evaporation rate calculated with equation (98) should be transformed into dimensionless vaporization rate:

$$M^* = \frac{\dot{m}}{\rho C_\mu^{\frac{1}{4}} K^{\frac{1}{2}}} \quad \textbf{(99)}$$

Wall function for heat transfer above vaporizing film:

$$\frac{\dot{Q}}{\rho_{gs} c_{pg} c_\mu^{1/4} K^{1/2} (T_{g\infty} - T_s)} = \begin{cases} \dfrac{M^*}{\left(\dfrac{y^+}{y_c^+}\right)^{\frac{M^* \mathrm{Pr}_T}{\kappa}} e^{y_c^+ M^* \mathrm{Pr}_g} - 1} & y^+ > y_c^+ \\ \dfrac{M^*}{e^{y_c^+ M^* \mathrm{Pr}_g} - 1} & y^+ \le y_c^+ \end{cases} \quad \textbf{(100)}$$

In the equation above $\dot{Q}$ is heat flux from/to gas phase, ρ_{gs} is gas phase density, c_{pg} is gas phase heat capacity (specific), $T_{g\infty}$ is gas phase temperature and T_s is film surface temperature. It should be emphasized that all the wall functions are provisional, i.e. they were derived only by physical reasoning and, to the best knowledge of the author, there are no experiments which would unambiguously confirm their accuracy.

4.3.2.2. Multicomponent evaporation

Within this thesis two kinds of multicomponent evaporation models were implemented, similar like in single component case. First, we are going to explain model from Wittig [35] that is basically generalization of single component model described in previous section with additional corrections.

Stanton number for mass transfer is now adjusted for multicomponent case and evaporation rate could be calculated as:

$$\dot{m}_i = -\rho_v u_{//} \frac{St_{m,i}}{\beta_{stefan,i}} \frac{c_i - c_{i,s}}{1 - c_{i,s}} \quad \textbf{(101)}$$

The main difference compared to equation (95) is Stefan flux correction defined as:

$$\beta_{stefan,i} = \frac{\ln\left\{\left[p - p_i(y)\right]/\left(p - p_{i,s}\right)\right\}}{\left[p_i(y) - p_{i,s}\right]/\left(p - p_{i,s}\right)} \quad \textbf{(102)}$$

where p is static pressure of gas phase above the film, p_i(y) is partial pressure of i–th liquid component in the gas phase and $p_{i,s}$ is partial pressure of the i–th liquid component on the

film/gas interface. Also, for the calculation of the friction factor from equation (90), the average shear stress was used instead of the wall shear stress:

$$\tau = \tau_w + \frac{\sum_i \dot{m}_i u_{//}}{1 + \left[\tau_w / (\rho u_{//}^2)\right]^{0.5} / \kappa} + 0.5 \Delta n \frac{dp}{dx} \tag{103}$$

where κ is von Karman constant, $\frac{dp}{dx}$ is streamwise pressure gradient and Δn is normal distance from the wall.

The wall functions derived by the O'Rourke and Amsden [78] were generalized by the Torres et al. [5]:

$$H_{Y,i} = \begin{cases} \dfrac{\rho C_\mu^{\frac{1}{4}} K^{\frac{1}{2}}}{y_C^+ Sc_{L,i} + (Sc_T / \kappa) \ln(y^+ / y_C^+)}, & y^+ > y_C^+ \\ \dfrac{\rho C_\mu^{\frac{1}{4}} K^{\frac{1}{2}}}{y_C^+ Sc_{L,i}}, & y^+ \le y_C^+ \end{cases} \tag{104}$$

with heat transfer wall function identical to equation (100), only with different definition of non-dimensional vaporization rate:

$$M^* = -\frac{\sum_i \dot{m}_i}{\rho C_\mu^{\frac{1}{4}} K^{\frac{1}{2}}} \tag{105}$$

The evaporation rate is calculated using Spalding number together with wall functions and concentration difference:

$$\dot{m}_i = -H_{\gamma,i} \frac{\ln(1+B)}{B} (c_i - c_{i,s}) \tag{106}$$

Spalding number is defined as:

$$B = \frac{\sum_i c_{i,s} - \sum_i c_i}{1 - \sum_i c_{i,s}} \tag{107}$$

As can be deduced by observing presented equations, concentration of vapour phase on the gas/liquid interface plays an important role for the accurate calculation of species vaporization rate. According to insight given from available literature, most of the authors use saturation pressure of each liquid composing the film on the film temperature. Here is very important physical phenomena neglected – how each component influences the rest of the components in the mixture depending on its molecular structure. In order to describe this influence, activity coefficients were calculated using the UNIFAC method [79]. When

considering the molecular interactions, the liquid mixture is assumed as a solution of the structural units of the molecules, rather on the sole molecules. The model relies on a data for the molecular behaviour of the investigated components [80]. UNIFAC method was implemented within this thesis, and on the basis of studied literature, it can be stated that such an approach wasn't employed yet in the area of liquid wall films.

4.3.3. Urea thermal decomposition

Besides the sole decomposition of urea, also additional reactions involving isocyanic acid may occur due to the very high reactivity of the latter [81]. For instance isocyanic acid may add to urea leading to biuret or there can be other reactions yielding higher molecular products such as triuret, melamine, ammeline and ammelide. Some of the possible reaction pathways are given in the Figure 4.

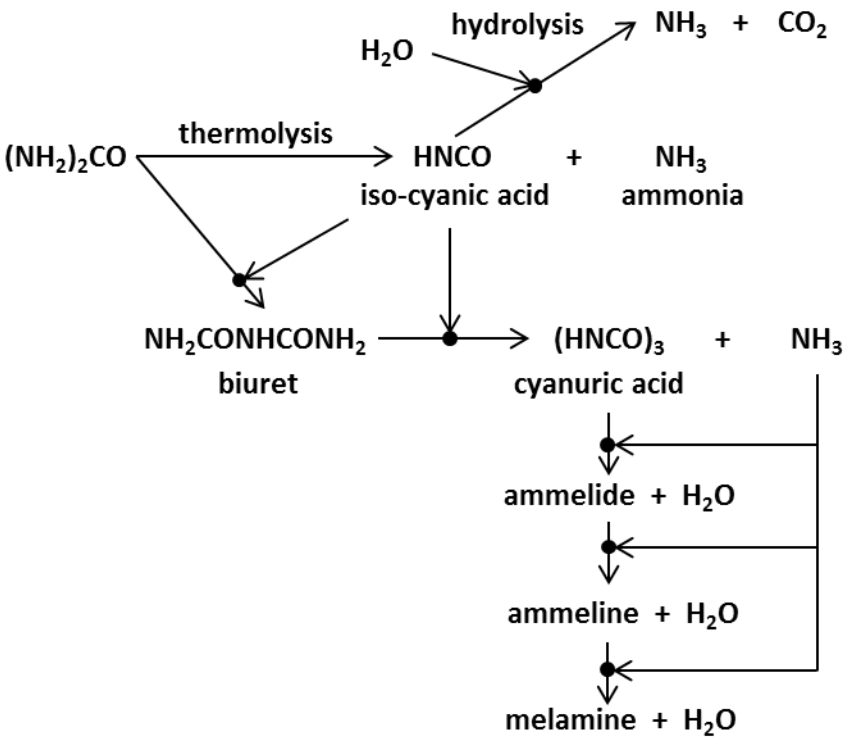


Figure 4. Reaction scheme of urea [82]

Brack et al. [22] have developed the reduced model of urea deposits thermal decomposition based on fifteen reactions describing thermolysis of urea and the creation and degradation of biuret and cyanuric acid. By using the results given in [21], they divided the process of urea thermolysis in three areas in which different deposits have the dominant role.

Each dominant deposit substance was individually experimentally analysed, the dominant reaction pathways were determined and, after optimization of individual stages, all explored mechanisms were fit into the complete process of urea decomposition shown in Table 4. It should be noted here that Brack et al. have solved the problem of influence of deposit geometry [21] by taking into account the area of free surface of the substrate that has great impact on the further course of isocyanic acid evaporation.

Table 4. Kinetic reaction scheme of urea decomposition [22]

reaction	γ_i	A	E_a
I $cya_{(s)} \rightarrow 3HNCO_{(g)}$	0	$1.001 \cdot 10^3 \frac{mol}{s}$	118.42 kJ/mol
II $biuret_{(m)} \rightarrow urea_{(m)} + HNCO_{(l)}$	1	$1.107 \cdot 10^{20} \frac{1}{s}$	208.23 kJ/mol
III $urea_{(m)} + HNCO_{(l)} \rightarrow biuret_{(m)}$	1/1	$3.517 \cdot 10^{11} \frac{ml}{mol\ s}$	75.45 kJ/mol
IV $urea_{(m)} \rightarrow HNCO_{(l)} + NH3_{(g)}$	0.3	$2 \cdot 10^4 \frac{ml^{0.7}}{mol^{0.7}\ s}$	74.00 kJ/mol
V $2biuret_{(m)} \rightarrow ammelide_{(s)} + HNCO_{(l)} + NH_{3(g)} + H_2O_{(g)}$	2	$3.637 \cdot 10^{26} \frac{ml}{mol\ s}$	257.76 kJ/mol
VI $biuret_{(m)} + HNCO_{(l)} \rightarrow cya_{(s)} + NH_{3(g)}$	1/1	$9.397 \cdot 10^{20} \frac{ml}{mol\ s}$	158.68 kJ/mol
VII $biuret_{(m)} + HNCO_{(l)} \rightarrow triuret_{(s)}$	1/1	$1.091 \cdot 10^{15} \frac{ml}{mol\ s}$	116.97 kJ/mol
VIII $triuret_{(s)} \rightarrow cya_{(s)} + NH_{3(g)}$	1	$1.238 \cdot 10^{18} \frac{1}{s}$	194.94 kJ/mol
IX $urea_{(m)} + 2HNCO_{(l)} \rightarrow ammelide_{(s)} + H2O_{(g)}$	1/2	$1.274 \cdot 10^{20} \frac{ml^2}{mol^2 s}$	110.40 kJ/mol
X $biuret_{(m)} \rightarrow biuret_{(matrix)}$	1	$8.193 \cdot 10^{26} \frac{1}{s}$	271.50 kJ/mol
XI $biuret_{(matrix)} \rightarrow biuret_{(m)}$	1	$3.162 \cdot 10^9 \frac{1}{s}$	122.00 kJ/mol
XII $biuret_{(matrix)} \rightarrow 2HNCO_{(g)} + NH_{3(g)}$	1	$5.626 \cdot 10^{24} \frac{1}{s}$	266.38 kJ/mol
XIII a) T > 403 K: $urea_{(s)} \rightarrow urea_{(m)}$	1	$T^{1.5} \cdot 10^{15} \frac{1}{s}$	160.00 kJ/mol
XIII b) T < 403 K: $urea_{(m)} \rightarrow urea_{(s)}$	1	$(806 - T)^{1.5} \cdot 10^{15} \frac{1}{s}$	160.00 kJ/mol
XIV $ammelide_{(s)} \rightarrow ammelide_{(g)}$	1	$10^{14} \frac{1}{s}$	201.67 kJ/mol
XV $HNCO_{(l)} \rightarrow HNCO_{(g)}$		Herz – Knudsen equation	

Reaction of HNCO evaporation is described by employing the Herz-Knudsen equation, contrary to the rest of the reactions which are described with Arrhenius expression:

$$r = Ae^{-E_a/(RT)} \quad \textbf{(108)}$$

Vapour pressure of HNCO could be approximated with the following expression [83]:

$$p_{v,HNCO} = 10^{4.69-\frac{1252.195}{T-29.167}} \cdot 10^5 \quad \textbf{(109)}$$

which is used afterwards in order to calculate ratio of liquid HNCO density versus vapour HNCO density:

$$h = \frac{\rho_{HNCO}}{p_{v,HNCO} \cdot \frac{M_{HNCO}}{RT}} \quad \textbf{(110)}$$

Finally, after defining average molecular velocity by employing kinetical theory of gases:

$$\bar{v} = \sqrt{\frac{8RT}{\pi \cdot M_{HNCO}}} \quad \textbf{(111)}$$

it is possible to express source term for the evaporation rate of the liquid HNCO:

$$j_{HNCO} = \frac{1}{4}\alpha_C \cdot \bar{v} \cdot \frac{c_{HNCO(l)} \cdot 10^6}{h} \cdot A_R \quad \textbf{(112)}$$

Above mentioned reactions were implemented for the first time as a part on the wall film model as a step in the process of description of urea deposits influence on overall domain of the real flue gas aftertreatment system.

4.3.4. Spray/wall interaction

According to dimensionless analysis carried out by Kuhnke [84], there are four different regimes of spray-wall interaction depending on the dimensionless wall temperature and the dimensionless droplet velocity, as presented in Figure 5. Dimensionless temperature is defined as follows:

$$T^* = \frac{T_w}{T_s} \quad \textbf{(113)}$$

where T_W is the wall temperature and T_S is the droplet saturation temperature.

Dimensionless droplet velocity is defined as:

$$K = \frac{(\rho_d D_d)^{3/4} u_{d,\perp}^{5/4}}{\sigma_d^{1/2} \mu_d^{1/4}} \quad \textbf{(114)}$$

where ρ_d is the droplet density, $u_{d,\perp}$ is the wall normal component of the droplet velocity, σ_d is the surface tension on the droplet-gas interface, D_d is the droplet diameter and μ_d is the dynamic viscosity of the droplet.

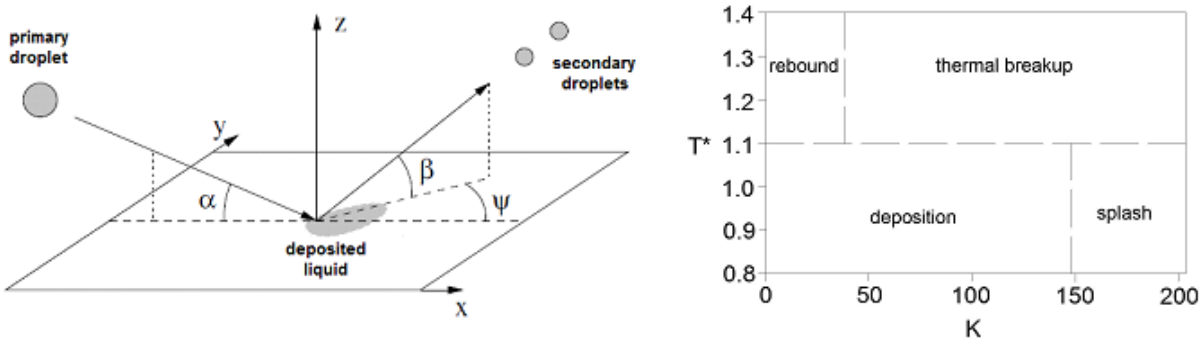


Figure 5. Schematic representation of droplet wall interaction and interaction regimes [84]

Deposition:

- occurs at low droplet velocities and if T* < 1.1;
- impacting droplets are completely deposed on the wall and create wall film.

Splash:

- occurs at higher droplet velocities and if T* < 1.1;
- particles are atomized and smaller secondary droplets are formed after the impact;
- a fraction of the droplet mass is transferred to the wall film.

Rebound:

- occurs at low impact velocities and if T* > 1.1;
- vapour layer between droplet and wall is formed that prevents a direct contact of the droplet with the wall and leads to a reflection of impinging droplet (the Leidenfrost effect);
- there is no wall film formed.

Thermal breakup:

- occurs at higher impact velocities and if T* > 1.1;
- the droplet disintegrates into secondary drops;
- there is no wall film formed.[85]

5. NUMERICAL SIMULATIONS, RESULTS AND DISCUSSION

This section presents results of mathematical models developed and implemented within the scope of thesis. Each section is also accompanied with short description of experimental configuration, data from which were used for model validation, numerical settings for simulations and discussion how the result fit the research hypothesis. According to introductory section, four different areas were tackled, namely: film rupturing criterion from Friedrich [12], multicomponent liquid film evaporation models on the basis of O'Rourke and Amsden [3] and Wittig [35], reaction kinetics of urea deposits thermal decomposition from Brack et al. [22] and numerical framework for selective non-catalytic reduction using 7-step reaction kinetics mechanism of Brouwer [63].

5.1. Film rupturing

Since there is no model in the literature that describes properties of ruptured film, verification of film rupturing criterion was carried on just on the qualitative basis in this stage of research. Thus, the separation criterion in the form of force ratio described in mathematical model section was adapted and implemented into the commercial CFD code Fire.

5.1.1. Experimental configuration

The data for numerical simulation were taken from experimental setting presented in [12]. The dimensions of the test section at the point of film introduction and up to the corner are 2 cm tall and 10 cm wide, giving an aspect ratio of 5. The liquid is introduced through a feeder on the bottom wall in the film introduction section. Flow is expected to be two-dimensional with this aspect ratio i.e., limited wall effects for the centre 7.5 cm of the test section [12]. It is over this width of the test section that the film is introduced. The liquid used for investigations was water with the addition of a surfactant Surfynol 465 at 0.1 % and 1.0 % by mass in order to capture influence of different surface tension effect. It should be noted that the surfactant had minimal effect on the fluid viscosity. The corner section has a 60° angle, measured from the horizontal and the length of the duct from the feeder to the corner is 230 mm. After the corner, the duct has an aspect ratio of 1.429. Gas phase velocities ranged from 20 m/s to 45 m/s and liquid flow rates varied from 6.5 cm^3/s to 41.5 cm^3/s.

A Photron 1280 PCI high speed camera, with close-up lenses totalling +7 diopter, was used to characterize the general characteristics of the liquid film. Measurement of the degree

of liquid film separation was made by pulling off the liquid that stays attached to the downward sloping wall after the corner. The captured film volume was weighed to establish a mass flow of liquid attached to the wall, which, along with the measured liquid flow into the test section, provides the mass flow of liquid separated at the corner [12].

5.1.2. Numerical simulation

In order to verify film separation criterion simulation of liquid film sheared by air flow was conducted on geometry with dimensions given in Figure 6. A three-dimensional computational mesh with 420,000 orthogonal hexahedron cells and corner section with slope of 60° measured from the horizontal was used for the simulation.

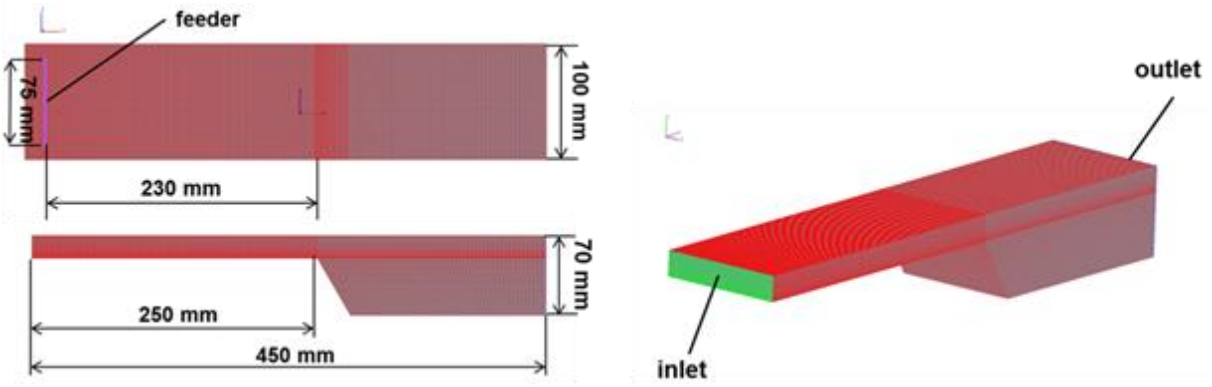


Figure 6. Computational domain with boundary conditions for case of film rupturing

To properly describe evolution of liquid film sheared by air flow, mesh was refined until the corner section with cell size below 1.5 mm. Air enters the domain with 20 m/s through the inlet with dimensions of 100 × 20 mm^2. Turbulence quantities on the inlet were 0.001 m^2/s^2 for turbulent kinetic energy and 0.0033 m for turbulent length scale. Outlet was defined as constant pressure outlet of 1 bar. The wall boundary condition was imposed at the bottom, top and on the domain sides. Pressure velocity coupling of momentum and continuity equation was obtained using the SIMPLE/PISO algorithm. The central difference discretisation scheme was used for the convective term in the continuity equation with a blending factor of 1, and for the convective terms in momentum equations the same scheme with a blending factor of 0.5 was used. Turbulence was modelled using advanced k-zeta-f model [46]. Liquid film of water was introduced using feeder located 20 mm from the inlet with volumetric flow rate of 41.5 cm^3/s. Time discretisation step was reduced to 1e-04 s to achieve stabile calculation.

5.1.3. Results

Verification of film rupturing criterion was carried just on the qualitative basis in this stage of research. Separation criterion in the form of force ratio described in the mathematical model section was adapted to numerical environment of CFD code Fire. Since there is no model in the literature that describes properties of ruptured film, i.e., percentage of ruptured mass and particle size distribution of separated droplets, authors made some assumptions that they presume as fairly reasonable:

- when force ratio is above unity, the whole film mass will detach, otherwise film will continue with propagation along the wall;
- diameter of separated droplets is assumed to be equal to the half of film thickness according to O'Rourke and Amsden [78].

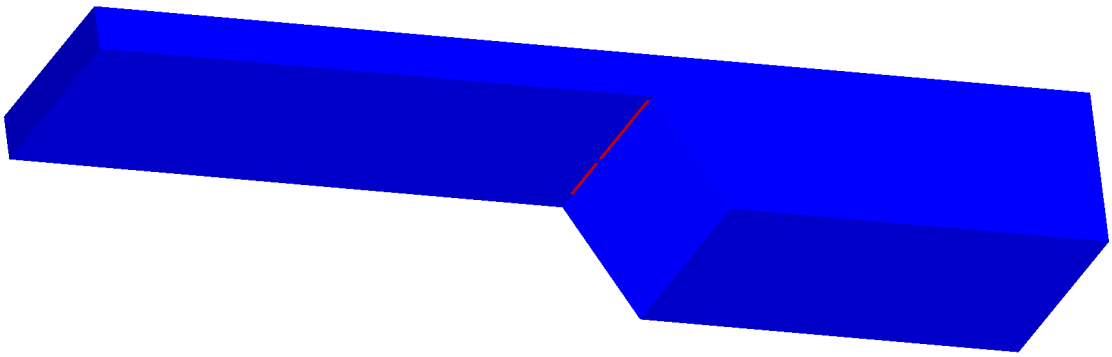


Figure 7. Qualitative representation of film separation criterion

Qualitative depiction of film separation is presented in Figure 7 and Figure 8. Cells where separation occurs are marked red inside the software, and it can be seen that they are located at the edge of the slope as expected. On that position, film properties were calculated and inserted into the separation criterion to check whether the code produces correct values. Thus, verification of the implemented model was obtained through qualitative check of cell position where separation occurred and through manual calculation of separation criterion for activated cells. This is a reasonable approach since only separation criterion is implemented in the code and it is the result of semi-empirical considerations. On the Figure 8 it can be seen that spray droplets formed by the liquid mass from film rupturing have diameter equal to half of the film thickness which is one of the model assumptions. It would be rather unphysical to

expect droplets whose diameter is greater than the film thickness since there is no mechanism which would cause such formation. There are no further physical implications following from the criterion, which could be observed in the simulations.

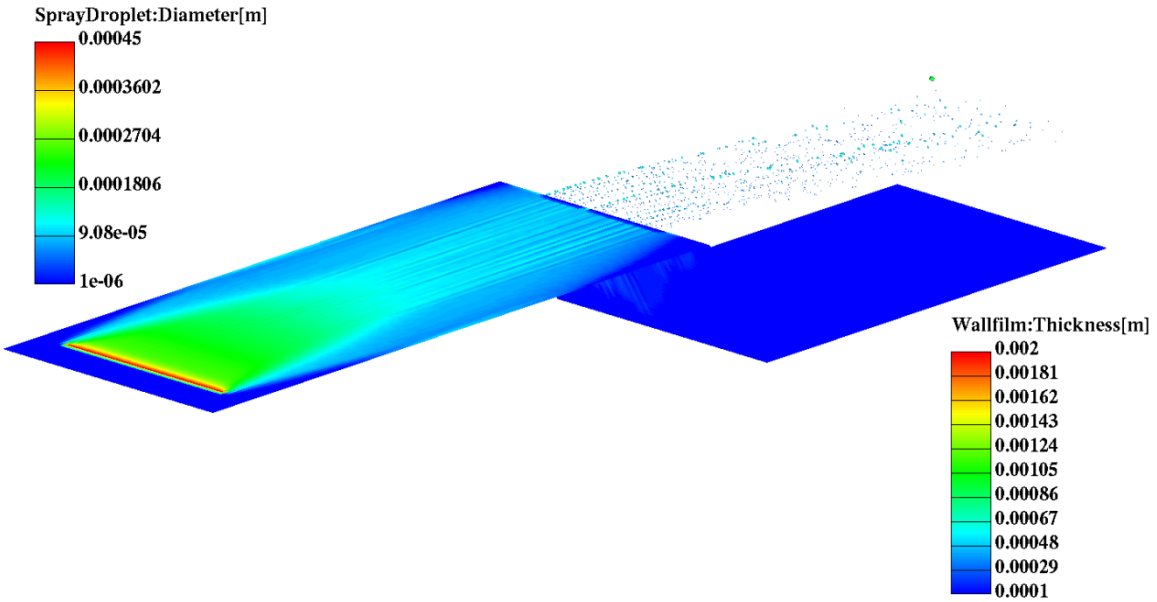


Figure 8. Film rupturing at the sharp corner

5.2. Multicomponent evaporation

5.2.1. Experimental configuration

The test section presented on Figure 9 has a primary cross section of 83x60 mm and has been characterized with the turbulent intensity and an integral length scale of 5 % [86]. The channel is divided with the film plate on two equal parts, each having height of 3.9 mm. The liquid film is introduced by feeder composed of a row of 0.5 mm holes, which are 0.8 mm apart. The test section provides six measurement planes, 80 mm apart. The first plane is 20 mm downstream from the start of the film plate and marks the starting point of the computational domain.

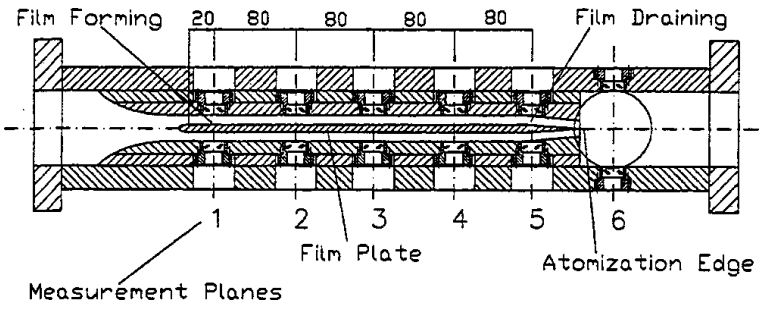


Figure 9. Shematic representation of the test section [35]

The vapour concentration profiles are measured by taking gas samples through a probe and cooling them down in a condenser to 273 K. The vapour concentration in the gas phase of the condenser is calculated based on the condensate compound and the measured pressure and temperature in the condenser. The ratio of the mass flow rate of each component and the dry air represents the mass concentration of the vapour component at the probe tip [35].

5.2.2. Numerical simulation

In order to reduce computational demands to acceptable level, only part of the domain was simulated. This was possible since flow within the channel has intrinsically symmetrical behaviour. Thus, only 5 mm of the channel width (compared to 60 mm in experiment) was simulated. The Figure 10 shows computational domain 300x5x3.9 mm with boundary conditions details. It consists of 15 000 control volumes.

Two cases were simulated with the goal of investigating the influence of gas phase pressure above the liquid film.

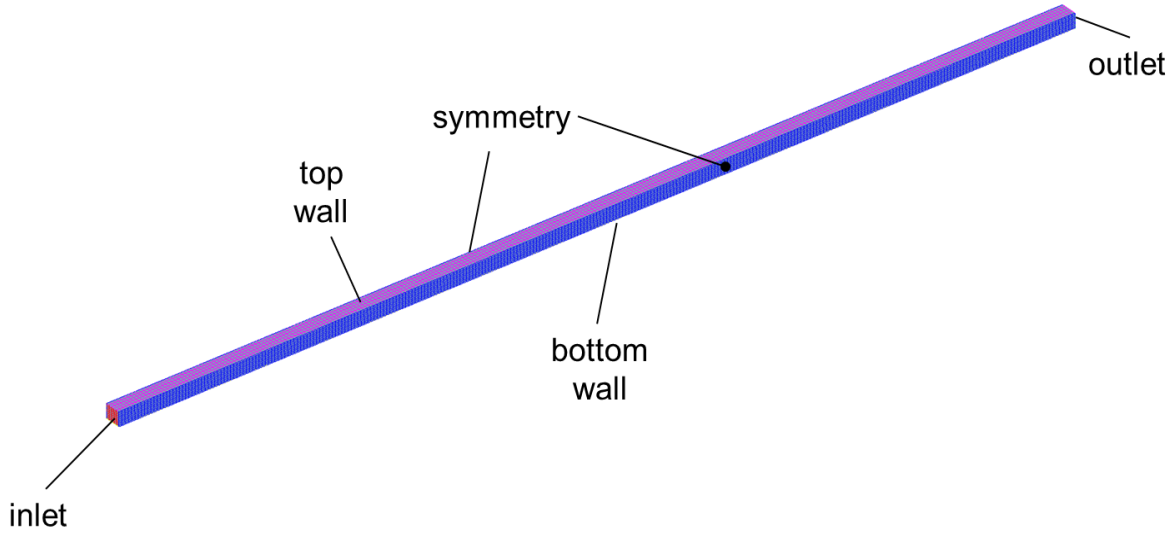


Figure 10. Mesh representation of computational domain

Time step was 5e-04 s for all simulated cases in order to have stable calculations with criterion of Courant number <1. The adiabatic boundary condition was imposed on the top and bottom walls, whilst the symmetry was set on the domain sides. Pressure on the outlet was either 1.1 or 2.6 bar, depending on the simulation case. For the turbulence, scalar and energy transport equations a first order UPWIND differencing scheme was applied, whilst for the continuity equation the central differencing scheme (CDS) was employed. The CDS can generate numerical oscillations yielding unbounded and non-monotonic solutions. Therefore, for the momentum equation a combination of MINMOD relaxed and UPWIND was proposed by introducing the blending factor of 0.5 [87]. The solution convergence criterion is achieved when the momentum, pressure and energy residuals decrease 4 orders of magnitude compared to the first iteration. The pressure velocity coupling of the momentum and continuity equation was obtained using the SIMPLE/PISO algorithm. Liquid, with equal mass fractions of ethanol and water, was introduced into the computational domain by means of feeder cell with mass flow rate of 1.5e-04 kg/s. Finally, turbulence quantities on the inlet were 5 % for turbulent intensity and turbulent length scale and turbulence was modelled using k-ε model.

5.2.3. Results

Following figures show comparison of developed multicomponent models with experimental data. We can see that model on the basis of O'Rourke and Amsden gives the same order of magnitude of concentrations compared to experiment. However, the sole agreement with data is not satisfactory. Reason behind this behaviour lays in the fact that wall

functions for boundary layer above vaporizing films were derived without experimental back-up. It seems that physical reasoning behind them is at least qualitatively correct, but the model is not able to pick up experimental tests quantitatively.

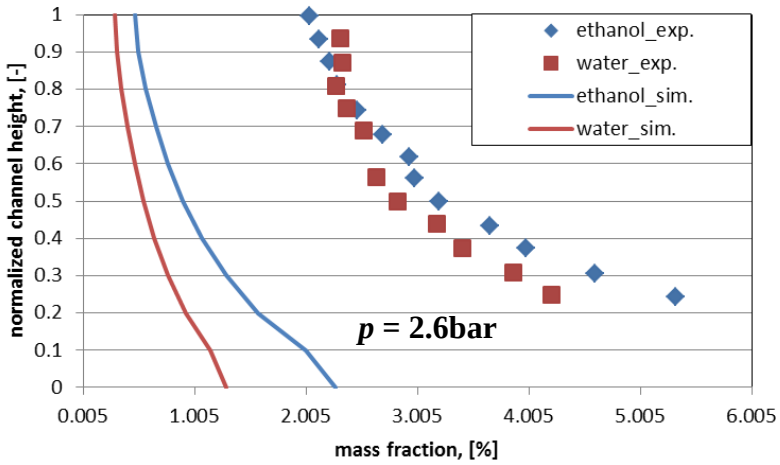


Figure 11. Comparison of gas phase concentrations in measurement plane 4 (O'Rourke model)

In the Figure 12 results of Wittig model show much better agreement with experiments. Here it should be noted that heat transfer in boundary layer was calculated with fixed Nusselt number, which was shown previously as a sound assumption in single component model. The validity of this model in single component case was generalized to multicomponent and also employment of UNIFAC method has certain share in improved results. As a conclusion of this part, it can be said that Wittig's model should be employed due to better results. However, very limited experimental data on this topic make it difficult to give definite conclusions. It should be noted that Figure 11 and Figure 12 represent high pressure conditions of 2.6 bar. There were also measurements carried out in the lower pressure of 1.1 bar in order to see what is the influence of pressure and whether newly developed model is able to capture those differences.

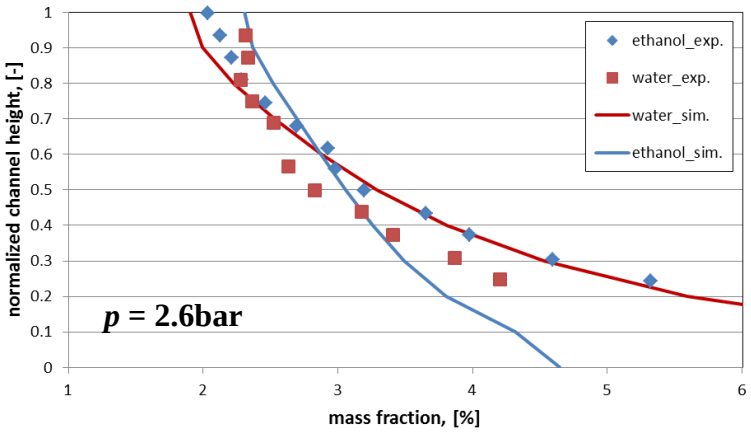


Figure 12. Comparison of gas phase concentrations in measurement plane 4 (Wittig model)

Comparison between Figure 12 and Figure 13 shows that lower pressure represents smaller resistance to evaporation, and consequently the concentrations in the gas phase of measurement plane 4 are higher. Since model based on the wall functions from O'Rourke and Amsden proved to be only qualitatively correct, comparison with experimental data on lower pressures was carried out only with Wittig model. It can be seen on Figure 13 that this model is able to capture experimental trend, especially in the case of ethanol concentrations. Agreement in the case of water concentrations is not so good, but still satisfactory, especially in the case of channel heights closer to the film surface. Moving away from the film surface, model under predicts water concentrations.

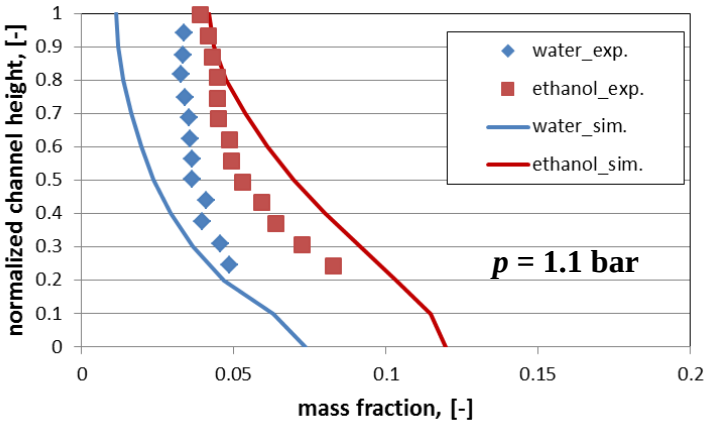


Figure 13. Comparison of gas phase concentrations in measurement plane 4 (Wittig model)

5.3. Urea thermal decomposition

5.3.1. Experimental configuration

For the validation of deposit decomposition model experimental work carried out in [22] was used. In that work the thermogravimetric analyses (TGA) were performed on a TG/DTA6300R from Seiko Instruments Inc, under nitrogen atmosphere (250mlN/min), with a cylinder shaped alumina crucible (crucible area of 14.52mm^2). The gaseous products were analysed by using a Fourier transform infrared spectrometer (FTIR) of Bruker (Bruker FTIR TENSOR) coupled with a thermogravimetric analyser of Netzsch (Netzsch TG 209F1IRIS). The measurements were done under nitrogen atmosphere (70mlN/min) with a cylinder-like alumina crucible (crucible area of 50.27mm^2). At characteristic temperatures corresponding to minima of the differential thermal gravimetric (DTG) curve, the sample was quenched at room temperature and afterwards, the remaining sample mass was qualitatively and quantitatively analysed by using high-performance liquid chromatography (HPLC) [22].

The case of plate cooling from PhD thesis of Felix Birkhold [87] is used as a basis for physical consideration of urea decomposition model, since there are no measurements in real exhaust gas aftertreatment configurations. Details of settings are given in [87], while only brief description is given here. Thin metal plate (2 mm) was placed inside the middle of rectangular channel with dimensions of 94x120x400 mm, as can be seen in the Figure 14. Uniform air flow passes both above and below the plate with velocity of 30 m/s. Urea – water spray is injected into the air stream above the plate and, depending on the local conditions there will or won't be wall film formation on the plate. Thermocouples are used to measure change in the plate temperature.

5.3.2. Numerical simulation

Since there are only 0D experimental data for validation of the urea deposits reaction kinetics, similar approach was used for CFD calculations. Thus, only one computational cell was simulated with area equal to that of experimental crucible (14.52 mm^2). Gas phase solution hasn't been taken into account and therefore, under relaxation factors were kept low in order to stop convergence of the gas phase. Within this work only wall film phenomena were investigated together with the overall mass balance. The other reason for keeping only few iterations of the gas phase is pronounced length of experimental investigations in the range of tens of minutes, which is by no means suitable time scale for CFD simulations.

Figure 14 depicts computational mesh consisting of 127 680 control volumes with imposed boundary conditions used for the simulation of the Birkhold experimental case described in the previous section. Temperature of the incoming air is 292 °C, whilst turbulent kinetic energy of 10 m^2/s^2 and turbulent length scale of 0.01 m were considered as reasonable assumption for given geometry and flow conditions. For calculation of turbulent flow field, advanced k-zeta-f model was employed. On the outlet static pressure boundary condition was imposed with 100 000 Pa, and side walls were given temperature equal to the inlet air. Pressure velocity coupling was accomplished by using combination of Simple and PISO algorithms. The only relevant body force was gravity acting perpendicular to min flow direction. For the turbulence energy and scalar equation upwind differencing scheme was utilized, for continuity equation central differencing scheme was used and, for the reasons of bounded results and minimizing numerical diffusion, blended differencing scheme between upwind and CDS was employed with the blending factor 0.5. Regarding spray settings, initial droplet velocity on the nozzle exit was 18.2 m/s, turbulent dispersion was taken into account with suitable built-in model and drag force on droplets was calculated using Schiller-Neumann correlation [88]. Average Weber number was below threshold for secondary atomization process, so consequently no break-up mechanism was activated. Finally, time step solution was considered converged when momentum and energy equation residuals fall 3 and 6 orders of magnitude respectively.

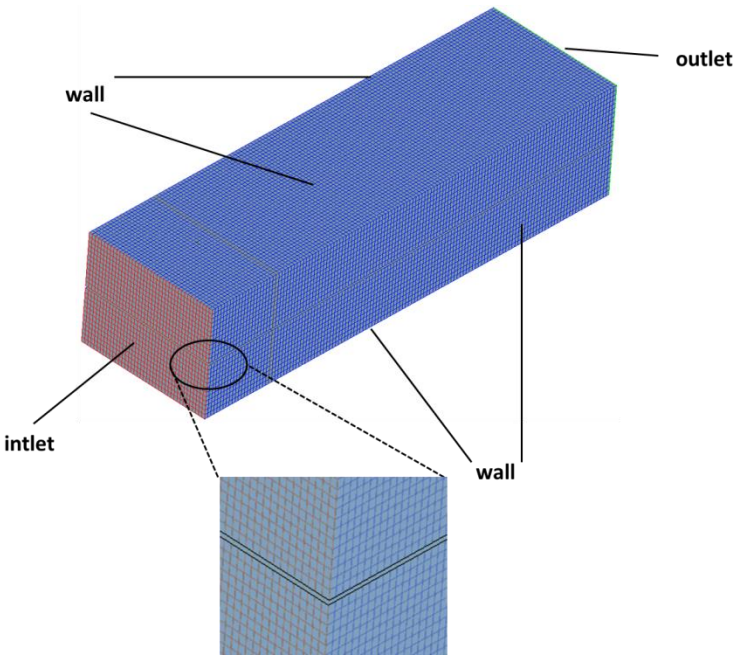


Figure 14. Computational domain with plate detail

5.3.3. Results

Figure 15 represents result of biuret decomposition. Initial mass was 50 mg with the heating rate of 2 K/min. High-performance liquid chromatography and thermogravimetric measurements were used to quantitatively describe reaction pathway of biuret. It can be seen that biuret mass loss has very good agreement compared with experiment, whilst cya and total mass show a little discrepancy in later stage of decomposition. However, overall behaviour is satisfactory and points to the conclusion that model could be used with satisfactory accuracy in real cases.

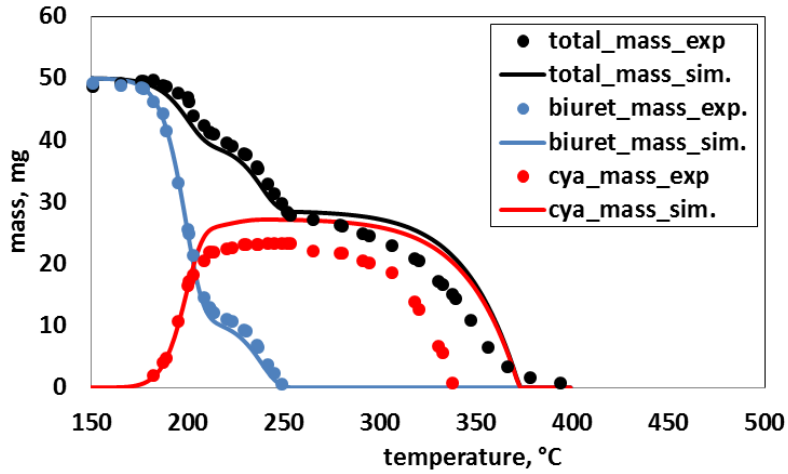


Figure 15. Biuret decomposition – comparison with experimental results

Since available literature review didn't reveal any experimental data in real exhaust conditions, verification of results was conducted on the well-established case from Birkhold [89]. In his work, Birkhold hasn't considered formation of deposits which is likely to happen in real exhaust system. Figure 16 shows developed wall film pattern due to spray/wall interaction and local cooling of the plate. When local energy provided by the plate cannot sustain evaporation of incoming spray droplets any more, liquid film will arise and build up. It can be seen that average thickness in the impact zone is in the range of 15-20 μm. The region of the plate with the highest frequency of impacting spray droplets has a temperature of around 340 K, compared to UWS temperature of 293 K. At the edges of the wall film pattern, there is narrow area with temperature of around 500 K which is boundary with the uniform temperature of the rest of the plate. It is expected that here will be the area of urea deposit formation since the energy inflow from the environment is the highest due to steep temperature gradient. If we recall reactions of urea deposit formation from Table 4, it is clear

that all of them are endothermal in nature, meaning the higher energy intake is, the higher are reaction rates.

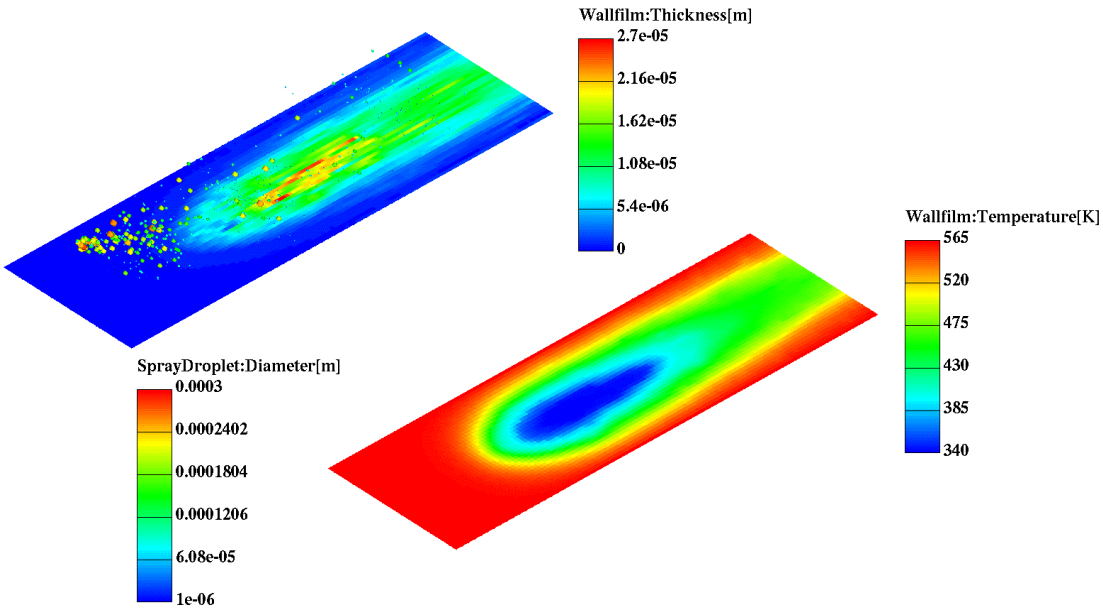


Figure 16. Spray/wall interaction and temperature field on the experimental plate

Figure 17 depicts deposit formation during the spraying of urea-water solution on the hot plate and confirms previously stated reasoning about the deposit formation zone. On the temperatures on the film boundary biuret and cyanuric acid concentrations are the same order of magnitude with only minor traces of higher product triuret.

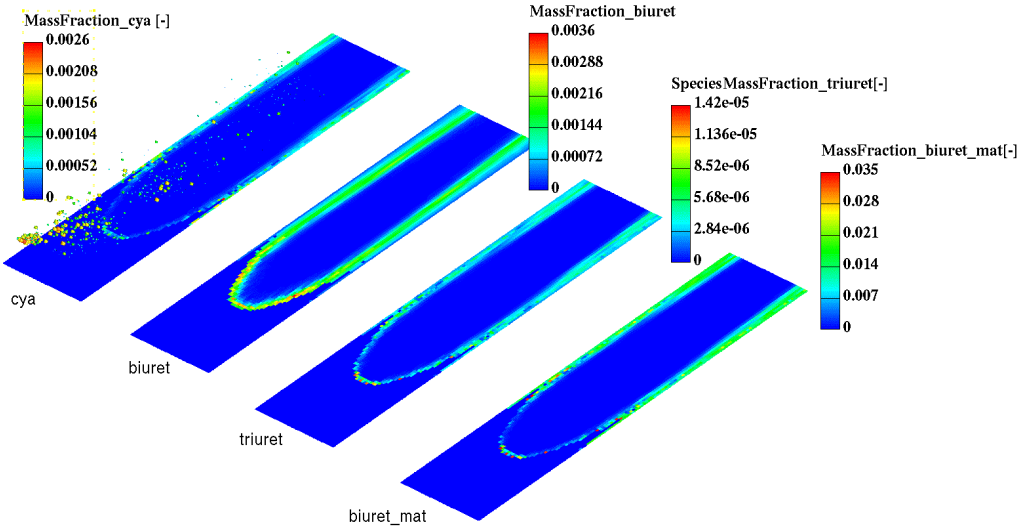


Figure 17. Development of urea deposits on the Birkhold experimental case

5.4. SNCR cases

Implemented mechanism was validated on the real industrial reactor for which experimental results can be found in the literature as well as on the case of municipal waste incinerator. Simulated results show satisfactory agreement of simulation results with measured data and are discussed below.

5.4.1. Pipe reactor

Influence of the temperature on the SNCR process efficiency was performed through the simulation of three experimental cases with various inlet temperatures, ranging from 1325 to 1365 K.

5.4.1.1. Experimental configuration

The NO reduction experiments by injecting the urea-water solution were carried out in a pilot-scale flow reactor depicted in Figure 18. The reaction temperature is controlled by a gas-fired burner installed at the reactor inlet which has a heating rate of 50-150 kW. The pipe reactor is divided into three zones according to temperatures and nozzle position. Pipe begins with high temperature zone which is 1.5 m long. After that, follows the nozzle region zone where the urea-water solution is injected and where intensive water evaporation from spray droplets takes place. This region is relatively narrow, compared to the other two zones. The low temperature zone follows the nozzle region and finally ends the pipe reactor.

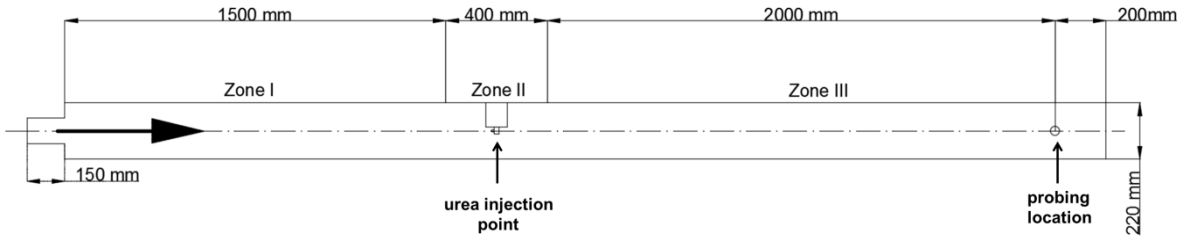


Figure 18. Schematic representation of experimental pipe reactor [29]

The burner and the reactor walls are insulated with 0.15 m thick ceramic wool in order to maintain a constant temperature gradient through prevention of heat losses to the environment. The mean temperature gradient in the vicinity of nozzle (zone II) is about 55-75. The outlet gases from the reactor are cooled in a heat exchanger before being exhausted to the atmosphere. Uniform mixing of fuel gases with the reagent (urea-water solution) plays an

important role in improving NOx reduction, and the injection nozzle is a key component. Urea-water solution is injected through a water-cooled atomizing nozzle of an injection angle of 70° and 6 holes with inner diameter of 1.016 mm. This nozzle releases the mean droplet size of 36 μm at the injection pressure of 3 atm. The weight concentration of the urea solution of 5 % was experimentally confirmed as an optimum value to maximize NOx reduction. NSR is varied from 1.0 to 2.0. NOx is measured from the sampling probe located at 2.8 m behind the nozzle injection point. The concentration of NOx is measured using the NO/CO analyser. NH_3 is also measured by the NH_3 electrode [29].

5.4.1.2. Numerical simulation

Figure 19 depicts the domain used in this research together with the boundary surfaces. In order to achieve mesh independency several computational meshes were examined. For the mesh dependency test, three meshes were generated consisting of 500 000, 200 000 and 107 000 control volumes, the last one being symmetrical. It has been observed that mean flow quantities inside the domain don't change significantly with decreasing mesh resolution to ≈200 000 control volumes. The same could be stated when employing symmetrical domain consisting of approximately 107 000 control volumes. Taking into account above stated, a symmetrical domain was selected for further research in order to maximise utilisation of available computational resources. At the outlet of the domain, the pressure boundary condition was applied. The nozzle surface was defined with the constant temperature (1073 K) wall boundary condition.

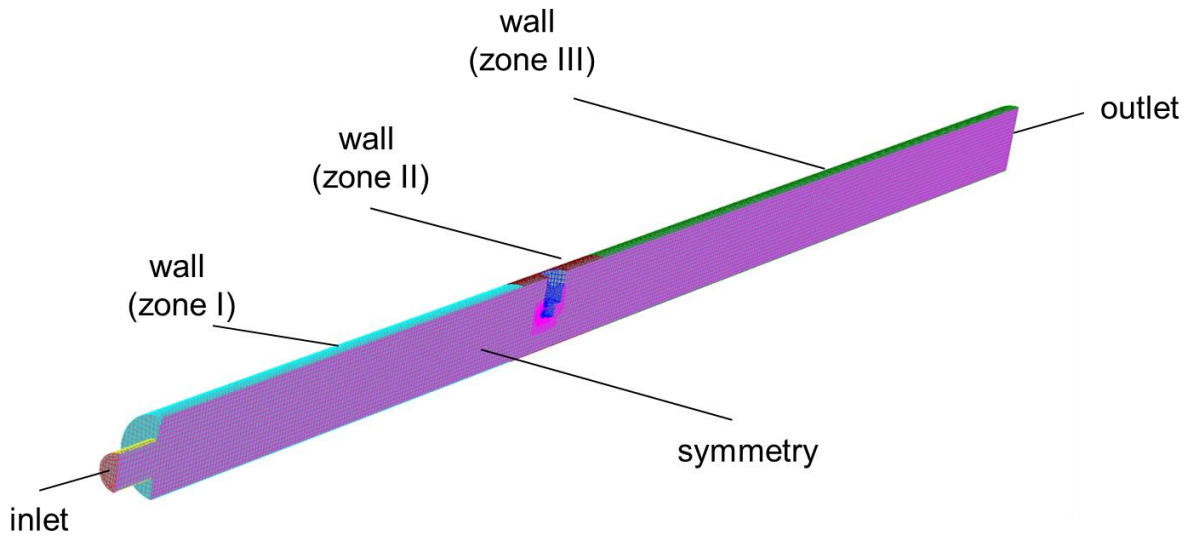


Figure 19. Computational domain with symmetric boundary condition

For the turbulence, momentum and energy transport equations a first order UPWIND differencing scheme was applied, whilst for the continuity equation the central differencing scheme (CDS) was employed. The CDS can generate numerical oscillations yielding unbounded and non-monotonic solutions. Therefore, for the momentum equation a combination of CDS and UPWIND was proposed by introducing the blending factor of 0.5 [90]. For all calculations the implicit time integration was employed ensuring unconditional solution stability, whilst the accuracy was achieved by employing sufficiently small time step of 1e-04 s. The solution convergence criterion is achieved when the momentum, pressure, energy and volume fraction residuals decrease under the value of 1e-04. The pressure velocity coupling of the momentum and continuity equation was obtained using the SIMPLE algorithm. Air entered the domain with prescribed constant mass flow through the inlet with diameter of 100 mm. Finally, turbulence quantities on the inlet were 10 % for turbulent intensity [29] and turbulent length scale was assumed to be 0.007 m. Urea water solution was injected into domain with particle size distribution approximated by Rosin–Rammler distribution with mean droplet diameter of 36 μm and spreading parameter value of 3 [29]. Other details can be found in experimental investigations performed in [29]. Influence of the temperature on the SNCR process efficiency was performed through the simulation of three experimental cases with various inlet temperature, as shown in Table 4.

5.4.1.3. Results

This section presents results of on the previously described real industrial case of pipe reactor. Figure 20 depicts the injection of urea water solution in the experimental pipe. Furthermore, here the droplet diameter and velocities are given. Blue particles represent slower droplets, and red particles represent faster particles, respectively. The droplets lose their mass due to the evaporation of water and urea thermolysis. Six injection spray cones can also be observed.

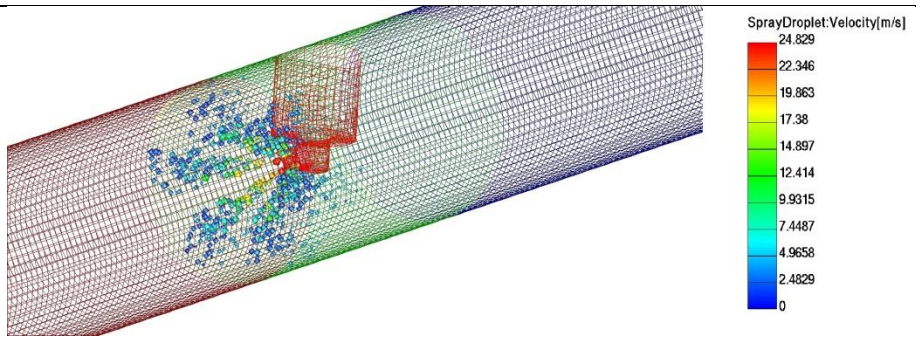


Figure 20. Detail of spray injection

In Figure 21 the velocity field inside the calculated experimental pipe is given for all simulated cases. As can be expected, velocity field of all cases is identical, since only inlet temperature was varied. On the left hand side of the figure, where the inlet is positioned, velocity is the highest. As the flow gets closer to the injector, it slows down, and afterwards has a stable profile with the velocity of around 5 m/s giving residence time for a reagent of about 0.3 s.

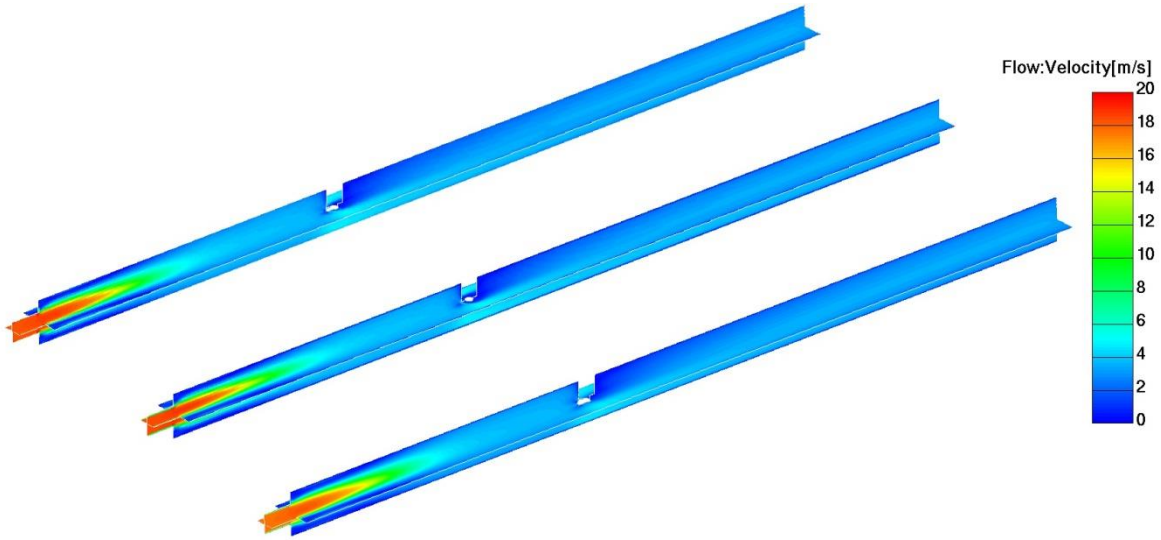


Figure 21. Velocity field

In Figure 22 the temperature field inside the calculated experimental pipe is given. Also, on the left hand side of the figure, where the inlet is positioned, the highest temperature can be observed. In the first part of the experimental pipe, the flow cools down only due to heat transfer to cooler walls. Linear temperature drop along pipe length has been assumed which correlates well with experimental measurements [29]. As the flow gets closer to the injector, the temperature decreases significantly due to the water evaporation and thermolysis

of urea, and afterwards has a stable value between 1100 and 1200 K, depending on the simulated case. Temperature is vital factor affecting deNOx efficiency and in the following, the influence of temperature field on the concentration of different species is shown.

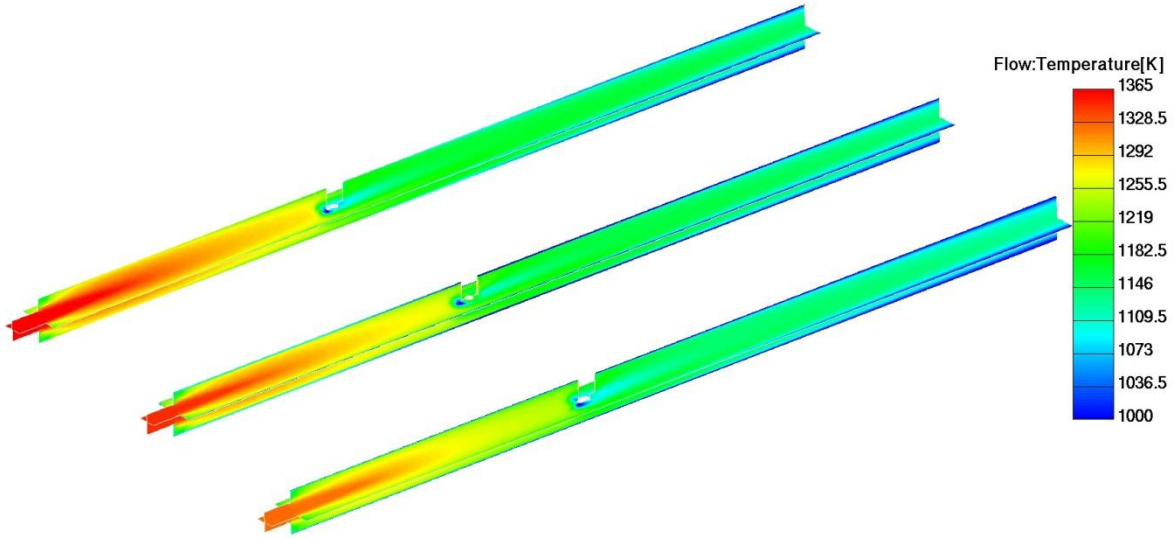


Figure 22. Temperature field

In Figure 23 the water vapour concentration inside the calculated experimental pipe is given. High temperature difference between the flow and injected urea water solution causes almost instantaneous evaporation of water content from droplets, which consequently means that the highest water concentration is in the vicinity of injector. After the injector, concentration stabilizes at the average value of around 8 % and there is no significant difference between three simulated cases. It is a reasonable result which shows that temperature difference between flow and UWS solution is so high that temperature variation in simulated cases doesn't affect rapid water evaporation. Thermolysis of urea is taking place after water content of droplets gets below 5 %. Urea is decomposed in equimolar amounts to ammonia and isocyanic acid.

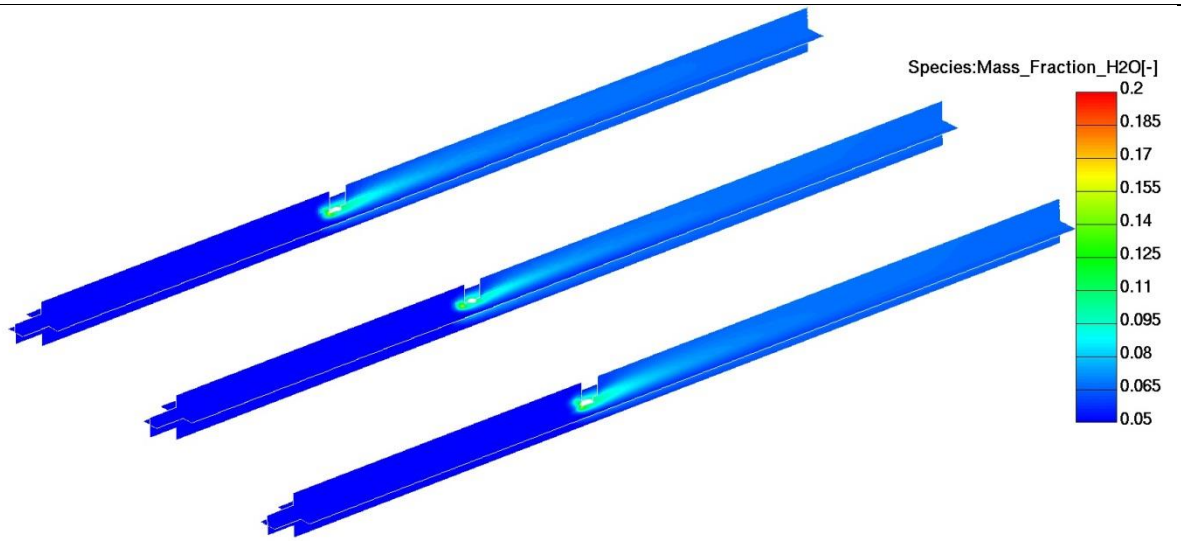


Figure 23. Water vapour mass fraction

Comparison of Figure 24 and Figure 25 reveals that isocyanic acid is consumed in reactions with NO much more than NH_3, indicating favourable simulation temperatures for former reactions. Comparison of simulated cases reveals that conditions in the first case yield the most favourable results in terms of production of a HNCO.

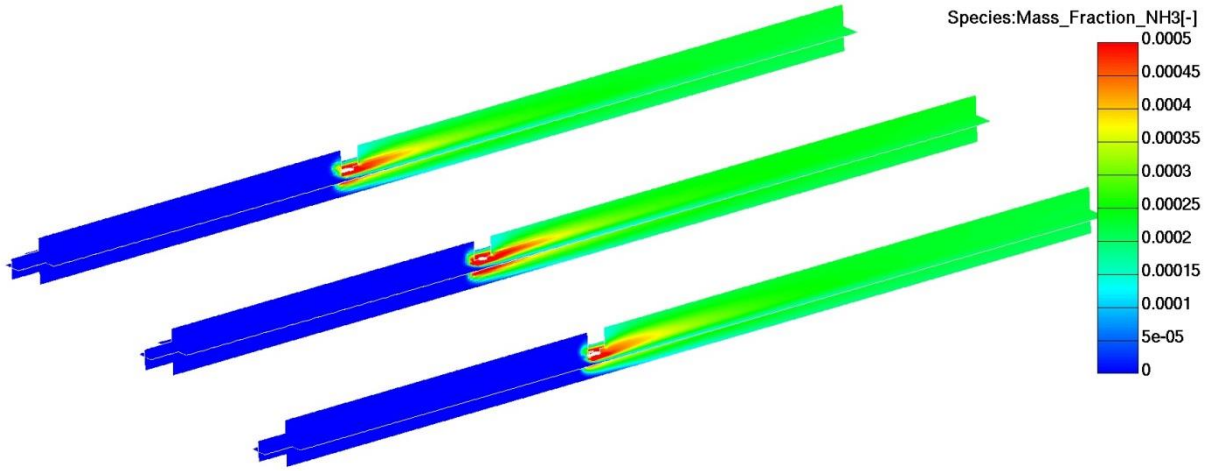


Figure 24. Ammonia mass fraction distribution

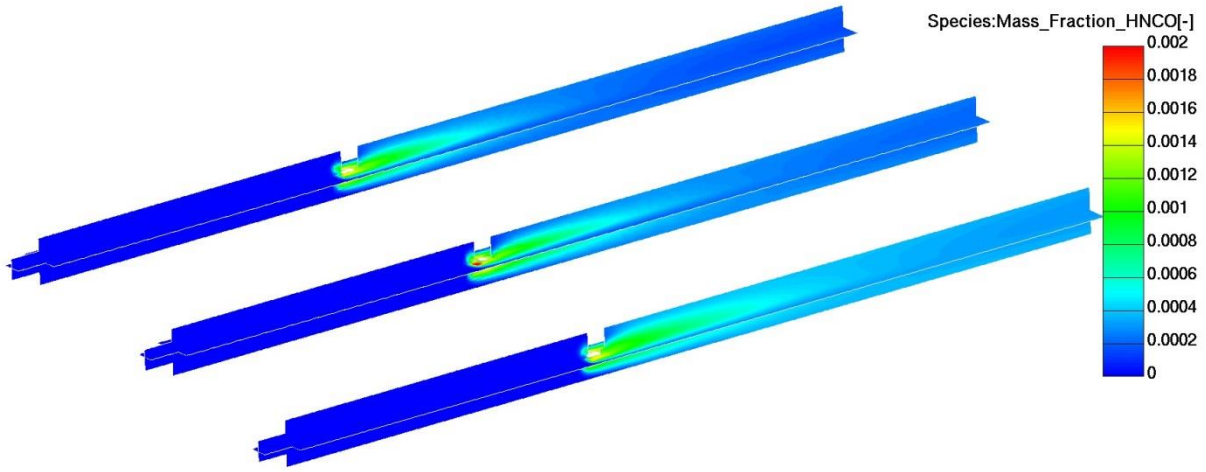


Figure 25. Isocyanic acid mass fraction distribution

Figure 26 shows NO concentration reduction inside the calculated experimental pipe which is the final aim of SNCR process. As the inlet flow temperature of simulated cases increases, NO reduction also increases. Connection with the consumption of HNCO is clearly visible, where third case with highest HNCO consumption yields the best NO reduction. In the injector region, due to the reaction of HNCO with NO, the NO mass fraction starts to decrease and continues so by flowing further downstream, which is equivalent to increase in reaction residence time.

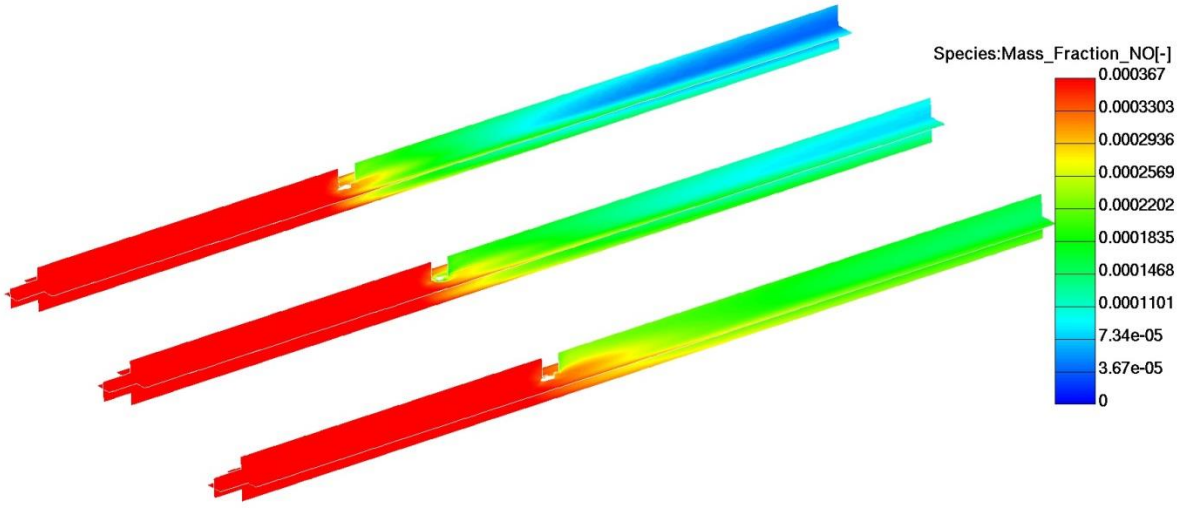


Figure 26. NO mass fraction distribution

Finally, in Figure 27 the comparison of experimental measurements with numerical predictions is given. The results are compared at the location of the measurement probe 200

mm before the pipe exit. Here it should be noted that the mean value for the numerical results was taken, since the location of the probe within the experimental pipe cross section is not mentioned. The numerical predictions show satisfying agreement with the experimental ones, although trend seen in experiment is not captured by the simulation. Contrary to simulations where NO reduction efficiency rises steadily with increasing temperature, experimental data show maximum in second case and then NO reduction efficiency drops afterwards. The reason behind this discrepancy may lay in the fact that linear temperature drop of the wall fitted from experimental measurements was provided only for the third case, which consequently shows the best agreement with NO reduction measurement. For cases 1 and 2 authors made an approximation on the inlet air temperature based on physical reasoning, but it can be clearly seen that some crucial information from experiment are needed for more accurate simulation. However, satisfactory agreement with experimental results gives reasonable confidence for industrial application of described model, described in the following section.

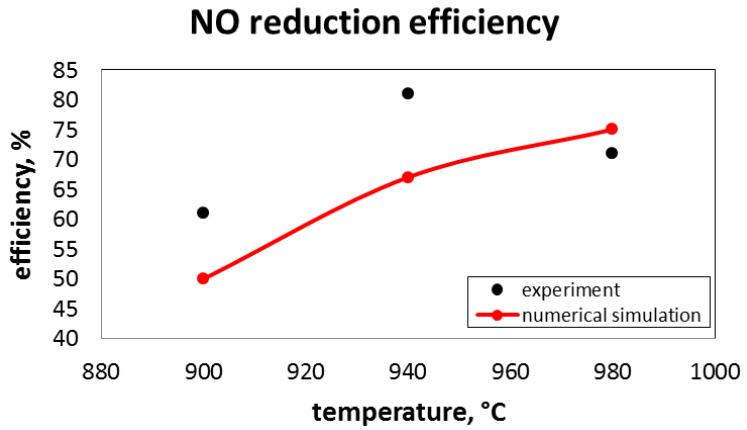


Figure 27. Comparison of experimental and numerical results

5.4.2. Industrial incinerator

5.4.2.1. Experimental configuration

Simple test cases are appropriate for checking the quality of individual implemented models or few of them, but the synergy of all physical models describing certain industrial application should be validated on some real industrial case for which, ideally there are some confident experimental measurements.

The combustor considered in this study has two chambers: the primary combustor and the secondary combustor. Municipal solid waste is burned in the primary combustor. The gas produced from the incineration is treated by a urea-based SNCR process installed in the secondary combustor to reduce the NOx concentration. The secondary combustor together with the outlet duct was used for CFD simulation as depicted in Figure 28. The plant capacity was designed for 50 ton/day. The plant data (temperature, flowrate, and NOx/SOx/CO/O2/HCl/dust concentrations) used in this study were obtained from the average values for 20 min, during a stable operation using telemetry monitoring system PG-250 (Horiba, Japan) Ammonia was measured by the NH_3 electrode (Orion 95-12, Thermo-electron Co., USA) [31].

5.4.2.2. Numerical simulation

Figure 28 depicts computational domain used in research of industrial incinerator together with the boundary surfaces. In order to achieve mesh independency several computational meshes were examined [91]. After evaluation, a computational domain consisting of 179 106 control volumes was selected. The most of those volumes were created in hexahedronal shape, especially in the regions of the utmost interest, such as injection point of the urea-water solution. To fully account the turbulent flow within the system a 3D computational mesh was used. The full detail on the geometry of the system can be found in [31].

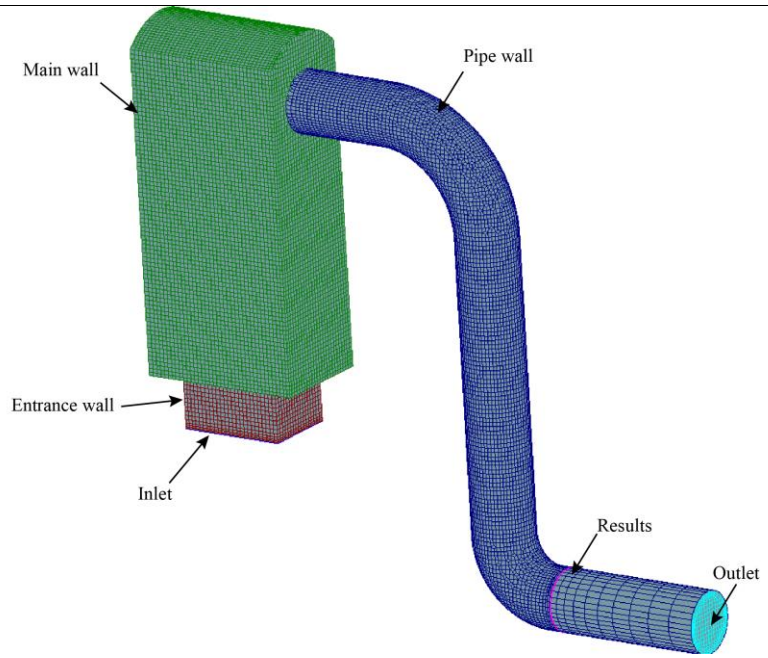


Figure 28. Computational domain of the incinerator

At the inlet a mixture of gases (NO, CO_2, O_2, N_2) with the temperature of 830 °C and a mass flow rate of 4.6602 kg/s enters the domain. The normal velocity taken from the experiments is 6 m/s. The temperature of the incinerator wall decreases as a result of heat loss to the surrounding. The temperature on the entrance wall reduces for 30 °C/m, on the main wall for 15 °C/m, whilst the pipe wall temperature is held at the constant temperature of 660 °C. The results were recorded at the Results selection. The location of this selection corresponds to the location of the measured data. The domain was prolonged from the selection Results to the Outlet selection to achieve the parabolic boundary conditions. At the outlet of the domain, the pressure boundary condition was applied. The 4 % urea-water solution is injected into the domain using three injectors with constant velocity of 25 m/s. The droplet disintegration models were replaced by presuming the droplet size distribution. The mean droplet diameter of the solution was 45 μm for the observed nozzle system. It is of utmost importance to correctly describe the spray process since the evaporation rate and the mixing between the droplet phase and bulk phase directly influence the thermolysis process and NO reduction. The Rosin–Rammler distribution with spread parameter value of 3 was used to represent the non-uniform droplet size distribution [31]. The urea-water solution spray at the developed state is shown in Figure 29.

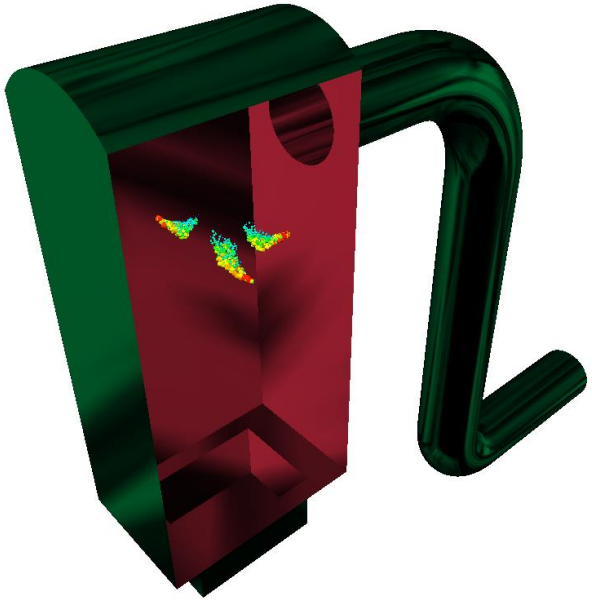


Figure 29. Urea-water solution spray at the the developed state

The same reduced kinetic model from Brouwer depicted in the Table 3 was employed to describe the chemistry processes occurring in the system. The NO reduction was achieved with reaction of the nitrogen oxide with the species generated from the thermolysis of the urea-water solution.

The numerical setup of the simulation was taken the same as in the previously validated numerical simulation of pipe reactor. The time step was set to 1e-04 s and it was conditioned with the used reaction mechanism. Simulation used turbulence settings as follows: 8 % turbulence intensity on the inlet and hydraulic diameter of 1.627 m [31]. With the given time discretisation and numerical setup, the simulation was stable and convergence of the solution in each time step was achieved.

5.4.2.3. Results

In Figure 30 several quantities of interest are shown for the initial stage (0.5 s) of urea injection and for the quasi-stationary state reached at 10 s. The first column shows the temperature field for mentioned time frame. Initially the gas mixture starts to flow into the incinerator with 6 m/s velocity and temperature of 1273.15 K. For better convergence and for reducing the simulation time the whole domain was initialised with the conditions that occur at the inlet selection. Therefore, in the whole domain at the initial state the NO was present in a certain amount. The urea-water solution was injected into the domain via three nozzles with total injected mass of 0.0107 kg/s. The endothermal thermolysis process occurred in the

region where the urea-water solution droplets are injected, as visible on the first column in Figure 30. Therefore, the temperature reduction can be addressed to the thermolysis of the injected solution. The thermolysis process is modelled according to the model described in the previous section. The second column shows the results of the 0D reactor model used for calculation of species reaction rates according to the seven step chemical mechanism. The NO reduction rate is visible and in accordance with the used mechanism. The negative NO reduction rate, that is visible in the second column, influences the overall NO species mass concentration. The spatial NO concentration is shown in the last column of Figure 30 and the border between zone of high NO concentration and zone with reduced concentration is actually the curve that correspond well to the NO reduction rate. However, due to the current nozzle positioning a certain amount of gas mixture containing high NO concentration passes into the pipe and outflows together with gas mixture with removed NO species.

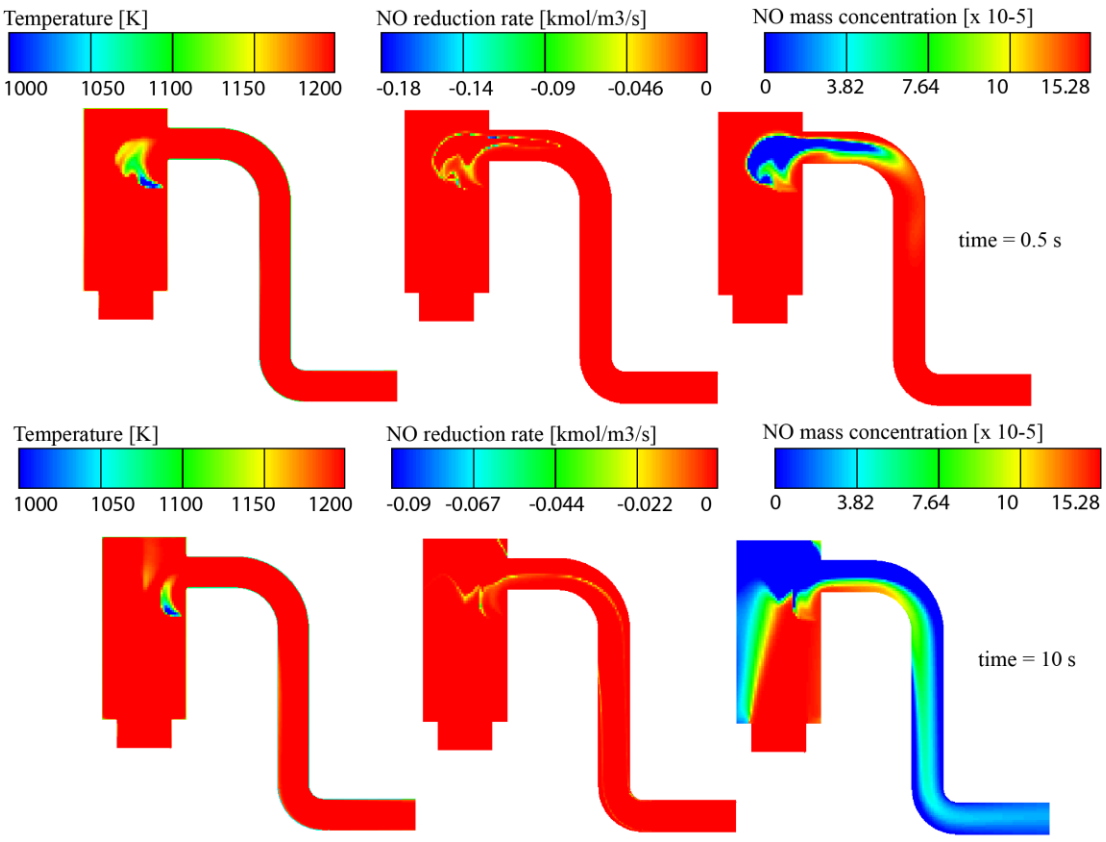


Figure 30. Flow temperature, NO reduction rate and NO mass concentration for two time points

Figure 31 shows the velocity field together with water and ammonia mass fraction for two different time instances. The average velocity value, after quasi steady state has been reached, is approximately 6 m/s inside the incinerator and increases to 10 m/s in the exit pipe

due to the continuity law. It would be expected that increased velocity will cause better reagent mixing in the exit pipe. However, as can be seen in the last column of Figure 31, this is not the case, since most of the ammonia is consumed in the SNCR process before even reaching the exit pipe. The injected water from UWS evaporates completely before the exit pipe and is diluted to minuscule quantities by turbulent mixing.

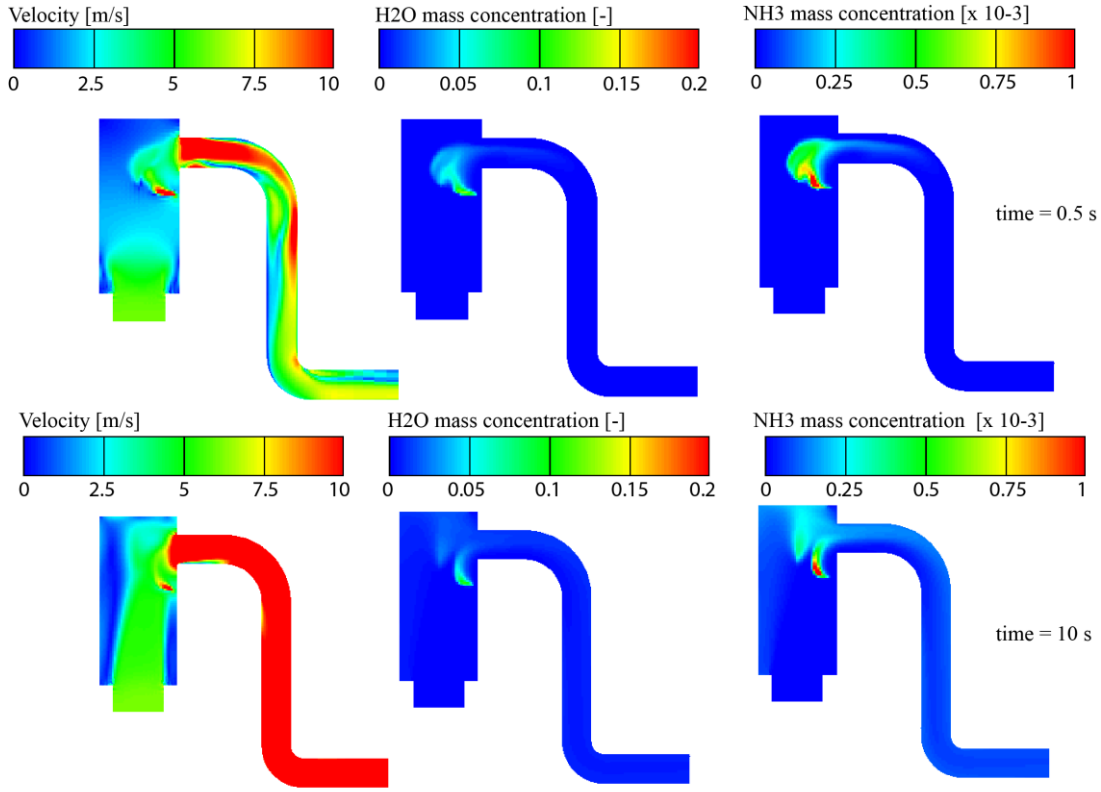


Figure 31. Flow velocity, H_2O and NH_3 mass fraction for two time points

The mix of reduced and the NO rich zone passes through selection at the outflow of the pipe, as shown in Figure 32. This position corresponds to the measurement position from the experiment which is used to calculate the NO reduction. In experimental research the recorded NO outlet concentration was 45 ppm, whilst in the simulation was 22.5 ppm. On the first sight it may look as a big discrepancy, but one should take into account that object is a miniscule quantity and also the position of the measurement probe was not indicated within the reference paper. Comparison with the outlet temperature is excellent with only 0.2 % discrepancy (932 °C compared to measured temperature of 930 °C). This implies that the numerical setup is correctly chosen and the used models are well implemented. Also, it means that the initial and boundary conditions are defined in correct way and are in a good

agreement with the experimental setup. Finally, it has been proven that developed model can be used as a part of development process of real industrial facilities.

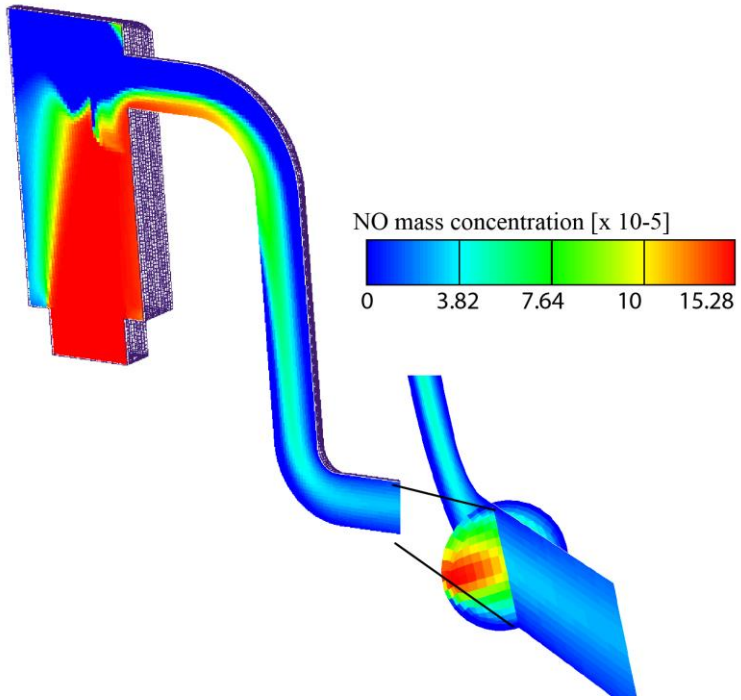


Figure 32. The NO mass fraction reduction from the inlet to the point of experimental measurement

6. CONCLUSION

This thesis makes improvement of the Eulerian liquid wall film model through further development and implementation of numerical models, with the ultimate goal of achieving more accurate and computationally efficient calculations as a surrogate for experimental approaches.

First objective was adaptation and implementation of semi-empirical wall film rupturing model to the numerical CFD framework. Verification of the implemented model was obtained through qualitative check of the cell position at which separation occurs, and through manual calculation of the separation criterion for activated cells. This is a reasonable approach, since only separation criterion is implemented in the code and there are no correlations describing properties of ruptured film. The pending problem of proper mathematical description of the percentage of separated film mass and particle size distribution of generated droplets remains to be considered in future studies. Further experimental investigation should be the object of future work in order to develop a quantitative model.

Multicomponent evaporation has been modelled by two approaches: by employing the modified wall functions derived by physical reasoning, and by utilizing the analogy between momentum and mass transfer. The latter approach proved to be more accurate in terms of comparison with experimental data from Wittig et al. [35]. However, limited experimental data prevent definitive conclusion on this matter. The provisory nature of derived wall functions seems to be responsible for higher discrepancies from experimental data. Particular scientific contribution presents implementation of the UNIFAC method for activity coefficients calculation, which is employed in the area of liquid wall films for the first time. It enables more accurate calculation of the interface concentrations in the case of multicomponent liquids, which have a decisive influence on the evaporation rate. Future work should include detailed modelling of liquid film properties, such as temperature and concentration, by employing some function dependency or film discretization procedure. It should be assessed how much would be that approach suitable by comparing increase in accuracy versus increase in computational time/resources.

Furthermore, the suitable kinetical model of urea thermal decomposition was adjusted and incorporated into existing numerical framework as a step in the process of description of

the urea deposits influence on overall domain of the real flue gas aftertreatment system. The model was checked against 0D experimental results, where urea and its by-products were analysed in quiescent conditions. The biuret mass loss has excellent agreement with experimental data, whilst cya and total mass depart slightly from the experimentally measured curve. However, the overall behaviour is satisfactory. Literature review hasn't revealed any experiment in highly convective environment of real exhaust gas systems configurations. Therefore, the nature of thermal decomposition in such conditions is still unknown and should be determined experimentally. Instead, the model was verified through physical examination of plate cooling by spray injection. As expected, the deposits have been formed in the high temperature zone at the film boundaries, and higher deposits such as triuret were present only in minuscule quantities.

Finally, this thesis presents the CFD modelling capabilities of physical phenomena taking place in the SNCR process. After the literature review, existing numerical framework was extended by incorporation of the suitable seven step reaction mechanism from Brouwer. It has been proven as sufficiently accurate and not overly demanding from the computational point of view. A 3D turbulent reacting flow CFD model involving reaction mechanism was applied on the pipe reactor experimental case. Results of the conducted numerical study show satisfactory agreement with measured data in terms of NO reduction efficiency, but the experimental trend was not captured by simulations. Afterwards, the same model was applied in the simulation of the large scale incinerator SNCR process, for which experimental measurements exist. The results show that the numerical prediction of NO reduction is in line with the measured NO reduction.

Overall, the work conducted here and validated by experimental measurements generally corresponding to the real industrial conditions, proves the research hypothesis that the improved, adopted and newly developed numerical models are going to enable numerical simulations of multicomponent liquid wall films with emphasis on chemical kinetics of urea deposits, which could be then used in industrial applications.

Due to the global pollution problem, the increasingly strict legislation on allowed emissions from the industry and transport sector forces manufacturers to design more efficient and optimized products. Direct consequence is increased complexity of the design process, which makes advanced design tools such as computational modelling of fluid dynamics a necessity. The improved model of liquid wall film behaviour developed within this thesis may be a valuable contribution in continuous process where the constant improvement of the

physical model accuracy used in CFD is mandatory in order to comply with the ever increasing requirements of the industry.

7. LITERATURE

[1] Ra Y, Reitz RD. Numerical Study of Multi-Component Spray Combustion with a Discrete Multi- Component Fuel Model. Int. Multidimens. Engine Model. User's Gr. Meet. SAE Congr., Detroit: 2009, p. 6.

[2] Lee CF, Cheng WL, Wang D. Finite diffusion wall film evaporation model for engine simulations using continuous thermodynamics. Proc Combust Inst 2009;32:2801–8. doi:10.1016/j.proci.2008.06.087.

[3] O'Rourke PJ, Amsden AA. A Particle Numerical Model for Wall Film Dynamics in Port-Injected Engines. 1996. doi:10.4271/961961.

[4] Zeng Y, Lee C. Multicomponent-Fuel Film-Vaporization Model for Multidimensional Computations. J Propuls Power 2000;16:964–73. doi:10.2514/2.5697.

[5] Torres DJ, O'rourke PJ, Amsden AA. Efficient multicomponent fuel algorithm. Combust Theory Model 2003;7:66–86. doi:10.1088/1364-7830/7/1/304.

[6] Seyed Vahid Ebrahimian Shiadeh. Development of multi-component evaporation models and 3D modeling of NOx-SCR reduction system. Institut National Polytechnique de Toulouse, 2011.

[7] Desoutter G, Habchi, Chawki, Bénédicte Cuenot TP. Single-component liquid film evaporation model development and validation using direct numerical simulations. Proc. ICLASS 2006, Kyoto: 2006, p. 8.

[8] Owen I, Ryley DJ. The flow of thin liquid films around corners. Int J Multiph Flow 1985;11:51–62. doi:10.1016/0301-9322(85)90005-9.

[9] Maroteaux F, Llory D, Le Coz J-F, Habchi C. Liquid Film Atomization on Wall Edges—Separation Criterion and Droplets Formation Model. J Fluids Eng 2002;124:565. doi:10.1115/1.1493811.

[10] Gubaidullin A. Comments on "Liquid Film Atomization on Wall Edges-Separation Criterion and Droplets Formation Model." J Fluids Eng 2007;129:665. doi:10.1115/1.2721078.

[11] Steinhaus BC, Ghandhi JB, Shedd TA. Experimental Investigation of Liquid Film Stripping at a Sharp Corner. Proc. ILASS Am. 20th Annu. Conf. Liq. At. Spray Syst., Chicago, Illinois: 2007, p. 8.

[12] Friedrich MA, Lan H, Wegener JL, Drallmeier JA, Armaly BF. A Separation Criterion With Experimental Validation for Shear-Driven Films in Separated Flows. J Fluids Eng 2008;130:051301. doi:10.1115/1.2907405.

[13] Bacharoudis E, Bratec H, Keirsbulck L, Buchlin J, Labraga L, France N De, et al. Experimental study of a horizontal shear-driven liquid film approaching a sharp corner . Critical conditions . UVHC , TEMPO , 59313 Valenciennes , France. Proc. ICLASS 2012, 12th Trienn. Int. Conf. Liq. At. Spray Syst., 2012, p. 1–8.

[14] Bacharoudis E, Bratec H, Keirsbulck L, Buchlin J-M, Labraga L. Onset of Atomization on Horizontal, Shear-Driven Liquid Films At the Vicinity of a Sharp Corner. At Sprays 2013;23:763–97. doi:10.1615/AtomizSpr.2013006811.

[15] Bacharoudis E, Bratec H, Keirsbulck L, Buchlin J-M, Labraga L. Simplified model for the prediction of the occurrence of film atomization in corner geometries. Int J Multiph Flow 2014;58:325–37. doi:10.1016/j.ijmultiphaseflow.2013.10.003.

[16] Birkhold F, Meingast U, Wassermann P, Deutschmann O. Modeling and simulation of the injection of urea-water-solution for automotive SCR DeNOx-systems. Appl Catal B Environ 2007;70:119–27. doi:10.1016/j.apcatb.2005.12.035.

[17] Wurzenberger JC, Wanker R. Multi-Scale SCR Modeling, 1D Kinetic Analysis and 3D System Simulation, 2005. doi:10.4271/2005-01-0948.

[18] Ebrahimian V, Nicolle A, Habchi C. Detailed modeling of the evaporation and thermal decomposition of urea-water solution in SCR systems. AIChE J 2012;58:1998–2009. doi:10.1002/aic.12736.

[19] Schaber PM, Colson J, Higgins S, Thielen D, Anspach B, Brauer J. Thermal decomposition (pyrolysis) of urea in an open reaction vessel. Thermochim Acta 2004;424:131–42. doi:10.1016/j.tca.2004.05.018.

[20] Lundström A, Andersson B, Olsson L. Urea thermolysis studied under flow reactor conditions using DSC and FT-IR. Chem Eng J 2009;150:544–50. doi:10.1016/j.cej.2009.03.044.

[21] Eichelbaum M, Farrauto RJ, Castaldi MJ. The impact of urea on the performance of metal exchanged zeolites for the selective catalytic reduction of NOxPart I. Pyrolysis and hydrolysis of urea over zeolite catalysts. Appl Catal B Environ 2010;97:90–7. doi:10.1016/j.apcatb.2010.03.027.

[22] Brack W, Heine B, Birkhold F, Kruse M, Schoch G, Tischer S, et al. Kinetic modeling of urea decomposition based on systematic thermogravimetric analyses of urea and its most important by-products. Chem Eng Sci 2014;106:1–8. doi:10.1016/j.ces.2013.11.013.

[23] Palash SM, Masjuki HH, Kalam MA, Masum BM, Sanjid A, Abedin MJ. State of the art of NOx mitigation technologies and their effect on the performance and emission characteristics of biodiesel-fueled Compression Ignition engines. Energy Convers Manag 2013;76:400–20. doi:10.1016/j.enconman.2013.07.059.

[24] Kozarac D, Vuilleumier D, Saxena S, Dibble RW. Analysis of benefits of using internal exhaust gas recirculation in biogas-fueled HCCI engines. Energy Convers Manag 2014;87:1186–94. doi:10.1016/j.enconman.2014.04.085.

[25] European Union, Directive 2010/75/EU. 2010.

[26] European Union, Directive 2000/76/EU. 2000.

[27] Mahmoudi S, Baeyens J, Seville JPK. NOx formation and selective non-catalytic reduction (SNCR) in a fluidized bed combustor of biomass. Biomass and Bioenergy 2010;34:1393–409. doi:10.1016/j.biombioe.2010.04.013.

[28] Li Z, Liu XM, Yang DH, Qin WJ, Yang GS, Zhang DL. Research of the SNCR Process and its Application. Adv Mater Res 2014;953-954:1307–14. doi:10.4028/www.scientific.net/AMR.953-954.1307.

[29] Nguyen TDB, Lim Y Il, Kim SJ, Eom WH, Yoo KS. Experiment and computational fluid dynamics (CFD) simulation of urea-based selective noncatalytic reduction (SNCR) in a pilot-scale flow reactor. Energy and Fuels 2008;22:3864–76. doi:10.1021/ef8004652.

[30] Xia Z, Li J, Wu T, Chen C, Zhang X. CFD simulation of MSW combustion and SNCR in a commercial incinerator. Waste Manag 2014;34:1609–18. doi:10.1016/j.wasman.2014.04.015.

[31] Nguyen TDB, Kang T-H, Lim Y-I, Eom W-H, Kim S-J, Yoo K-S. Application of urea-based SNCR to a municipal incinerator: On-site test and CFD simulation. Chem Eng J 2009;152:36–43. doi:10.1016/j.cej.2009.03.025.

[32] Mikulčić H, Vujanović M, Fidaros DK, Priesching P, Minić I, Tatschl R, et al. The application of CFD modelling to support the reduction of CO2 emissions in cement industry. Energy 2012;45:464–73. doi:10.1016/j.energy.2012.04.030.

[33] Kapitler M, Samec N, Kokalj F. Numerical optimization of a waste-to-energy plant's operating parameters using CFD. Therm Sci 2011;15:1–16. doi:10.2298/TSCI101004084K.

[34] Samec N, Kokalj F, Chen J-Y. Combustion Simulation in the Secondary Chamber of a Pilot-Scale Incinerator. Environ Eng Sci 2007;24:905–16. doi:10.1089/ees.2006.0154.

[35] Gerendas M, Wittig S. Experimental and Numerical Investigation on the Evaporation of Shear-Driven Multicomponent Liquid Wall Films. J Eng Gas Turbines Power 2001;123:580. doi:10.1115/1.1362663.

[36] Tadić M. Prijenos topline i tvari n.d.

[37] Alfirević I. Uvod u tenzore i mehaniku kontinuuma. Zagreb: Golden marketing; 2003.

[38] Mehanika fluida II 2013:99.

[39] Henk Tennekes JLL. A First Course in Turbulence. First prin. Cambridge, Massachusetts: MIT Press; 1972.

[40] Wilcox DC. Turbulence Modeling for CFD. Third Edit. La Cañada Flintridge, California: DCW Industries; 2006.

[41] Vujanović M. Numerical modelling of multiphase flow in combustion of liquid fuel. University of Zagreb, 2010.

[42] Pope SB. Turbulent Flows. 1st editio. Cambridge University Press; 2000.

[43] Launder BE, Spalding DB. The numerical computation of turbulent flows. Comput Methods Appl Mech Eng 1974;3:269–89. doi:10.1016/0045-7825(74)90029-2.

[44] B. E. Launder, A. Morse, W. Rodi DBS. The prediction of free shear flows - A comparison of the performance of six turbulence models. Proc. NASA Conf. Free

Shear Flows, Langley: 1972.

[45] Durbin PA. Near-wall turbulence closure modeling without “damping functions.” Theor Comput Fluid Dyn 1991;3:1–13. doi:10.1007/BF00271513.

[46] Hanjalić K, Popovac M, Hadžiabdić M. A robust near-wall elliptic-relaxation eddy-viscosity turbulence model for CFD. Int J Heat Fluid Flow 2004;25:1047–51. doi:10.1016/j.ijheatfluidflow.2004.07.005.

[47] Kolmogorov A. The Local Structure of Turbulence in Incompressible Viscous Fluid for Very Large Reynolds’ Numbers. Dokl Akad Nauk SSSR 1941;30:301–5.

[48] Durbin PA. On the k-3 stagnation point anomaly. Int J Heat Fluid Flow 1996;17:89–90. doi:10.1016/0142-727X(95)00073-Y.

[49] Baburić M. Numerically efficient modelling of turbulent non-premixed flames. University of Zagreb, 2006.

[50] H. Versteeg WM. An Introduction to Computational Fluid Dynamics: The Finite Volume Method. second. Harlow: Pearson; 2007.

[51] Tuković Ž. Metoda kontrolnih volumena na domenama promjenjivog oblika. Sveučilište u Zagrebu, 2005.

[52] J. H. Ferziger MP. Computational Methods for Fluid Dynamics. 3rd editio. Springer; 2002.

[53] YUEN MC, CHEN LW. On Drag of Evaporating Liquid Droplets. Combust Sci Technol 1976;14:147–54. doi:10.1080/00102207608547524.

[54] Vujanović M, Petranović Z, Edelbauer W, Baleta J, Duić N. Numerical modelling of diesel spray using the Eulerian multiphase approach. Energy Convers Manag 2015;104:160–9. doi:10.1016/j.enconman.2015.03.040.

[55] Dukowicz JK. Quasi-steady droplet phase change in the presence of convection. 1979.

[56] Dukowicz JK. A particle-fluid numerical model for liquid sprays. J Comput Phys 1980;35:229–53. doi:10.1016/0021-9991(80)90087-X.

[57] Sirignano WA. Fluid Dynamics and Transport of Droplets and Sprays. Second Edi. New York: Cambridge University Press; 2010.

[58] Abramzon B, Sirignano WA. Droplet vaporization model for spray combustion calculations. Int J Heat Mass Transf 1989;32:1605–18. doi:10.1016/0017-9310(89)90043-4.

[59] AVL Fire: Lagrangian Multiphase Module Manual, version 2011 n.d.

[60] Wang TJ, Baek SW, Lee SY, Kang DH, Yeo GK. Experimental investigation on evaporation of urea-water-solution droplet for SCR applications. AIChE J 2009;55:3267–76. doi:10.1002/aic.11939.

[61] Yim SD, Kim SJ, Baik JH, Nam IS, Mok YS, Lee JH, et al. Decomposition of urea into NH3 for the SCR process. Ind Eng Chem Res 2004;43:4856–63. doi:10.1021/ie034052j.

[62] Farcy B, Abou-Taouk A, Vervisch L, Domingo P, Perret N. Two approaches of chemistry downsizing for simulating selective non catalytic reduction DeNOx process. Fuel 2014;118:291–9. doi:10.1016/j.fuel.2013.10.070.

[63] Brouwer J, Heap MP, Pershing DW, Smith PJ. A model for prediction of selective noncatalytic reduction of nitrogen oxides by ammonia, urea, and cyanuric acid with mixing limitations in the presence of co. Symp Combust 1996;26:2117–24. doi:10.1016/S0082-0784(96)80036-1.

[64] Desoutter G. Etude numérique de la propagation d'une flamme sous l'influence d'un film liquide de carburant sur la paroi. Institut National Polytechnique de Toulouse, 2007.

[65] Stanton DW, Rutland CJ. Multi-dimensional modeling of thin liquid films and spray-wall interactions resulting from impinging sprays. Int J Heat Mass Transf 1998;41:3037–54. doi:10.1016/S0017-9310(98)00054-4.

[66] Bai C, Gosman AD. Mathematical Modelling of Wall Films Formed by Impinging Sprays. 1996. doi:10.4271/960626.

[67] Foucart H, Habchi C, Le Coz JF, Baritaud T. Development of a Three Dimensional Model of Wall Fuel Liquid Film for Internal Combustion Engines. 1998. doi:10.4271/980133.

[68] Ebner J, Schober P, Schäfer O, Wittig S. Modelling of Shear-Driven Liquid Wall Films on Curved Surfaces : Effect of Accelerated Air Flow and Variable Film Load. Proc. ICLASS 2003, 9th Trienn. Int. Conf. Liq. At. Spray Syst., Sorento: 2003.

[69] Lucchini T, D'Errico G, Brusiani F, Bianchi GM, Tuković Ž, Jasak H. Multi-dimensional modeling of the air/fuel mixture formation process in a PFI engine for motorcycle applications, 2009. doi:10.4271/2009-24-0015.

[70] Cazzoli G, Forte C. Development of a model for the wall film formed by impinging spray based on a fully explicit integration method 2005. doi:10.4271/2005-24-087.

[71] AVL. FIRE ® VERSION 2014.2 manual 2015.

[72] Wurz D. Experimentelle Untersuchung des Strömungsverhaltens dünner Wasserfilme und deren Rückwirkung auf einen gleichgerichteten Luftstrom mäßiger bis hoher Unterschallgeschwindigkeit. Karlsruhe Institute of Technology, 1971.

[73] Sill KH. Wärme- und Stoffübergang in turbulenten Strömungsgrenz-schichten längs verdunstender welliger Wasserfilme. Karlsruhe Institute of Technology, 1982.

[74] Sattelmayer T. Zum Einfluß der ausgebildeten, turbulenten Luft-Flüssigkeitsfilm-Strömung auf den Filmzerfall und die Tropfenbildung am Austritt von Spalten geringer Höhe. Karlsruhe Institute of Technology, 1985.

[75] Arai, T., Hashimoto H. Disintegration of a thin liquid sheet in a cocurrent gas stream. ICLASS'85, London: 1985.

[76] Burck E. Der Einfluß der Prandtl-Zahl auf den Wärmeuübergang und Druckverlust künstlich aufgerauhter Strömungskanäle. Wärme-Stoffübertrag 1969;2:87–98.

[77] Jayatilleke CLV. The Influence of Prandtl Number and Surface Roughness on the Resistance of the Laminar Sub-Layer to Momentum and Heat Transfer. Prog Heat Mass Transf 1969;1.

[78] O'Rourke PJ, Amsden AA. A Particle Numerical Model for Wall Film Dynamics in Port-Injected Engines. 1996. doi:10.4271/961961.

[79] Fredenslund A, J. Gmehling PR. Vapor-liquid Equilibria Using Unifac. Amsterdam: Elsevier; 1977.

[80] Brenn, G., Deviprasath, L.J. and Durst F. Computations and Experiments on the Evaporation of Multi-Component Droplets. Proc.9th Int.Conf.Liquid At. Syst. (ICLASS), Sorento: 2003.

[81] Koebel M, Elsener M, Marti T. NO x -Reduction in Diesel Exhaust Gas with Urea and Selective Catalytic Reduction. Combust Sci Technol 1996;121:85–102. doi:10.1080/00102209608935588.

[82] Nishioka A, Sukegawa Y, Katogi K, Mamada H, Kowatari T, Mukai T, et al. A Study of a New Aftertreatment System (2): Control of Urea Solution Spray for Urea-SCR, 2006. doi:10.4271/2006-01-0644.

[83] Linhard M. Der Dampfdruck flüssiger Cyansäure. Zeitschrift Für Anorg Und Allg Chemie 1938;236:200–8. doi:10.1002/zaac.19382360118.

[84] Kuhnke D. Spray Wall Interaction Modelling by Dimensionless Data Analysis. TU Darmstadt, 2004.

[85] Baleta J. Numerical investigation of wallfilm formation for selective catalytic reduction applications. University of Zagreb, 2013.

[86] Wittig S, Himmelsbach J, Noll B, Feld HJ, Samenfink W. Motion and Evaporation of Shear-Driven Liquid Films in Turbulent Gases. J Eng Gas Turbines Power 1992;114:395. doi:10.1115/1.2906604.

[87] Birkhold F. Selektive katalytische Reduktion von Stickoxiden in Kraftfahrzeugen : Untersuchung der Einspritzung von Harnstoffwasserlosung. Das Karlsruher Institut für Technologie (KIT), 2007.

[88] Schiller L. NAZ. A drag coefficient correlation. VDI Zeitschrift 1933;77:318–20.

[89] Birkhold F, Meingast U, Wassermann P, Deutschmann O. Analysis of the Injection of Urea-Water-Solution for Automotive SCR DeNOx-Systems: Modeling of Two-Phase Flow and Spray/Wall-Interaction, 2006. doi:10.4271/2006-01-0643.

[90] AVL. FIRE ® VERSION 2013.2 manual. 2013.

[91] Baleta J, Mikulčić H, Vujanović M, Petranović Z, Duić N. Numerical simulation of urea based selective non-catalytic reduction deNOx process for industrial applications. Energy Convers Manag 2016. doi:10.1016/j.enconman.2016.01.062.

CURICULUM VITAE

Jakov Baleta was born on January 12th, 1989 in Sisak, Croatia. After completing secondary school in Sisak in 2007, he was enrolled in the Faculty of Mechanical Engineering and Naval Architecture, University of Zagreb. There he finished undergraduate and graduate study of power and process engineering with highest honour (summa cum laude) and for which he also received medals of the Faculty. During his study he was also awarded with Davorin Bazjanac award for the best student in academic year 2008/2009, "Hrvoje Požar" Award for exceptional scholastic ability on power engineering study in 2012, INETEC (Institute for Nuclear Technology) Award for achievement during the study in 2012 and Dean's Award for promotion of the Faculty of Mechanical Engineering and Naval Architecture in the same year.

He is proficient in the use of English, both written and spoken, and has basic communication knowledge of German. Since 2013 he is enrolled in the postgraduate study at the University of Zagreb and is employed as a researcher at the Power Engineering and Energy Management Chair at the Department of Energy, Power Engineering and Environment, Faculty of Mechanical Engineering and Naval Architecture. During the postgraduate study he has participated in two international workshops, namely Short Course Atomization and Sprays, held at TU Darmstadt, Darmstadt, Germany in February of 2015 and Building Knowledge and Experience Exchange in CFD, Central European Exchange Program for University Studies (CEEPUS), held at TU Brno, Brno, Czech Republic in December of 2015. He has been a member of the Adria Section of Combustion Institute since 2014 and member of the International Centre for Sustainable Development of Energy, Water and Environment Systems (SDEWES Centre) since 2013. Also, beginning from 2013, he has served as a member of Local Organising Committee of the 8th, 9th and 10th Conferences on Sustainable Development of Energy, Water and Environment Systems and 1st South East European Conference on Sustainable Development of Energy, Water and Environment Systems.

Areas of his research are: rational use of energy in buildings and industry, with a focus on heat pumps, energy analysis of HVAC systems and the development of mathematical models of computational fluid dynamics problems in the treatment of exhaust gases of internal combustion engines. Hi serves as a reviewer for Journal of Cleaner Production, Energy and Energy Conversion and Management. His hobbies include: playing guitar, sailing,

philosophy of mathematics, physics, travelling, etc. Complete list of publications is available on: http://bib.irb.hr/lista-radova?autor=340845&lang=EN.